University of Southampton

FACULTY OF PHYSICAL SCIENCES AND ENGINEERING

Optoelectronics Research Centre

Fiberised silicon photonics for infrared nonlinear photonics

by

Haonan Ren

Thesis for the degree of Doctor of Philosophy

September 2019

University of Southampton

Abstract

FACULTY OF PHYSICAL SCIENCES AND ENGINEERING

Optoelectronics Research Centre

Thesis for the degree of Doctor of Philosophy

Fiberised silicon photonics for infrared nonlinear applications

by

Haonan Ren

Silicon photonics is fast becoming one of the most active research areas. Within this field, silicon waveguides have gained significant attention for their tight light confinement, which makes them well suited for nonlinear applications. In recent years, silicon core optical fibres have emerged as a new platform for nonlinear optics. The motivation of this project is to characterise the nonlinear properties of the silicon core fibres and build novel nonlinear photonic devices. In this work, firstly, a tapering process is introduced to reduce the core sizes of the silicon core fibres down to sizes required for nonlinear applications. The tapers are studied numerically and the linear optical transmission properties characterised experimentally. Then, the optical nonlinear properties, such as the nonlinear Kerr coefficient and two-photon absorption parameter of these fibres are characterised by fitting experimental data of high-power pulse propagation with numerical simulations of the nonlinear Schrodinger equation. These characterisations cover wavelengths from telecom band to short wave infrared regime. Secondly, supercontinuum generation is demonstrated experimentally in various silicon core fibres with different taper profiles. The process of the supercontinuum is also studied numerically to understand the pulse dynamics. The results are analysed with respect to the power efficiency and coherence properties. Thirdly, an inverse taper structure is demonstrated as a novel approach for integrating the silicon core fibres with conventional silica fibre systems. The fabrication process of the integration technique is fully documented. The coupling efficiency of the device is characterised using a combination of experiments and finite element numerical studies. These studies will pave the way for future all-fibre nonlinear silicon photonic systems.

Abstract

Table of Contents

List of Tables ..... **vi**
List of Figures ..... **vii**
Declaration of Authorship ..... **xv**
Acknowledgements ..... **xvii**
Definitions and Abbreviations ..... **xix**
Chapter 1 Introduction **1**
1.1 Fiberised nonlinear silicon photonics 1
1.1.1 Silicon core fibre 2
1.2 Literature review 4
1.2.1 From integrated circuit to nonlinear silicon photonics 4
1.2.2 Silicon core fibre 6
1.3 Thesis outline 11
1.4 Key achievements 12
Chapter 2 Background **13**
2.1 Introduction 13
2.2 Optical properties of fibre waveguides 13
2.2.1 Modal properties of step index fibre 13
2.2.2 Modes of a SCF 17
2.2.3 Linear transmission 18
2.2.4 Dispersion 20
2.3 Nonlinear short pulse propagation 23
2.3.1 Ultrafast laser pulses 23
2.3.2 Nonlinear light matter interaction 24
2.3.3 Nonlinear short pulse propagation 28
Chapter 3 Fabrication of tapered silicon core fibres **33**
3.1 Introduction 33
3.2 Melton core drawing technique 33
3.3 Tapering technique of SCF 35
3.3.1 Vytran glass processor 35
3.3.2 Tapering SCF with mechanical support 37

Capillary method 37
SMF splicing method 38
3.3.3 Profile of tapered SCF 39
Numerical model for tapering 40
Profile of tapered fibre 43
3.3.4 Fabrication of silicon nanowire 44
Capillary number 45
Optimisation of hot zone temperature 46
3.4 Sample polishing and mounting 47
3.5 Conclusion 48

Chapter 4 Characterisation of silicon core fibres 49

4.1 Introduction 49
4.2 Crystallinity of tapered silicon core fibres 49
4.3 Linear transmission characterisation 51
4.3.1 Cutback method 51
4.3.2 Fabry–Pérot method 55
4.4 Nonlinear properties of the SCFs 58
4.4.1 Transmission characterisation 58
4.4.2 Nonlinear absorption characterisation 60
4.4.3 Nonlinear refraction characterisation 62
4.5 Conclusion 64

Chapter 5 Mid-infrared supercontinuum generation 67

5.1 Introduction 67
5.2 Review of mid-IR SCG 67
5.3 Transmission window and dispersion map 68
5.4 Modelling of supercontinuum generation in silicon core fibres 70
5.4.1 Modified NLSE model for supercontinuum 70
5.4.2 Flow chart of modelling 70
5.5 SCG in straight fibre structure 71
5.5.1 SCF with a 2 μm core diameter 72
5.5.2 SCF with a 3 μm core diameter 74

5.6 SCG in tapered SCF in the SWIR 75
5.6.1 Design of the fibre profile 76
5.6.2 Experimental results 77
5.6.3 Numerical modelling analysis 78
5.7 SCG in the tapered SCF in MWIR 80
5.7.1 Design of fibre profile 80
5.7.2 Mode coupling and transmission 82
5.7.3 Experimental results 83
5.7.4 Numerical analysis 86
5.7.5 Coherence property 89
5.7.6 Spectral optimisation 90
5.8 Conclusion 91

Chapter 6 High index fiber integration 93

6.1 Introduction 93
6.2 Splicing of SCF nanospike to SMF 93
6.2.1 Fabrication 94
6.2.2 Optical characterisation 97
6.3 Splicing SCF nanospike to tapered SMF 98
6.3.1 Fabrication 99
6.3.2 Optical characterisation 102
6.4 Conclusion 105

Chapter 7 Conclusion and future work 107

7.1 Conclusion 107
7.2 Future work 107

List of publications 109
References 111

List of Tables

Table 2.1 Coefficients of Sellmeier equation for crystalline silicon. 21

Table 2.2 Coefficients of Sellmeier equation for fused silica 22

Table 3.1 The tapering parameters for the Vytran GPX-3300 37

Table 4.1. -20 dB band width for λ=1.54 μm 63

Table 4.2. -20 dB band width for selected pump wavelengths 63

Table 5.1 Summary of SCG in Group IV waveguide in recent 10 years. 68

Table 5.2. SCG simulation parameters 78

Table 5.3 MWIR SC results 84

Table 5.4. SCG simulation parameters 86

Table 6.1 Splicing optimisation of Vytran parameters (FTAV4 filament). 102

List of Figures

Figure 1.1 Coupling strategies between an optical fibre and a silicon planar waveguide. (a) Using a SSC. (b). Using a grating coupler. 2

Figure 1.2 Concept plan of a SCF device in a standard fibre system. On the right shows the cross section of a SCF. 3

Figure 1.3 A collection of reviewed SCFs in the past decade. (a). Scanning electron micrographs (SEM) of silicon fibres deposited in a honeycomb MOF template [22]. (b). A SCF deposited in a PCF template [46]. (c). SEM of a single core SCF [47]. (d). SEM of the first MCD SCF [23]. (e) SCF after tapering by a splicer. (f)-(g). Small core SCF after post process tapering [24]. 8

Figure 1.4 Collection of SCF devices. (a) A hybrid silicon-core, silica-clad microspherical resonator. (b) Packed solar SCF. (c) Bragg gratings written on SCF. (d) Silicon nano p-n spheres, scale bar 100 µm. 10

Figure 2.1 Cross sectional refractive index profile of a step-index optical fibre. 14

Figure 2.2 LP mode electric field amplitudes of a step-index fibre taken from Ref. [69]. The colour shows the different signs of the electric field. 16

Figure 2.3 Mode characteristics of a SCF. (a) Fundamental mode profile with core diameter of 10 µm. (b) Fundamental mode profile with core diameter of 1 µm. (c) High order modes examples of SCF with a core diameter of 10 µm. (d) Mode intensity profile (fundamental mode) of the SCF with core diameter of 10 µm. The black line shows the calculated profile and red dashed line shows the Gaussian curve fit. (e) Effective mode area (fundamental mode) of SCFs at the wavelengths λ = 1.55 µm and λ = 2 µm. 17

Figure 2.4 Schematic diagram of free space coupling to a SCF using lens. 18

Figure 2.5 Transmission window of silicon [74] and silica [75].....19

Figure 2.6 Refractive index measured by Li in 1980 at 293 K and 350K [73].....22

Figure 2.7 Dispersion profile of fundamental mode of SCF. (a) $\beta 2$ of SCF as a function of core size, for different wavelengths as labelled in the legend. (b) Material dispersion and waveguide dispersion contributions to a SCF with core diameter 1 µm. 23

List of Figures

Figure 2.8 Spectrogram of a hyperbolic secant pulse with different chirp parameters. Both pulses have $TFWHM$ of 0.1 ps at wavelength of λ = 2 µm. 24

Figure 2.9 Illustration of electric field-induced nonlinear polarisation of molecules. 25

Figure 2.10 (a) TPA process in a momentum energy diagram. $\hbar$ is the reduced Planck constant and Eg is the band gap energy. (b) FCA process in a momentum energy diagram..... 26

Figure 2.11 (a) Spectral evolution of SPM for a 1 ps Gaussian pulse at 1.55 µm propagating over the nonlinear length 10 LN. (b) Nonlinear phase shift and chirp of the output pulse. 31

Figure 3.1 SCFs fabricated using the MCD technique. (a) Photo of a small core SCF [64], illustrating its flexibility. (b) Photo of a large core SCF that is more rigid [63]. (c) SEM image of a SCF core with its silica cladding etched by hydrofluoric solution [63]. (d) Illustration of SCF structure with the interface modifier [63]..... 33

Figure 3.2 Fabrication process of MCD with CaO interface modifier. 34

Figure 3.3 (a) SEM image at core/cladding interface of the as-drawn SCF [54]. (b) Microprobe data of the cladding core interface. (c) Microscope image of silicon core (backlight illumination). 35

Figure 3.4 (a) Diagram of Vytran GPX-3300 glass processor. (b) Photo of Vytran is tapering a fibre. 36

Figure 3.5 (a) Microscope (Vytran) image showing a SCF inside of a silica tube. The red dashed line shows the starting position of the filament to obtain complete fusion. (b) Microscope (Vytran) image showing perfect fusion of the tube and SCF in (a). (c) Schematic of perfect fusion between the silica tube and a SCF. 38

Figure 3.6 Splicing SMF to SCF as mechanical support before tapering. Image taken from Vytran microscope. 39

Figure 3.7. Measured fibre profile of a tapered SCF. Inset is a microscope image of the SCF.... 40

Figure 3.8 Diagram of single sweep tapering process. 40

Figure 3.9 (a) Schematic of model used for numerical modelling of the tapering process. The blue and red lines show the small profile change before and after pulling in a small amount of time. The grey and green lines show the changes in the viscosity distribution. (b) Viscosity distribution of a fibre during tapering process..... 42

Figure 3.10 Simulated taper profile evolution (y axis is normalised outer diameter of the fibre). (a) Fixed tapering ratio of 0.5 with 0 mm target down transition length. (b) Fixed tapering ratio of 0.5 with a 3 mm down transition length. The dotted line is to guide the eye to the designed fibre waist diameter.....44

Figure 3.11 Microscope image showing SCF with core breakup (top) and SCF with continuous core (bottom). 45

Figure 3.12 A typical tension curve for a SCF during the tapering process. 46

Figure 3.13 (a) Microscope image of a SCF sample in cross section view. (b) Microscope image of a large core SCF after polishing. (c) Microscope image of a SCF with a nanoscale core. (d) Illustration of the SCF sample preparation before polishing. 47

Figure 3.14 Sample preparation of SCFs for high-power applications. 48

Figure 4.1 Common allotropes of silicon. 50

Figure 4.2 Raman response of the a-Si, p-Si and c-Si [95]. 50

Figure 4.3 Lattice spacing of diffraction spots measured using XRD along tapered and untapered as-drawn SCF. 51

Figure 4.4 Loss measurement using cutback method. 51

Figure 4.5 Schematic of transmission characterisation setup. Mirror (M), beam-splitter (BS), microscope objective lens (L), charge-coupled device camera (CCD), photo detector (PD). 52

Figure 4.6 Cutback measurements of a SCF at 1.55 µm. (a) Insertion loss at different lengths. (b) The lowest loss obtained with various SCF core diameters. The red dashed line is a guide to the eye. 53

Figure 4.7 Schematic of multiple wavelength transmission characterisation setup. Mirror (M), beam-splitter (BS), microscope objective lens (L), charge-coupled device camera (CCD), photo detector (PD), patch cord (PC), acousto-optic tunable filter (AOTF), supercontinuum laser (SC). 54

Figure 4.8 Losses of various core diameters solar grade tapered SCF at different wavelengths. Dashed lines are guides to eye. 54

Figure 4.9 Schematic of a Fabry–Pérot cavity formed by SCF. I_0, I_r and I_t are input, reflected and transmitted light intensity. 55

List of Figures

Figure 4.10 Experimental setup for Fabry–Pérot cavity measurements. 56

Figure 4.11 Spectra response of the SCF Fabry–Pérot cavity. 57

Figure 4.12 Schematic of the transmission setup. Beam-splitter (BS), photo detector (PD1 & PD2), microscope objective lenses (L1 & L2), CCD Cameras (CCD1 & CCD2), optical spectrum analyser (OSA). 59

Figure 4.13 (a) Transmission loss measured by the cutback method compared with the Fabry–Pérot method. (b) The coupling loss at different wavelengths. 60

Figure 4.14 (a) Nonlinear absorption measurements for different pump wavelengths. The solid curves are the simulated fits for the corresponding wavelength given in the legend. (b) Measured TPA parameter as a function of wavelength, together with data points from measurements by other groups [97], [98]. Error bars represent the uncertainty in the input powers. Dashed line is theoretical fits based on calculations of Garcia and Kalyanaraman [101]. 61

Figure 4.15 Pulse duration of the OPO measured by a mid-IR auto-correlator. The red dashed line is a guide to the eye. 62

Figure 4.16 Spectral evolution with different coupled peak intensities at 1.54 µm. 63

Figure 4.17 Experimental transmission spectra as a function of pump centre wavelength: (a) 1.75 µm, (b) 1.85 µm, (c) 1.95 µm and (d) 2.15 µm. The dashed lines are numerical fits obtained by solving the generalised NLSE. The normalised spectra are offset for clarity. 63

Figure 4.18 (a) Wavelength dependence of the Kerr nonlinear coefficient n_2 for a tapered SCF. Error bars represent the uncertainty in the input pulses power. (b) Wavelength dispersion of the FOM_{NL}. 64

Figure 5.1 Summary of SCG in silicon-based waveguide in recent 10 years. 68

Figure 5.2 (a) Simulated absorption map in dB/cm as functions of wavelength and fiber core diameter. (b) Contour map of GVD parameters $\beta 2(\mathrm{ps}2/m)$ as functions of fiber core diameter and wavelength. The pink areas in (a) and (b) shows when $\beta 2$ lies between -0.5 and 0. 69

Figure 5.3 Flow chart of the NLSE modelling for propagation in a tapered SCF pumped by an ultrafast laser. 71

Figure 5.4 Experimental setup of SCG in a SCF. The pulsed pump source is coupled into the tapered SCF with a lens (L1). The output light is collected with a second lens (L2) and measured by an OSA or a Monochromator. Beam splitters (BS1 and BS2) are used to direct light at the fibre input and output facets onto CCD cameras (CCD1 and CCD2) to monitor the coupling. 72

Figure 5.5 SCG spectra from a 2 µm core SCF. (a) Pumped at λ = 2 µm. (b) Pumped at λ = 2.1 µm. (c) Pumped at λ = 2.15 µm, λ = 2.25 µm and λ = 2.35 µm. (d) λ = 2.15 µm with different pump powers. 73

Figure 5.6 SCG in a straight 3 µm core diameter SCF pumped at 2.4 µm.....74

Figure 5.7 Schematic of the asymmetric taper design. 76

Figure 5.8 (a) Fibre profile with the corresponding ZDW when the pump wavelength is at 2.4 µm. (b) The beam profile from a mid-IR camera (Pyrocam IIIHR, Ophir Optronics). (c) The mode image from the output of the fibre in the CCD camera. 77

Figure 5.9 (a) SCG spectra generated in the tapered SCF, pumped at 2.4 µm with increasing coupled average power. (b) Wavelength tuning of the pump. 78

Figure 5.10 (a) Dispersion properties of the tapered SCF at the pump wavelength of λ = 2.4 µm. (b) Effective mode area of the tapered SCF at the pump wavelength of λ = 2.4 µm. 79

Figure 5.11 NLSE simulation of the SCG in the tapered SCF with 520 W pulse peak power. (a) Spectral evolution along fibre. (b) Pulse propagation along the fibre.....79

Figure 5.12. Spectrogram of the SCG at different fibre locations. (a) At 6 mm along the fibre. (b) At 12 mm along the fibre.....80

Figure 5.13 (a) Simulation of SCG evolution in a straight SCF with a 2.8 µm core diameter and 1.5 kW coupled pump power at λ = 3 µm. (b) Simulated SCG spectra with different down taper transition lengths. 81

Figure 5.14 (a) Fibre profile with the corresponding ZDW when pumped at 3 µm. Inset is the schematic of the fibre. (b) The beam profile from a mid-IR camera (Pyrocam IIIHR, Ophir Optronics). (c) The mode image of the SCG from the output of the fibre in the CCD camera....81

Figure 5.15 (a) Mode overlap of a Gaussian beam and the two lowest order LP_{0m} modes in the SCF with a 10 µm core diameter at a 3 µm pump wavelength. (b) Percentage of the fundamental mode for different input beam waist radi. 82

Figure 5.16 Transmission properties of the tapered SCF at different wavelengths. The error bars are from uncertainties of the coupling efficiency. 83

Figure 5.17 (a) Experimental spectral broadening as a function of coupled average input power. The wavelength converted peaks associated with FWM (FWM sidebands SB1 and SB2) and DW emission are labelled in the top spectrum. Black arrow shows the CO2 absorption dip. (b) Comparison of SC generation with different pump wavelengths. 84

Figure 5.18 Output SC power versus coupled power, average power (bottom) and peak power (top), for the tapered SCF. Black line indicates linear loss. 85

Figure 5.19 (a) Dispersion properties of the tapered SCF at the pump wavelength of λ = 3 µm. (b) Effective mode area of the tapered SCF at the pump wavelength of λ = 3 µm. (c) Numerical simulation results for SC spectra generated in the tapered SCF when pumped at 3 µm. 87

Figure 5.20 (a) Simulated spectral evolution of the SC along the tapered fibre on a normalised log scale. (b) Simulated temporal evolution of the SC along the tapered fibre for the maximum coupled peak power of 1.19 kW. The colour bar shows the peak power in kW. 88

Figure 5.21 (a) Spectrogram of the SCG at different fibre locations. The scale of the horizontal axis is shown as scale bar. (b) Input and output SCG pulses in the time domain. 89

Figure 5.22 Simulated coherence with quantum noise and intensity fluctuations (5% in purple and 1.3% in red) together with the simulated SC spectra with + 5% and -5% differences of the highest input power in Fig. 5.19 (c). 90

Figure 5.23 (a) Tapered SCF profile. (b) Simulated SC spectra with different coupled peak powers. 91

Figure 5.24 Simulation result for optimised taper profile. (a) Spectra evolution along the SCF. (b) Pulse evolution along the SCF. 91

Figure 6.1 (a) Schematic of SMF integration with the SCF nanospike. (b) Fundamental mode profile in a SCF with different core diameters at λ = 1.55 µm. (c) Mode overlap between silicon tip and SMF as a function of tip diameter at λ = 1.55 µm. 94

Figure 6.2 (a) Microscope image of a SCF with nanospike. The rainbow colour on the nanospike indicates the smoothness of its tip. (b) SEM image of the naked nanospike with the silica cladding etched. 95

Figure 6.3 Fabrication of the nanospike and splicing with SMF. (a) Sample preparation of the SCF. The SCF is inserted into a silica tube for mechanical support and also to increase the cladding thickness. (b) SCF with nanospike forms between the waist and down transition region. (c) Cleaved SCF is spliced with SMF. 96

Figure 6.4 (a) Splicing of nanospike with SMF using commercial arc splicer. (b)-(c) SCF with nanospike before and after splicing with SMF. The glass tube is fused with the SCF cladding. (d)-(e) SCF with nanospike before and after splicing with SMF. The glass tube is not fused with the SCF cladding. 97

Figure 6.5 (a) Optical characterisation setup used for loss measurements. (b-d) Output mode images measured from the CCD camera without the pinhole for the different samples, as labelled. 98

Figure 6.6 (a) Schematic of the SCF nanospike integration with tapered SMF. (b) Mode profile of SCF with same 10 µm diameter cladding and different core diameters at λ = 1.55 µm.....99

Figure 6.7 Illustration of void gap formation of SCF. Lower image shows the microscope image of a SCF with a void gap. 100

Figure 6.8 Fabrication of the nanospike and splicing to a tapered SMF. (a) Gap formation in the core of the SCF. (b) Tapering the SCF and formation of the nanospike. (c) Cleaving near the nanospike. The inset shows the cleaved facet. The scale bar is 10 µm. (d) Splicing of the tapered SCF with a tapered SMF. (e) Remove the up transition of the tapered SCF by cleaving. The inset photo shows the cleaved facet. The scale bar is 10 µm.....100

Figure 6.9 (a) Microscope top view of the cleaved fibre and blade. (b) Cleaving of the 30 µm core fibre. (b) Splicing of the 30 µm core fibre. 102

Figure 6.10 Schematic of the light transmission in the SMF-SCF devices.....103

Figure 6.11 Optical characterisation setup used for loss measurements. (b) IR camera image of the output mode profile. (c) Simulated power profile of the output mode. (d) Experimental output mode profile image taken by a beam profiler. (e) Output mode profile after spatial filtering of the cladding guided mode.....104

Figure 6.12 (a) Loss measurements with a linear fit to the data. Inset schematically shows cut-back positions where the tapered SCF was cleaved. (b) Simulated coupling efficiency as a function of the spike length and cladding diameter using 3D model in COMSOL.....105

List of Figures

Declaration of Authorship

Print name:	Haonan Ren

Title of thesis:	Fiberised silicon photonics for infrared nonlinear applications

I declare that this thesis and the work presented in it are my own and has been generated by me as the result of my own original research.

I confirm that:

1. This work was done wholly or mainly while in candidature for a research degree at this University;
2. Where any part of this thesis has previously been submitted for a degree or any other qualification at this University or any other institution, this has been clearly stated;
3. Where I have consulted the published work of others, this is always clearly attributed;
4. Where I have quoted from the work of others, the source is always given. With the exception of such quotations, this thesis is entirely my own work;
5. I have acknowledged all main sources of help;
6. Where the thesis is based on work done by myself jointly with others, I have made clear exactly what was done by others and what I have contributed myself;
7. Parts of this work have been published as: See List of Publications

Signature:		Date:	

Acknowledgements

It was a challenging and exciting journey to complete my PhD program here in Optoelectronic research centre, University of Southampton. It was also filled with joys and tears. Here I would acknowledge a few people who provide great help and care in this journey.

I would like to thank Prof. Anna Peacock for the guidance and supervision during my PhD studies, also for the strong support for providing an excellent working environment and academic atmosphere. It is a great honour and luck to be accepted as PhD candidate by her. I am sincerely grateful for this offer. As my second supervisor, I would also thank Prof. Goran Mashanovich for the useful and interesting lectures given at the beginning of my PhD studies.

Then I would like to thank my parents who teach me the principle to be a kind human being. The fundamental of academic research is curiosity, it is my parents who cultivate this deeply in my mind.

Then I would like to thank Prof. Ursula Gibson, Dr. Noel Healy, Dr. Sakellaris Mailis, Dr. Swe Zin Oo, Dr. milos nedeljkovic for the delightful collaborative working experience and academic discussion.

Then I would like to thank Dr. Antoine Runge, Dr. Ozan Aktas and Dr. Li Shen for their great help in the research work. They are excellent researchers who provided me inspiring ideas, great help and guidance in the laboratory work and academic writings. Also, many thanks to my colleges, Dr. Yohann Franz, Dr. Haojie Zhang, Dr. Peter Shardlow, Dr. Lin Xu, Dr Yujun Feng, Dr. Shaoxiang Chen, Huaiqin Lin and Dr. Sijing Liang for their help in the daily work and sharing knowledge and laboratory equipment.

Definitions and Abbreviations

3PA	Three-Photon Absorption
A-Si	Amorphous Silicon
A-Si:H	Hydrogenated Amorphous Silicon
Cao	Calcium Oxide
C-Si	Crystalline Silicon
CVD	Chemical Vapour Deposition
CW	Continuous Wave
FCA	Free Carrier Absorption
FCD	Free Carrier Dispersion
FEM	Finite Element Method
FOM	Figure of Merit
FSR	Free Spectral Range
FWHM	Full Width Half Maximum
FWM	Four-Wave Mixing
GVD	Group-Velocity Dispersion
GNLSE	Generalise Nonlinear Schrödinger Equations
HPCVD	High Pressure Chemical Vapor Deposition
HNLF	Highly Nonlinear Fibre
MCD	Molten Core Drawing
MI	Modulation Instability
mid-IR	Mid-Infrared
MMI	Multimode Interference
MPA	Multiphoton Absorption
NA	Numerical Aperture
NIR	Near-Infrared
NLSE	Nonlinear Schrödinger Equation
OPO	Optical Parametric Oscillator
Pbse	Lead Selenide
PC	Polarisation Controller

PCF	Photonic Crystal Fibre
P-Si	Polycrystalline Silicon
RMS	Root Mean Square
SEM	Scanning Electron Microscopes
SC	Supercontinuum
SCG	Supercontinuum Generation
SMF	Single Mode Fibre
SOI	Silicon-On-Insulator
SOS	Silicon-On-Sapphire
SPM	Self-Phase Modulation
TE	Transverse Mode
TPA	Two-Photon Absorption
ZDW	Zero-Dispersion Wavelength
Znse	Zinc Selenide

Chapter 1 Introduction

1.1 Fiberised nonlinear silicon photonics

Silicon is the second most abundant element on earth's crust. It plays an important role in the modern industrial world for its special properties. It is thermally stable, chemically inert and non-toxic [1]. As a semiconductor, it has useful electrical conductivity properties that positions it between insulators and metals in the periodic table, and which can be controlled by introducing dopants into the material. Thus, silicon is widely used in the electronics industry for semiconductor devices, such as integrated circuits and solar panels. Moreover, silicon is also a useful photonic material as it has a wide transmission window that extends from 1 μm up to 8 μm. Silicon photonics has been studied extensively in terms of passive and active devices since mid-1980s [2]. Drawing on advanced CMOS fabrication technologies, silicon photonic devices can be produced at relatively low cost, making them promising platforms for integrated on-chip photonics. Numerous photonic devices have been successfully demonstrated, such as resonators [3], modulators [4] and optical multiplexers [5]. However, most of these devices are still under development in research laboratories and have yet to be fully adopted by industry.

Silicon also has attractive nonlinear optical properties. It is a highly nonlinear material that has a Kerr nonlinear index two orders of magnitude larger than silica. It also has a high damage threshold and so can tolerate high light intensities from ultrafast lasers. It has a high refractive index so that light can be confined tightly within nano-sized waveguide structures. As a result, intense interest has been devoted to the demonstration of nonlinear silicon devices such as all-optical switches [6], Raman lasers [7] and parametric amplifiers [8], supercontinuum generation [9], and frequency combs [10]. Although much of the early work was focused on the telecommunications band, owing to silicon's high nonlinear absorption in this region, in the past 10 years attention has turned to the mid-infrared (mid-IR) spectral region, where it exhibits a higher nonlinear figure of merit (FOM). The mid-IR is an important spectral region for applications in medicine, food production, environmental monitoring, and security [11]. However, the transmission window of conventional silicon photonics devices, constructed from the silicon-on-insulator (SOI) platform, are limited to the shortwave infrared (SWIR) band. A few complex structures have been developed to extend the transmission window to the mid-wave infrared (MWIR) band, such as silicon-on-porous silicon [12], silicon-on-sapphire [13], silicon-on-nitride [14], suspended silicon waveguide [15] and silicon pedestals [16]. However, these platforms encounter different challenges such as increased fabrication complexity, robustness and device quality.

In addition to the challenges associated with the chip design , there are also hurdles to robustly integrate planar-based silicon photonics devices with widely used optical fibre systems [17]. The most significant problem is how to couple light efficiently into these nano-sized waveguides. Currently, there are two mainstream coupling methods used between fibre and chip-based waveguides: edge coupling and grating coupling, as shown in Fig. 1.1. The coupling efficiency of the former is modest when coupling light directly from an optical fibre to a nanometre sized waveguide due to the huge mode mismatch. As a result, this method is often assisted by a spot size converter (SSC), which is basically a section of tapered waveguide. However, this method lacks practicality as it requires precise alignment when packaging. The second method uses waveguide gratings, by which light can be coupled into the waveguide from an out of plane direction with a relatively large spot size. However, it has less efficiency, narrow bandwidth and polarisation dependency [17]. Furthermore, both of these methods cannot avoid free space light propagation between the fibre and chip, which reduces the robustness of the device. To date, there is still a need for a compact, fibre integrated infrared photonics platform that takes advantage of the numerous optical properties of silicon.

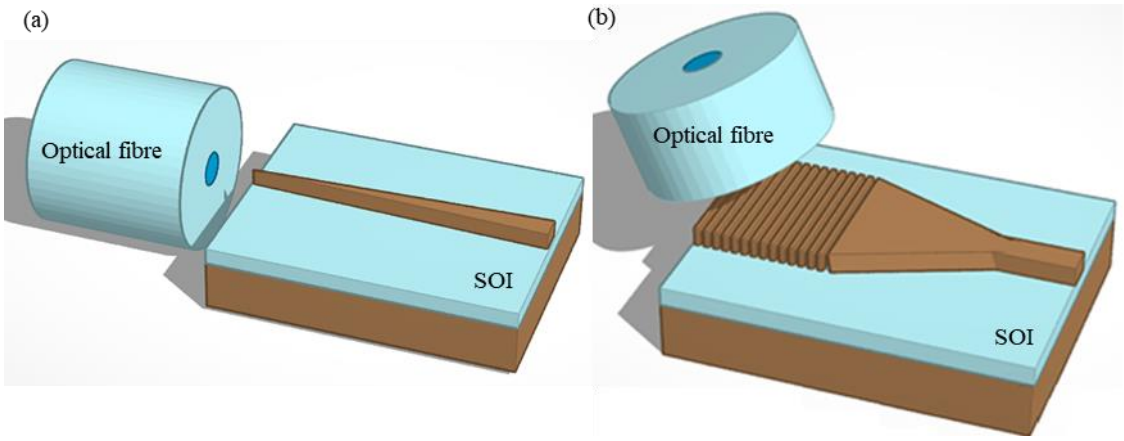

Figure 1.1 Coupling strategies between an optical fibre and a silicon planar waveguide. (a) Using a SSC. (b). Using a grating coupler.

1.1.1 Silicon core fibre

Following the invention of laser in 1960, optical fibres technologies have developed rapidly as a means to steer the light over long paths. They are not only the foundation of modern communication systems, but also used in many other fields, such as sensing, imaging and nonlinear photonic applications. However, conventional silica optical fibres have many limitations in terms of their transmission window and functionality. Efforts have been made to develop optical fibres with different core materials for specific optical functions. The silica-clad, silicon core fibre (SCF) emerged in the past decades as a novel fibre platform that incorporate silicon photonics into

conventional silica fibre technologies. It has been investigated for various of applications in photonics and optoelectronics including optical signal processing [18], [19], supercontinuum generation (SCG) [20], and solar cells [21]. As an intermediate platform between on-chip silicon devices and conventional optical fibres, the SCFs combine characteristics of both, with some additional useful features. Compared with chip-based waveguides, the SCFs benefit from the fibre geometry, so that they offer the potential to be robustly spliced with other fibre based optical systems. Fig. 1.2 shows a concept plan for SCF device integration in a standard fibre system. The silica cladding provides protection to the core from the surrounding environment. SCFs can also be made with a larger variation in core sizes, which can be fabricated from a few hundreds of micrometres to nanometre scales, to provide a wider range of modal properties than their planar counterparts. Compared with conventional fibres, SCF offers much higher nonlinear coefficients and tighter light confinement for nonlinear light manipulation. The nonlinearity parameter of the SCFs is usually 2-3 orders of magnitude higher than conventional nonlinear fibres. Furthermore, it has unique optoelectronics properties that can expand the range of potential fibre applications.

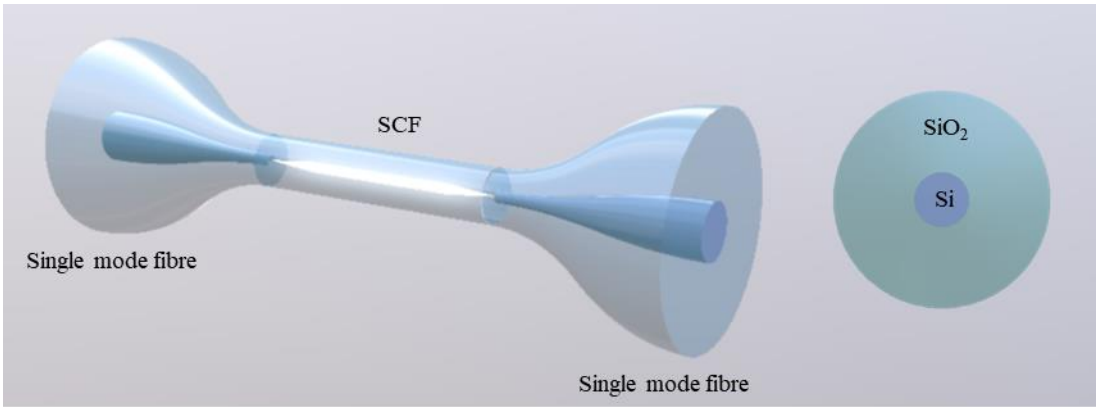

Figure 1.2 Concept plan of a SCF device in a standard fibre system. On the right shows the cross section of a SCF.

There are two main methods for SCF fabrication. The first SCF was fabricated by depositing silicon inside a silica capillary via the high-pressure chemical vapour deposition (HPCVD) method [22]. However, this method was time consuming and only produced fibres with centimetre lengths. Shortly after this initial work, a more flexible method was proposed, the so called “molten core drawing (MCD)” method, that made use of a conventional fibre drawing tower and so can produce fibres over much longer lengths, making the MCD fibres cheaper to produce [23]. Therefore, the SCFs used in this thesis were fabricated by the MCD method. Although the core sizes of the MCD fibres are typically quite large (>10 μm), recently our group developed a post-processing tapering procedure that can controllably reduce the fibre dimensions, while at the same time improving the material quality of the silicon core, making them more suitable for nonlinear applications [24].

Although the SCFs produced from the MCD method looked to be a promising platform for compact nonlinear photonics devices, they still required further development. Firstly, the optical properties of the SCFs fabricated from the post-processing tapering were not fully characterised. Also, as the research direction of the fibre optics community is gradually moving to the mid-IR band, there is an increasing demand for the optical characteristics of the SCFs to be optimised for use in this new wavelength region. However, the linear and nonlinear transmission properties of tapered SCFs were previously only characterised in the telecommunication band [24]. Secondly, few nonlinear optical devices were demonstrated using tapered SCFs. Thirdly, as SCFs are high-index core fibres, there was a strong demand for establishing a method for robust integration with standard fiber infrastructure. Hence, the main goal of this project was to exploit the potential of the tapered SCF for all-fiberised nonlinear photonic devices extending beyond the telecoms band and into the mid-IR. Specifically, in this thesis, the linear and nonlinear optical properties of the tapered SCFs are characterised from the near-to mid-IR region. Wide band supercontinuum generation in the mid-IR is studied. A robust, low loss all-fibre integration method for subwavelength SCF is proposed and demonstrated. These studies pave way to next generation all-fibre nonlinear optical systems.

1.2 Literature review

1.2.1 From integrated circuit to nonlinear silicon photonics

After the integrated circuit (IC) emerged in the 1960s, the gate length of a single transistor has been reducing at an incredible speed from 10 μm in the early 1970s to below 10 nm nowadays. With this enormous success of the silicon fabrication technology, it is easy to associate the silicon chip fabrication technology with photonics, as silicon can also be used to make optical devices by virtue of its distinguished photonic and optoelectronic properties. The initial concept of silicon photonics was raised by Richard Soref in 1986 [2]. In this early work, he demonstrated an optical power divider using a planar silicon waveguide operating at 1.3 μm. Several light manipulation schemes were proposed, including using the free carrier effects and Kerr nonlinear effects. These waveguides were produced using epitaxially grown high resistance silicon on a heavily doped silicon substrate. However, they had high propagation losses, which were caused by weak light confinement and large cladding leakage. Following Soref's work, other platforms such as (SOI) [25], silicon-on-sapphire (SOS) [26], and silicon-germanium-on-silicon [27] were reported around 1990. Among these platforms, SOI has prevailed in the near infrared region for its low cost and low cladding refractive index [1]. The large refractive index contrast of silicon and silicon dioxide offers a tighter light confinement, which reduces the substrate leakage and allows for smaller scale devices. To

date, SOI waveguides with nanoscale dimensions can have transmission losses less than 0.5 dB/cm in the telecom band [28].

Within the field of silicon photonics, nonlinear optical effects have been widely studied thanks to the tight light confinement and the high nonlinear coefficients of silicon. Compared with conventional nonlinear optical fibres, silicon waveguides offer useful advantages in that they are extremely compact and offer much lower power thresholds. The power threshold is also much lower for waveguides. Like silica, silicon is a $\chi^{(3)}$ material due to its symmetric crystalline structure. Many nonlinear demonstrations have been reported based on Kerr effects, including Raman amplification and lasering, harmonic generation, parametric amplification, SCG and frequency combs.

In 2002 and 2003, spontaneous Raman scattering [29] and stimulated Raman scattering [30] were first observed in a silicon waveguides. These findings opened up the study of nonlinear silicon photonics. As the Raman gain in silicon is strong and has a narrow bandwidth, silicon waveguides are suitable for making Raman amplifiers and lasers. The first silicon Raman laser was reported in 2004, with a lasing threshold of 9 W from a pulsed pump at wavelength of 1.68 μm [31]. In the next few years, the silicon Raman laser was further developed, a continuous wave (CW) Raman laser [32] and a cascaded Raman laser [33] were reported. The laser threshold was reduced to microwatt level by photonic-crystal nanocavity in 2013 [7].

The four-wave mixing (FWM) processes have been extensively studied in silicon waveguides, as the generation of new frequencies and parametric amplification can be realised for communication and sensing applications. In 2005, FWM was first observed in a silicon waveguide in the telecom band [34], [35]. The bandwidth and gain of the FWM process in the telecom band were improved in 2006 by optimising the waveguide, pump power and phase matching [36]. This technique was soon used for signal regeneration in the telecommunication band in 2008 [37] and mid-IR band in 2012 [38].

SCG is another widely studied phenomenon in silicon photonics, as silicon has the potential to generate broadband supercontinuum thanks to its wide transmission window. SCG in silicon waveguides can be classified into two types: one is by pumping with femtosecond pulses, where the nonlinear processes are dominated by self-phase modulation (SPM) in the normal dispersion regime and soliton dynamics in the anomalous dispersion regime; the other is by pumping with relatively longer pulses or CW signals, where it is dominated by modulation instability (MI) and Raman scattering [39]. The early supercontinuum generated in silicon waveguides were pumped by picosecond pulses near the telecom band [40], [41]. The bandwidth was limited by the large nonlinear absorption in this wavelength regime. Significant improvements were made by using mid-IR pump sources to reduce the nonlinear absorption [9], [42]. Since 2014, most of the SCG in silicon

waveguides have used femtosecond pump source, as it is easier to achieve broader bandwidths than when using picosecond pumps. However, the longest wavelength achieved within an SOI waveguide is 3.6 µm [43], which is limited by the large cladding absorption due to the transmission window of silica. Broad mid-IR SCG was achieved by using the SOS waveguide [13], which enabled the spectrum to be extended up to 6 µm.

1.2.2 Silicon core fibre

Development of fabrication process

With the great successes of chip-based silicon photonics, SCFs emerged as a fiberised silicon photonic platform, which uses silicon as a core and silica as the cladding. The fibre structure of the SCFs offers the possibility for robust all-fibre silicon photonic devices. Compared to silica fibres, they also have rich optoelectronic properties and an extended mid-IR transmission window. The first silicon fibre was reported in 1996 via the micro pull down technique [44]. This technique continuously feeds a seed crystal with melted silicon through a graphite crucible. To prevent oxidation of the crucible and silicon, argon gas was flushed in the growth chamber. Bare single crystal silicon fibre was drawn to 200 µm in diameter over 15 cm in length. Similar to that of bulk silicon single crystal growth, these fibres were always grown in the <111> direction. The crystal growth mechanism was studied in this article, in terms of mass conservation, energy conservation and shape stability to produce high quality single crystalline silicon fibre. However, dislocations and subgrains occasionally appeared in these early fibres and they were not primarily considered for light guiding.

In 2006, the first glass clad silicon core optical fibre was fabricated via the HPCVD method as shown in Fig. 1.3 (a). Silicon was deposited into the hole of microstructured optical fibers (MOFs) using a silane (SiH_4) precursor in a high temperature furnace under high pressure [22]. Silane decomposes and leaves silicon on the inside walls of the capillary, which eventually forms the core of the SCF. Depending on the temperature, it can result in Hydrogenated amorphous silicon (a-Si:H) or Polycrystalline silicon (p-Si) cores [45]. The first optical SCF had a core that was polycrystalline in nature with a transmission loss estimated to be 7 dB/cm at 1.55 µm. In 2009, another SCF fabricated through a modified MOF template, as shown in Fig. 1.3 (b), was demonstrated to have a transmission loss from 5-10 dB/cm and significantly reduced the number of modes supported by the core. [46]. The loss was then reduced to 3 dB/cm at 1.55 µm in 2010 and 1.7 dB/cm by controlling the hydrogen content in the a-Si:H [47], [48]. These SCFs used silica capillaries as the deposition template instead of MOFs, as shown in Fig. 1.3 (c).

The main drawback of the HPCVD method is that the deposition process is slow and produces fibres with only a few centimetres' length. The MCD method was developed to produce long polysilicon fibres in 2008 [23]. This method fabricates polycrystalline SCF by adapting the convention fibre drawing technique. A silicon rod with a 3 mm diameter was drilled out from a single crystal boule and inserted into a thick silica tube with 3.5 mm inner diameter and 5 mm outer diameter. The fibre was drawn at a rate of 2.7 m/min, at around 1950 °C, which is above the melting temperature of silicon, so that the molten silicon fills the silica tube, leaving no gap between core and cladding. The resulting fibre had a large core/cladding diameter (60-120 µm/1-2 mm) and a length of 30 m, as shown in Fig. 1.3 (d). However, this initial drawn fibre had a high defect density, with only a 5 cm section of fibre shown to be "bubble free". The measured transmission of this fibre was measured to be 2.7 dB/cm at 1.3 µm and 0.043 dB/cm at 2.9 µm, as the large core size reduced the effects of scattering loss from the core cladding boundary. Following this work, efforts were made to reduce the core size of the drawn SCFs while maintaining low transmission losses. In 2009, the diameter of the core/cladding of the MCD SCFs were reduced to 10-100 µm/40-240 µm using a custom-made fiber drawing system [49]. Unlike the work in [23], it used high purity silicon powder filled in a silica tube instead of a silicon rod. However, this method only produced fibres with a few centimetres' length and their transmission losses were not thoroughly studied due to unknown coupling conditions.

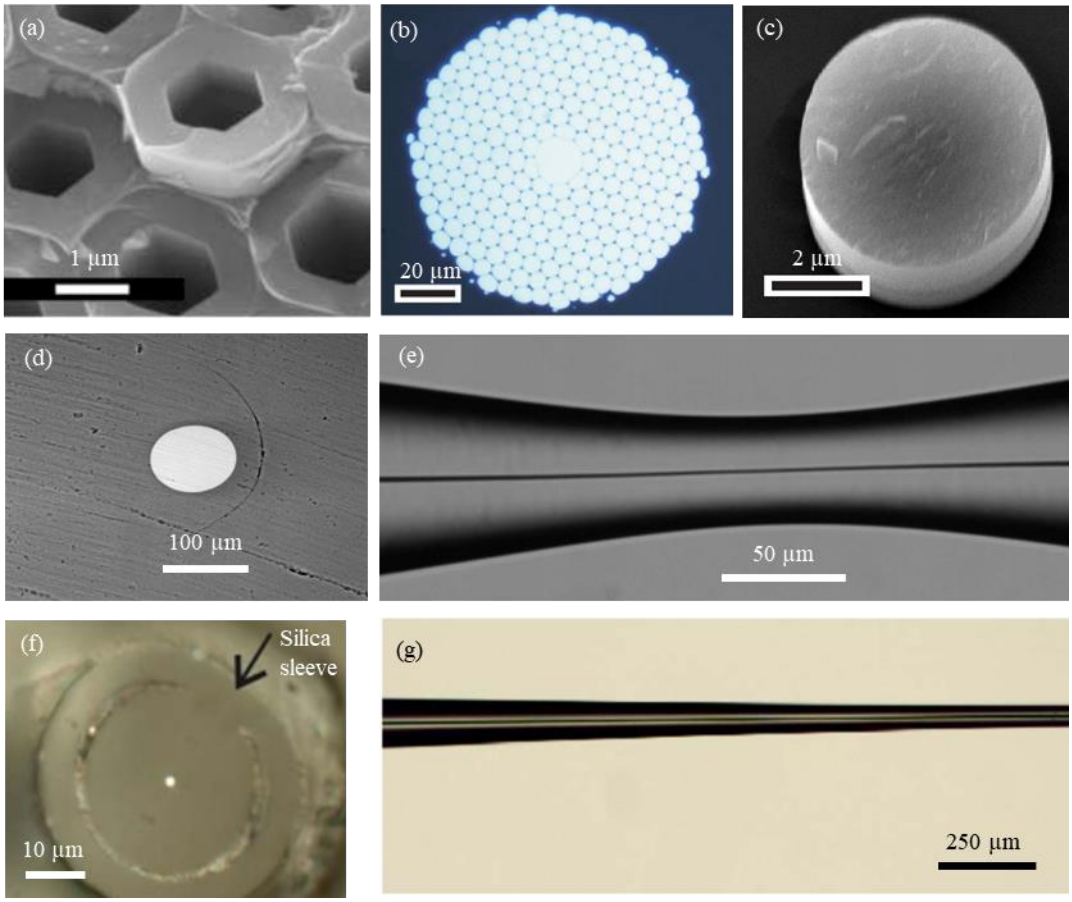

Figure 1.3 A collection of reviewed SCFs in the past decade. (a). Scanning electron micrographs (SEM) of silicon fibres deposited in a honeycomb MOF template [22]. (b). A SCF deposited in a PCF template [46]. (c). SEM of a single core SCF [47]. (d). SEM of the first MCD SCF [23]. (e) SCF after tapering by a splicer. (f)-(g). Small core SCF after post process tapering [24].

Characterisations of the crystallinity of the SCF were carried out, including studies of the effects of the core geometry, surface roughness, crystal grain boundaries, crack defect, oxygen diffusion and longitudinal perturbations [50]–[53]. It was found that defects such as bubbles and stress can be induced by chemical reactions and thermal mismatch between the silicon core and silica cladding. To eliminate these defects, in 2013, alkaline oxide interface modifiers were introduced into the SCFs as an interface layer between the core and cladding [54]. This layer can moderate the stress between core and cladding, and at the same time reduce the impurities of the silicon core and provide a gradient index of refraction. Different materials including NaO, MgO, SrO, CaO and BaO were tested. CaO and MgO modifier were considered to have the best performance. This method significantly increases the quality of the SCF in terms of uniformity, mechanical properties and defect rate. The fibre core diameter was reduced to 10 µm with the reported loss of 4 dB/cm at 1.55 µm.

In 2015, a novel drawing method using an aluminium rod inserted inside a silica tube was reported [55]. This method utilizes the reaction of aluminium and silica to produce a silicon core. However, the optical transmission property of these fibres was not measured, leaving a question mark of the optical quality of these fibres.

In 2010, tapered SCFs were first demonstrated by post-processing an a-Si:H core HPCVD SCF using a fusion splicer, as shown in Fig. 1.3 (e) [56]. The fibre core was transformed into a polycrystalline material with a smooth taper profile. This work showed that the fibre dimension could be further decreased to nanometre scale via tapering. In 2016, a modified post-process tapering method was used to reduce the losses of polycrystalline core MCD SCFs down to 3.5 dB/cm, while at the same time reducing the core diameter to 0.94 μm, shown in Fig. 1.3 (f)-(g) [24]. These fibres exhibit different transmission qualities compared to the as-drawn SCFs, as the tapered process reduces the core diameter as well as the number of grain boundaries.

Photonic applications

Following improvement in the transmission properties, various optical applications were studied in these SCFs. In general, most of these applications exploited the excellent nonlinear optical properties of the a-Si:H core fibres, which had the lowest transmission losses and smallest cores. The most studied nonlinear application in SCFs is all optical modulation near the telecommunication band. In 2007, all-optical modulation was first demonstrated in an a-Si:H core fibre using free carrier absorption (FCA) generated by a 532 nm pulsed laser [57]. An 8.3 dB modulation depth was achieved with 1.4 MHz modulation frequency at 1.55 μm. In 2011, another all optical modulation experiment was demonstrated in an a-Si:H SCF using two-photon absorption (TPA) [48]. A 40 MHz modulation frequency with a 4-dB extinction ratio was achieved at telecom wavelengths. In 2012, using a similar experiment configuration as in [48], cross phase modulation (XPM) was demonstrated in the same fibre at telecom wavelengths, with an improved 12 dB extinction ratio [18]. The first nonlinear application in a crystalline SCF was demonstrated in 2015, where optical modulation was demonstrated in a hybrid silicon-core, silica-clad microspherical resonator using the Kerr effect (Fig. 1.4 (a)) [19].

Other nonlinear phenomena were less studied, and so there is scope for further investigation. In 2010, the nonlinear transmission properties of a-Si:H core SCFs were characterised, such as the linear absorption, nonlinear refractive index and nonlinear absorption. Numerical simulation of short pulse propagation in tapered SCF was also studied. It showed that SCFs with tapered designs could be used for parabolic pulse generation as well as soliton-like pulse propagation and compression [58]–[60]. In 2014, an octave supercontinuum generation from 1.6 μm to 3.4 μm was demonstrated in an a-Si:H core SCF [20]. The fibre was 4 mm long and pumped by a femtosecond

pulse laser with peak power of 75 W at 2.5 µm. This was strong evidence that the SCFs are a suitable platform for mid-IR nonlinear photonics.

There have also been a few studies of optical devices drawing on the linear properties. In the year 2015, an all-fiber temperature sensor based on a silicon Fabry–Perot interferometer was demonstrated using a polycrystalline silicon core fibre [61]. The device was realised by splicing a single mode fibre (SMF) with the SCF, which was also the first all-fibre silicon photonic device. In 2017, Bragg gratings were written in to SCFs via laser treatments (Fig. 1.4 (c)) [62], however, their optical properties were not characterised. Other research on SCFs, such as solar SCFs (Fig. 1.4 (b)) [21], [63], [64], infrared optical detection [65], [66], and silicon nano p-n spheres (Fig. 1.4 (d)) [67] have indicated that these fibres are also suitable for optoelectronics applications.

In conclusion, significant progress has been made to the SCF platform over past decade. However, there is still a large space for the SCF technology to be further developed in terms of fabrication techniques, optical transmission, device integration with standard fibre systems and nonlinear optical applications. Being a highly nonlinear fibre, many nonlinear applications such as SCG, optical parametric amplification (OPA), Raman amplification and pulse shaping have yet to be demonstrated experimentally in the MCD SCFs. Furthermore, although silicon has a wide mid-IR transmission window, most of the early work focused on demonstrations in the telecommunication band. Prior to the work in this thesis, little research on SCFs was carried out in the mid-IR band, where increased attention is being focused in the silicon photonic community.

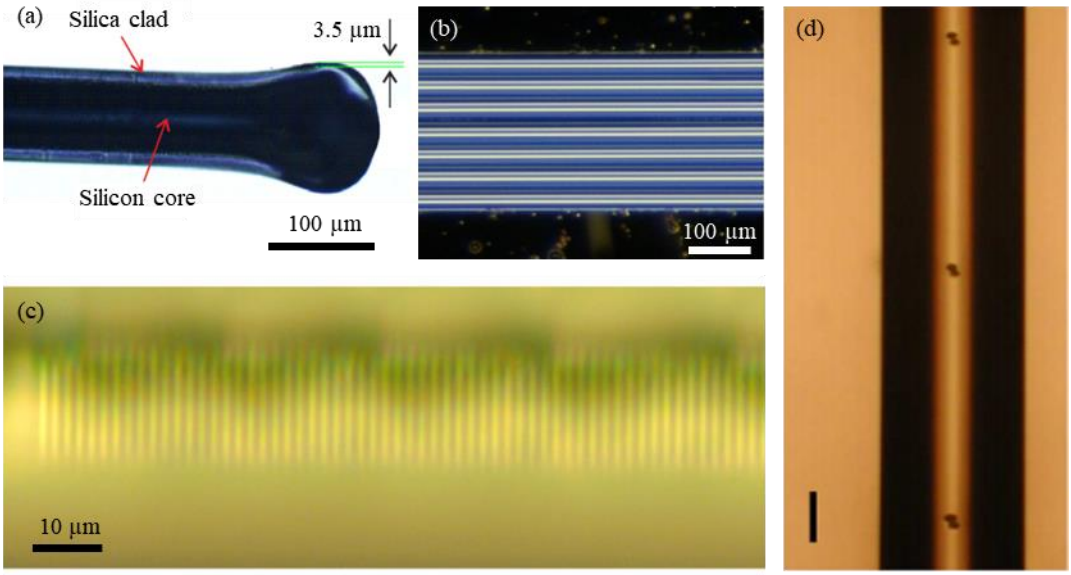

Figure 1.4 Collection of SCF devices. (a) A hybrid silicon-core, silica-clad microspherical resonator. (b) Packed solar SCF. (c) Bragg gratings written on SCF. (d) Silicon nano p-n spheres, scale bar 100 µm.

1.3 Thesis outline

Chapter 2 reviews the basic knowledge of nonlinear fibre optics. It is divided into two sections. In the first section, the optical properties of fibre waveguides are introduced. The modal behaviours and optical transmission properties of SCFs are reviewed. The dispersion properties of SCFs are studied numerically. The second section describes the nonlinear short pulse propagation in a nonlinear fibre. The physics of nonlinear light matter interactions in silicon are introduced briefly, including the third order susceptibility induced Kerr nonlinear effect and TPA. The TPA induced free carrier absorption (FCA) is also discussed. The effect of these nonlinear behaviours is studied on ultrafast pulses propagation. The pulse shape in both time and spectral domain is analysed both analytically and numerically via the well-known Nonlinear Schrodinger Equation (NLSE). I mainly focus on self-phase modulation (SPM) and soliton fission that are related to this thesis.

Chapter 3 mainly focuses on the fabrication and tapering technology of the SCFs. It starts with reviewing the fabrication of the as-drawn SCF. The tapering process for the SCFs is then studied experimentally and numerically. Firstly, the tapering rig is introduced, which talks about the machine operation and parameter settings. Two types of fibre mounting techniques for tapering are introduced, including the capillary method and splicing method. Then, the shapes of the tapered SCFs are studied experimentally and numerically. A model is built based on fluid mechanics to get a deeper understanding of the tapering process. Then the technique of tapering nanometre scale SCFs is studied with both theory and hands on experience. Some tips are provided on the criteria to achieve successful tapering of ultra-small core SCFs. Finally, the sample mounting and polishing skills are introduced.

Chapter 4 introduces the optical characterisation of the tapered SCFs. It first reviews the material properties of SCFs in previous work associated with the crystallinity of the core. Transmission measurements of the tapered SCFs with a range of different core sizes are characterised experimentally by cutback measurements for various wavelengths from the telecom to mid-IR spectral band. These results are compared with the Fabry-Pérot cavity analysis. Two types of SCFs are characterised, one is a SCF which is made from solar grade, heavily doped n-type silicon, the other is made from pure silicon. The transmission properties of both fibre types are compared and discussed. Then, the nonlinear properties of the SCFs, including nonlinear absorption and nonlinear refraction are characterised. By pumping a SCF with high intensity femtosecond pulses, the spectral broadening is recorded and fitted with numerical simulations to determine the nonlinear parameters.

Chapter 5 demonstrates broadband SCG in the tapered SCFs. It begins with a short review of recent SCG in silicon. Then the dispersion and transmission window limitation of SCFs are discussed for

efficient SCG design in the SCFs. SCG is then studied in two parts. The first part uses untapered SCFs for SCG generation and the second part uses tapered SCFs. The experimental results of these SCG are compared with simulations. The SCG process is also studied using spectrograms to obtain a deeper understanding of the pulse dynamics. Finally, the coherence properties of the SCGs are analysed with numerical calculations.

Chapter 6 describes a novel method for SCF integration with other fibre systems. A nanospike structure has been developed for efficient light coupling between SCFs and standard fibre systems. Two types of couplers using the nanospike structure are studied in this chapter. They are studied with both numerical simulation of light coupling and experimentally optical transmission characterisation. The performances of these approaches are compared and discussed. Their fabrication process is documented in detail.

Chapter 7 summarises the work that has been done to date and presents potential future work.

1.4 Key achievements

1. Characterised the linear and nonlinear transmission properties of small core tapered SCFs from telecom wavelengths to the TPA edge in the mid-IR regime. These tapered SCFs exhibit low linear loss on the order of a few dB/cm over the entire wavelength range. The obtained TPA coefficient and nonlinear refractive index revealed the high nonlinear FOM of tapered SCFs above 2 μm and the potential for these fibres to find nonlinear applications in the infrared region.

2. Demonstrated a broadband coherent 1.74 octave spanning SC generation from 1.6-5.3 μm, beyond the conventional silica absorption edge, with a ~ 60% in fibre conversion efficiency. The SC is enhanced by an asymmetrical taper structure. Further optimisation of the fibre structure could extend the spectrum to beyond 8 μm. This is the broadest supercontinuum among silicon core, silica clad waveguides. This result suggests SCFs are a viable platform for broadband nonlinear applications in the mid-IR include free-space communications, gas detection and medical diagnostics.

3. Designed, fabricated and characterised an inverse taper structure (nano-spike) on the end of a SCF that is robustly fusion spliced to standard SMFs. The estimated coupling efficiency was 4 dB, which could be further improved up to 0.2 dB by optimising the taper structure. This paves a path to all-fibre nonlinear photonic systems that can exploit the material benefit of the silicon core.

Chapter 2 Background

2.1 Introduction

This chapter reviews the fundamental background knowledge of fibre optics. In particular, it focuses on the linear and nonlinear transmission properties of step index fibres. The optical properties of fibre waveguides, including the fibre mode behaviour, mode coupling, light transmission, and dispersion are discussed. The properties of ultrafast laser pulses are introduced, followed by a description of nonlinear propagation of the ultrafast pulses in fibres. Some basics about the nonlinear light mater interaction are reviewed, including the nonlinear absorption and refraction in silicon. The nonlinear induced free carrier generation and absorption in silicon are also discussed. Then the effect of these nonlinear properties is studied on ultrafast pulses propagation. The pulse evolution in both time and spectral domains are analysed both analytically and numerically via the NLSE. I mainly focus on SPM and soliton fission as they are related to this work.

2.2 Optical properties of fibre waveguides

2.2.1 Modal properties of step index fibre

A conventional telecommunication fibre for is a long, thin cylindrical structure where light can be confined and transmitted via total internal reflection at the core and cladding interface. They are made of two layers of silica glass with different refractive indexes. They are usually a few hundred of micrometres thick and metres to kilometres long. Fig. 2.1 shows the schematic of the cross section of a conventional fibre that has a refractive index profile as a step function. The core in which light is guided has a higher refractive index than the cladding. The jacket coating is usually made of polymer that provides necessary mechanical support for the fibre, it has a higher refractive index than the cladding, which helps to remove undesired light from being transmitted in the cladding.

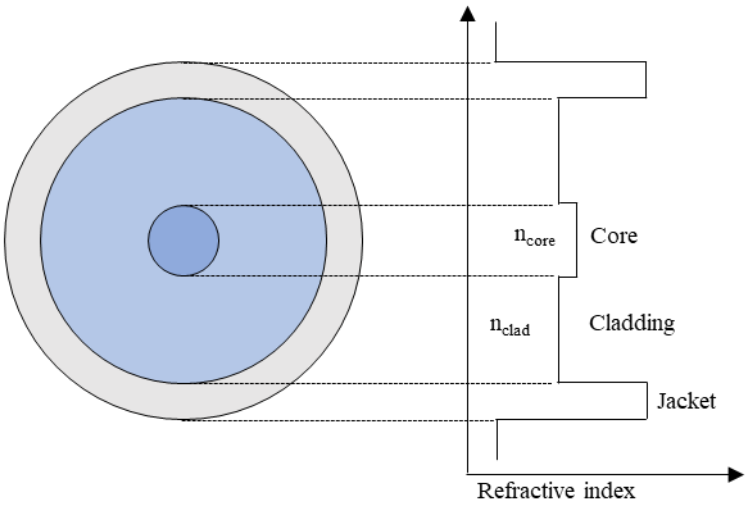

Figure 2.1 Cross sectional refractive index profile of a step-index optical fibre.

Light transmission can be studied by either ray optics where the light is treated as straight lines, or wave optics where the light is treated as electromagnetic waves. Ray optics is used as an approximation of wave optics when the wavelength is much smaller than the optical element that is being studied. The optical properties of an optical fibre are usually studied by wave optics. However, the electromagnetic wave transmission in the waveguide is rather complex, as Maxwell's equations in three dimensional fibre structures are difficult to solve. The modal studies of a fibre offer a convenient way to analyse the complex electromagnetic wave propagation. When light propagates in a fibre, the electromagnetic field in the fibre cross section can be decomposed to many orthogonal sub fields, each sub field is called a mode. Every guided mode has to be a solution of Maxwell's equations within the boundary conditions of fibre cross section. In an optical fibre where the fibre structure does not vary along the fibre axis, fibre modes are independent from each other and do not change their shape or size while propagating along the length. Two terms need to be clarified here, the supported modes are all the modes that can be guided in a fibre, whereas the modes launched into the fibre represent the actual electromagnetic fields propagating in the fibre. Each excited mode must be one of the supported modes, however, not all supported modes are necessarily excited.

To determine the mode characteristics of a step index fibre, Maxwell's equations are solved in the fibre cross section and an eigenvalue equation can be obtained as [68]

$$\{vn_{eff}\}^2\{\frac{V}{UW}\}^4 = \left[\frac{n_{core}^2 J_v'(U)}{UJ_v(U)} + \frac{n_{clad}^2 K_v'(W)}{WK_v(W)}\right]\left[\frac{J_v'(U)}{UJ_v(U)} + \frac{K_v'(W)}{WK_v(W)}\right], \quad (2.1)$$

where v is an integer, J_v is the Bessel function of the first kind, K_v is the modified Bessel function of the second kind, U, V and W are defined as:

$$U = k_0 r \sqrt{n_{core}^2 - n_{eff}^2}, \quad (2.2)$$

$$W = k_0 r \sqrt{n_{eff}^2 - n_{clad}^2}, \quad (2.3)$$

$$V = k_0 r \sqrt{n_{core}^2 - n_{clad}^2}, \quad (2.4)$$

Where r is the core radius and the effective mode index n_{eff} is the eigenvalue of Eq. (2.1). Each integer value v corresponds to a set of n_{eff}. The values of n_{eff} lie between the refractive index of fibre core and cladding. Each eigenvalue corresponds to a supported mode of the fibre. V is the normalised frequency that can be used to estimate the mode numbers of a fibre. When V is smaller than the cutoff frequency 2.405, only one eigenvalue can be found. In this case, the fibre only supports the fundamental mode and is called a single mode fibre. For large normalised frequency V, the number of modes in a step index multimode fibre, known as the mode volume, can be estimated by

$$M \approx \frac{V^2}{2}. \quad (2.5)$$

There is no analytical solution for Eq. (2.1), so it has to be solved numerically. When $v = 0$, the solutions are transverse electric (TE) or transverse magnetic modes (TM), where the electric field E or magnetic field H components are completely transverse to the fibre axis, in other words, $E_z = 0$ for TE mode or $H_z = 0$ for TM mode. With $v > 0$, the solutions are hybrid modes where all six components ($E_x, E_y, E_z, H_x, H_y, H_z$) of the electromagnetic field are non-zero. In the general case for conventional fibres, the core and cladding have a very small refractive index difference so that the light in the optical fibre is regard as weekly guided. The modes can be approximately treated as the linear polarised modes (LP modes), where E_z and H_z are relatively small so can be ignored [68]. Fig. 2.2 shows the LP_{lm} modes of a step index fibre [69]. The footnote l represents the half number of maxima of the field around the circumference and m represents the number of maxima of the field along the radius. The LP_{01} mode is called the fundamental mode of a step index fibre and is often approximated as a Gaussian distribution.

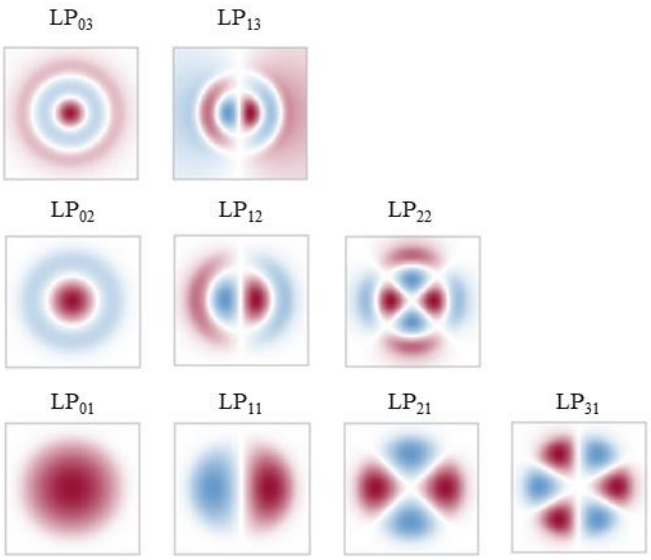

Figure 2.2 LP mode electric field amplitudes of a step-index fibre taken from Ref. [69]. The colour shows the different signs of the electric field.

The electrical filed of a mode can be represented as [70]

$$E(x,y,z) = A(\omega) \cdot F(x,y) \cdot \exp\left[j\beta(\omega)z\right], \tag{2.6}$$

where $A(\omega)$ is a normalisation constant that only related to the angular frequency ω, β is propagation constant that is related to n_{eff} as $\beta = n_{eff}k_0$, k_0 is the propagation constant in vacuum and is related to the wavelength λ as $k_0 = 2\pi/\lambda$ and $F(x,y)$ is the electric field distribution in the fibre cross section. In an optical fibre, $F(x,y)$ is usually represented as two parts in the polar coordinate system as [70]

$$F(x,y) = \begin{cases} J_0\left(\frac{U}{r}\rho\right), & \rho < r, \\ (r/\rho)^{1/2} J_0\left(\frac{U}{r}\rho\right) exp\left(-\frac{W}{r}(\rho - r)\right), & \rho > r, \end{cases} \tag{2.7}$$

where r is fibre core radius and ρ is radial distance. The mode area is quantified by the effective mode area A_{eff}. It is defined as [70]

$$A_{eff} = \frac{(\iint |F(x,y)|^2 dxdy)^2}{\iint |F(x,y)|^4 dxdy}. \tag{2.8}$$

It also can be converted to polar coordinate as

$$A_{eff} = \frac{2\pi(\int_0^\infty \rho|F(\rho)|^2 d\rho)^2}{\int_0^\infty \rho|F(\rho)|^4 d\rho}. \tag{2.9}$$

2.2.2 Modes of a SCF

SCFs have a large refractive index difference between the core and cladding. The confinement is so strong that light is tightly confined inside the core. As a result, SCFs usually exhibit multimode behaviour owing to the large V number. It cannot be treated as weakly guided fibre, however, the modal behaviour of SCFs can still be approximated as LP mode, as the fraction of E_z and H_z components in a SCF are still small enough to be ignored. Fig. 2.3 (a) and (b) show the mode field comparison of a large core SCF (with core diameter D = 10 µm) and a small core SCF (with core diameter D = 1 µm) at wavelength 1.55 µm. The electric field intensity of these modes indicates that the light confinement is tight in these fibres. The E_z components of the 10 µm fibre is negligible, whereas the 1 µm core has a small, but non-negligible, E_z component.

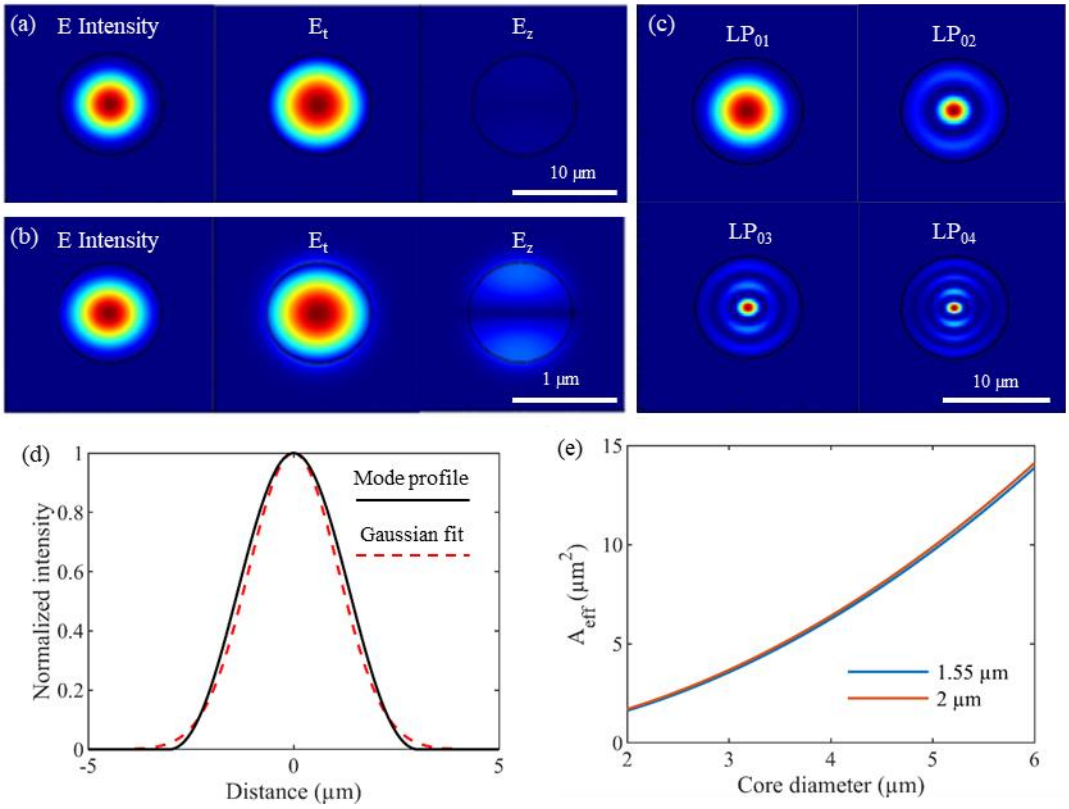

Figure 2.3 Mode characteristics of a SCF. (a) Fundamental mode profile with core diameter of 10 µm. (b) Fundamental mode profile with core diameter of 1 µm. (c) High order modes examples of SCF with a core diameter of 10 µm. (d) Mode intensity profile (fundamental mode) of the SCF with core diameter of 10 µm. The black line shows the calculated profile and red dashed line shows the Gaussian curve fit. (e) Effective mode area (fundamental mode) of SCFs at the wavelengths λ = 1.55 µm and λ = 2 µm.

Although SCFs usually have large mode volumes, in practice only the LP_{0m} modes can be excited efficiently due to the symmetry of beam profile from laser source. Fig. 2.3 (c) shows some of the higher order LP_{0m} modes of the 10 µm SCF, as these modes are more likely to be excited by a

Gaussian beam input. Fig. 2.3 (d) shows the fundamental mode profile of the 10 µm core fibre at a wavelength of 1.55 µm where the profile is fit well with a Gaussian shape. The effective mode area does not vary a lot with different wavelengths of interest, as shown in Fig. 2.3 (e).

When light is coupled into a multimode fibre such as SCF, light will excite one or more modes of the fibre with different coupling efficiencies. The coupling efficiency for each mode depends on the mode matching between the incoming beam and the modes of the fibre and can be calculated via the mode overlap integral [68]. The overlap η_{mode} between two modes (in the same direction) can be calculated by [71]

$$\eta_{mode} = \left(\frac{Re\{\int \vec{E}_1 \times \vec{H}_2^* \cdot d\vec{s}\}}{\int \vec{E}_1 \times \vec{H}_1^* \cdot d\vec{s}}\right)\left(\frac{Re\{\int \vec{E}_2 \times \vec{H}_1^* \cdot d\vec{s}\}}{\int \vec{E}_2 \times \vec{H}_2^* \cdot d\vec{s}}\right), \quad (2.10)$$

where $\vec{E}_1, \vec{H}_1, \vec{E}_2, \vec{H}_2$ are the electric and magnetic field of the two modes, $*$ represents the complex conjugate. As shown in Fig. 2.4, a laser beam is focused by a convex lens into a small spot that has a similar size to the fundamental mode of the fibre. With careful coupling into the core, it is possible to propagate most of the light in the fundamental mode [72]. When the focused spot is smaller or larger than the fundamental mode, the coupling efficiency to fundamental mode will drop, with the rest of the energy coupled to higher order mode or scattered.

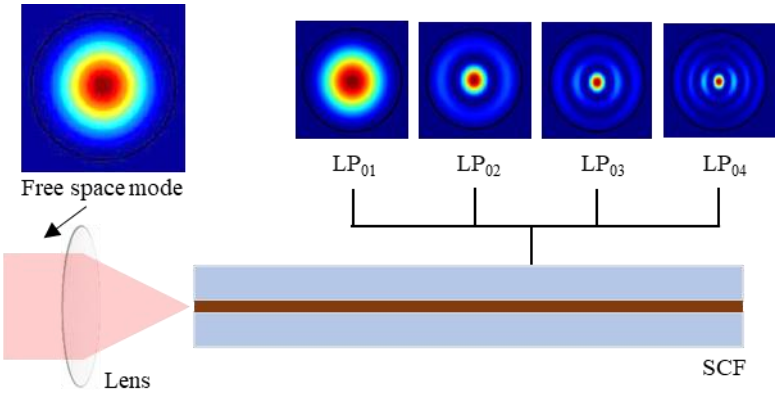

Figure 2.4 Schematic diagram of free space coupling to a SCF using lens.

2.2.3 Linear transmission

The electric field in a waveguide is often described in power intensity (power transferred per unit area) I, which is related to the electric field as

$$I = \frac{E^2}{Z_0}, \quad (2.11)$$

where Z_0 is the impedance of free space. Light attenuation in a fibre is described as

$$I(z) = I_0 e^{-\alpha z}, \quad (2.12)$$

where α is loss coefficient and I_0 is the initial power intensity. α is related to the imaginary part of the refractive index n_i as

$$\alpha = 2n_i k_0, \quad (2.13)$$

In practice, the loss per unit length is used with the relation

$$\alpha_{dB} = -\frac{10\, log_{10}\left(\frac{I}{I_0}\right)}{z} = 4.343\alpha, \quad (2.14)$$

where α_{dB} is loss in dB per unit length.

Light attenuation in crystalline silicon can be caused by many factors. The cut-off wavelength in the shorter wavelength region is mainly caused by band edge absorption, which depends on the bandgap energy of the material. Since the bandgap energy of crystalline silicon is around 1.1 eV, photons with energy above this value will be absorbed to excite electrons from the valence band to the conduction band. This sets the shortest transparent wavelength of silicon to be 1.1 µm. Below this wavelength, silicon absorbs strongly and cannot be used as a waveguide material. For longer wavelengths, absorption is caused by molecular vibrations and rotations [73]. The widely accepted cut-off wavelength is up to 8 µm, though above 8 µm silicon is still partly transparent. Fig. 2.5 shows the transmission window of silicon [74] and silica [75]. In practice, for the silicon in the SCF core, the absorption spectrum could be different, as the bandgap and molecular vibrations of silicon depend on different sample conditions such as impurity content, stress, strain and temperature.

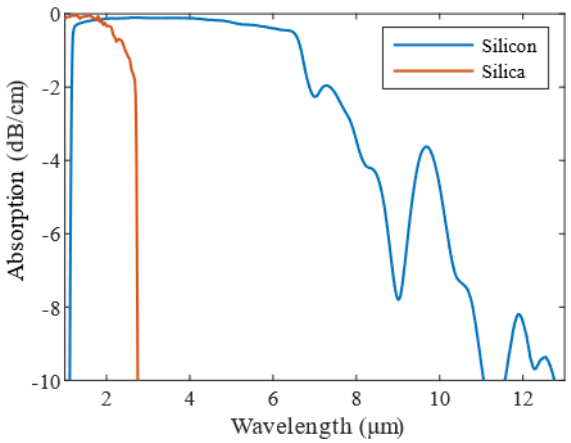

Figure 2.5 Transmission window of silicon [74] and silica [75].

Another contribution to the attenuation in a fibre is Rayleigh scattering by the impurities and imperfections in the material, such as contaminant atoms and crystalline defects. In optical planar

waveguides, it can also be caused by the surface roughness at the core cladding boundary. The surface scattering increases with increasing refractive index difference between waveguide core and cladding. However, for SCFs, the light attenuation from surface scattering is usually considered to be negligible as the fibre surfaces are very smooth [50], which is a significant advantage of this geometry. The scattering loss is a function of wavelength and exhibits a λ^{-4} dependence:

$$\alpha_R = \frac{C_R}{\lambda^4}, \tag{2.15}$$

where C_R is a constant related to the material quality and waveguide surface roughness.

2.2.4 Dispersion

Dispersion is the phenomenon when photons with different frequencies travel at different speeds in the medium. It arises primarily due to the wavelength dependence of the refractive index of the material. For waveguides, dispersion also exhibits a waveguide contribution as the effective refractive index of a mode depends both on the waveguide geometry and the material dispersion. The speed of light (phase velocity) in a medium v is related to the refractive index n as

$$v = \frac{c}{n(\omega)}. \tag{2.16}$$

The propagation constant β is defined as the phase change of the electric field over a unit length and can be expressed as

$$\beta(\omega) = \frac{d\varphi}{dz} = \frac{d\varphi/dt}{dz/dt} = \frac{\omega}{v} = n(\omega)\frac{\omega}{c}, \tag{2.17}$$

where φ is the phase of the electric field. Then the propagation constant can be expanded in a Taylor series at the central frequency ω_0 as

$$\beta(\omega) = \beta_0 + \beta_1(\omega - \omega_0) + \frac{1}{2}\beta_2(\omega - \omega_0)^2 + \frac{1}{6}\beta_3(\omega - \omega_0)^3 \ldots, \tag{2.18}$$

where β_m is the m^{th} order dispersion and can be calculated by taking the m^{th} derivative of β at ω_0. β_1 and β_2 are related to the refractive index n (n_{eff} in a waveguide) as

$$\beta_1 = \frac{1}{v_g} = \frac{n_g}{c} = \frac{1}{c}\left(n + \omega\frac{dn}{d\omega}\right), \tag{2.19}$$

$$\beta_2 = \frac{1}{c}\left(2\frac{dn}{d\omega} + \omega\frac{d^2n}{d\omega^2}\right), \tag{2.20}$$

where v_g, n_g are the group velocity and group index. Physically, β_1 governs the optical pulse envelope speed and β_2 is the group velocity dispersion (GVD) of optical pulses and responsible for

pulse envelop spreading. The dispersion parameter D is also commonly used in optical fibre systems. It is derived from β_2 as

$$D = -\frac{2\pi c}{\lambda^2}\beta_2. \quad (2.21)$$

β_3 is the third-order dispersion (TOD), which results from the frequency dependency of the β_2. It is responsible for the oscillatory structure on ultra-short pulses in time domain.

Material dispersion

When light propagates in a medium, it causes disturbance of the electron charges in the material so that they oscillate with same frequency, but with a phase difference. The combined field of the light and electron oscillation has the same frequency, but with a slower phase velocity than the original wave. This mechanism leads to refraction and reflection, according to Huygens–Fresnel principle. The refractive index of crystalline silicon and silica have been studied by various different groups. The values measured in these studies are slightly different, as samples with different material qualities and conditions were used. For convenience, we use the results from Ref. [73], [76] for silicon and Ref. [75], [77] for silica in this work. The refractive index of bulk silicon and bulk silica is a function of wavelength and temperature, which can be described by the Sellmeier equation as

$$n^2(\lambda, T) - 1 = \sum_{i=1}^{3} \frac{S_i(T) \cdot \lambda^2}{\lambda^2 - \lambda_i^2(T)}, \quad (2.22)$$

where

$$S_i(T) = \sum_{j=0}^{4} S_{ij} \cdot T^j, \quad (2.23)$$

$$\lambda_i(T) = \sum_{j=0}^{4} \lambda_{ij} \cdot T^j, \quad (2.24)$$

with the parameters shown in the Table 2.1 for crystalline silicon and Table 2.2 for fused silica.

Table 2.1 Coefficients of Sellmeier equation for crystalline silicon

	S_1	S_2	S_3	λ_1	λ_2	λ_3
T^0	10.4907	-1346.61	4.42827E+07	0.299713	-3.51710E+3	1.71400E+06
T^1	-2.08020E-04	29.1664	-1.76213E+06	-1.14234E-05	42.3892	-1.44984E+05
T^2	4.21694E-06	-0.278724	-7.61575E+04	1.67134E-07	-0.357957	-6.90744E+03
T^3	-5.82298E-09	1.05939E-03	678.414	-2.51049E-10	1.17504E-03	-39.3699
T^4	3.44688E-12	-1.35089E-06	103.243	2.32484E-14	-1.13212E-06	23.5770

Table 2.2 Coefficients of Sellmeier equation for fused silica

	S_1	S_2	S_3	λ_1	λ_2	λ_3
T^0	1.10127E+00	1.78752E-05	7.93552E-01	-8.906E-02	2.97562E-01	9.34454E+00
T^1	-4.94251E-05	4.76391E-05	-1.27815E-03	9.08730E-06	-8.59578E-04	-7.09788E-03
T^2	5.27414E-07	-4.49019E-07	1.84595E-05	-6.53638E-08	6.59069E-06	1.01968E-04
T^3	-1.59700E-09	1.44546E-09	-9.20275E-08	7.77072E-11	-1.09482E-08	-5.07660E-07
T^4	1.75949E-12	-1.57223E-12	1.48829E-10	6.84605E-14	7.85145E-13	8.21348E-10

The effect of temperature on the refractive index can be ignored in most cases as the temperature shift is relatively low, even for our high-power pulses. Fig. 2.6 shows the refractive index of silicon and the effect of temperature shift.

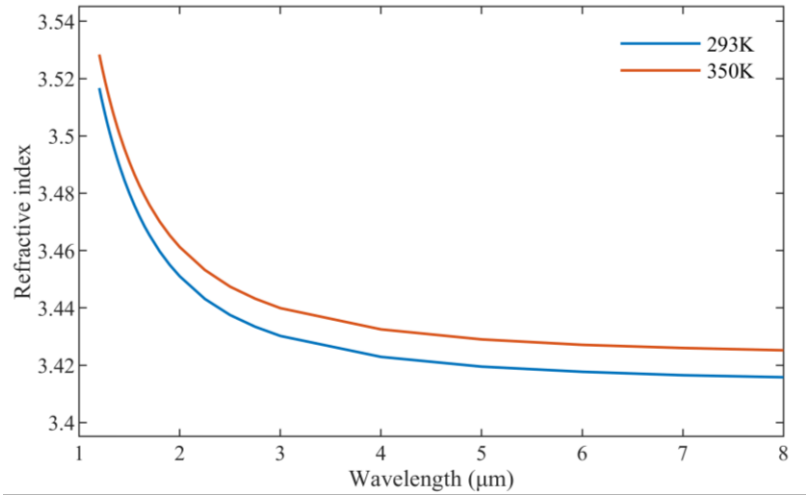

Figure 2.6 Refractive index measured by Li in 1980 at 293 K and 350K [73].

Waveguide dispersion

In an optical fibre, each mode has a different dispersion characteristic. Propagation constants of a mode can be derived from the effective mode index as

$$\beta = n_{eff} k_0 = n_{eff} \frac{\omega}{c}. \qquad (2.25)$$

Then the overall dispersion profile can be found by taking derivatives of β against ω. The waveguide dispersion can be found by subtracting the material dispersion from the overall dispersion. Total dispersion is a combination of effects due to the waveguide structure and the material dispersion from the core and cladding. For subwavelength waveguides, the waveguide dispersion dominates. For large waveguides, the material dispersion dominates. Fig. 2.7 (a) shows the numerically calculated β_2 profile of fundamental mode of SCF as a function of core size at different wavelengths. β_2 increases for larger core diameter and shorter wavelengths. The material dispersion, waveguide dispersion and overall dispersion of a 1 μm core diameter SCF is shown in Fig. 2.7 (b) for comparison.

It is obvious that in this fibre dimension, waveguide structure plays an important role to the overall dispersion.

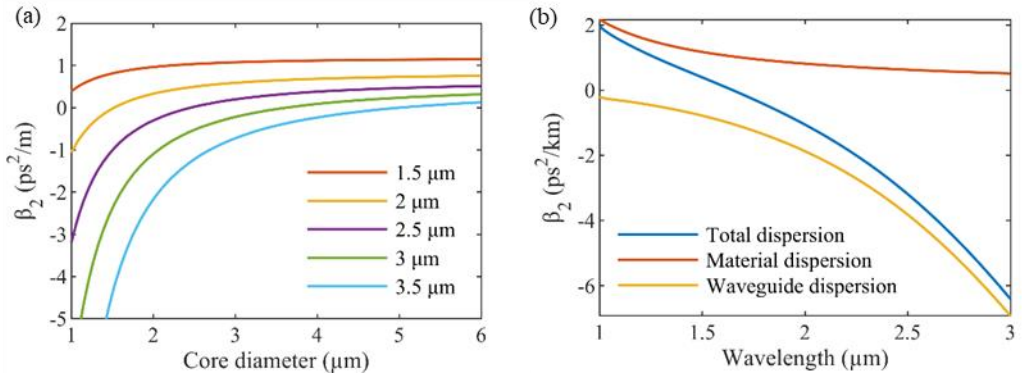

Figure 2.7 Dispersion profile of fundamental mode of SCF. (a) β_2 of SCF as a function of core size, for different wavelengths as labelled in the legend. (b) Material dispersion and waveguide dispersion contributions to a SCF with core diameter 1 μm.

2.3 Nonlinear short pulse propagation

2.3.1 Ultrafast laser pulses

Ultrafast laser pulses are typically used for nonlinear applications owing to their high peak intensity. These pulses usually have pulse durations that are of the order of picoseconds (10^{-12} s) or femtoseconds (10^{-15} s), which result in ultrahigh peak powers, up to kilowatts to megawatts levels. These peak powers make nonlinear photonics applications much easier. The electric field of an optical pulse can be described as the product of an envelop $A(t)$ with a phase $\varphi(t)$ as

$$E(t) = A(t)e^{j\varphi(t)}. \quad (2.26)$$

For convenience of study, a frame of reference is used that moves with the pulse at the group velocity. Within this frame, the time index is transformed as

$$T = t - \frac{z}{v_g} = t - \beta_1 z. \quad (2.27)$$

One common form of a pulse envelop from a laser source is a hyperbolic secant profile, which can be described as

$$A(T) = \sqrt{P_0}\,\mathrm{sech}\left(\frac{T}{T_0}\right)e^{\left(-\frac{iCT^2}{2T_0^2}\right)}, \quad (2.28)$$

where T_0 is input pulse width at $1/e$ intensity point, P_0 is the peak power of the input pulse and C is the chirp parameter of the pulse. The chirp can be caused by dispersion or nonlinear effects from

the laser source. To describe the pulse duration of a hyperbolic secant pulse, the full width at half maximum (FWHM) is defined as

$$T_{FWHM} = 2ln(1+\sqrt{2})T_0 \approx 1.763T_0. \quad (2.29)$$

The spectrum of an optical pulse can also be obtained by the Fourier transform as

$$A(\omega) = \int A(T)\, e^{-j\omega T} dT. \quad (2.30)$$

It can be found that the spectrum of a hyperbolic secant pulse also has a hyperbolic secant shape.

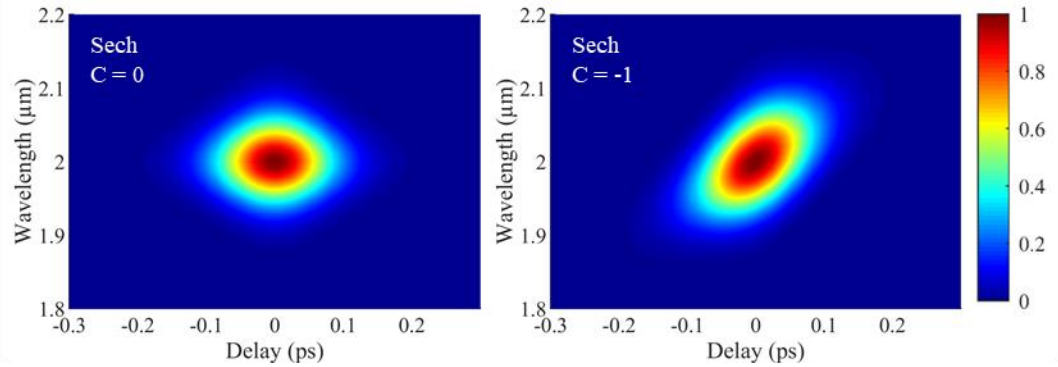

Figure 2.8 Spectrogram of a hyperbolic secant pulse with different chirp parameters. Both pulses have T_{FWHM} of 0.1 ps at wavelength of λ = 2 μm.

To study the combined temporal and spectral properties of the optical pulses, the spectrogram is introduced as a tool for mapping the spectral and time domain pulse profiles in one single image. The spectrogram of an optical can be obtained by

$$S(\omega, T) = \left| \int A(\tau) g(\tau - T)\, e^{j\omega\tau} d\tau \right|^2, \quad (2.31)$$

where $S(\omega, T)$ is the spectrogram signal, $g(\tau - T) = |A(\tau - T)|^2$ is a gate function. Fig. 2.8 shows the spectrum of both unchirped and chirped hyperbolic secant pulses, with 0.1 ps FWHM at wavelength of λ = 2 μm. When the pulse is unchirped, it is called a transform limited pulse as the pulse duration is the shortest for a given spectral bandwidth. When the pulse is negatively chirped, its shorter wavelengths are distributed more in the rising edge of the pulse, whereas the longer wavelengths are distributed more in the trailing edge of the pulse.

2.3.2 Nonlinear light matter interaction

Optical nonlinearity in a medium primarily arises due to anharmonic motion of electrons in response to an intense light beam. When the electric field is applied to a medium, the molecules in the medium are affected by this field. The polarisation is proportion to the displacement of the

positive and negative charges. Fig. 2.9 shows an illustration of electric field-induced polarisation of a molecule. For the convenience of this study where femtosecond pulsed pump is used, Raman effect can be neglected, as the pulse duration is much smaller than the phonon response time of silicon (>3 ps) to have a sufficient Raman gain [78]. The optical filed is assumed to maintain it polarisation so that a scalar approach is valid. Then the electric field-induced polarisation is typically represented as a power series as [70]

$$P(t) = \epsilon_0\left(\chi^{(1)}E(t) + \chi^{(2)}E^2(t) + \chi^{(3)}E^3(t) + \cdots\right), \quad (2.32)$$

where $\chi^{(j)}$ is the j^{th} order susceptibility. $\chi^{(1)}$ is the linear portion of the polarisation and is related to the refractive index and attenuation coefficient in the frequency domain ($\tilde{\chi}$ represents χ in the frequency domain) as

$$n(\omega) = 1 + \frac{1}{2}Re[\tilde{\chi}^{(1)}(\omega)], \quad (2.33)$$

$$\alpha(\omega) = \frac{\omega}{nc}Im\left[\tilde{\chi}^{(1)}(\omega)\right]. \quad (2.34)$$

$\chi^{(2)}$ is the second order susceptibility that can be ignored in silicon due to its symmetric crystalline structure. $\chi^{(3)}$ is responsible for nonlinear effects such as nonlinear refraction and nonlinear absorption as will be described in more detail below.

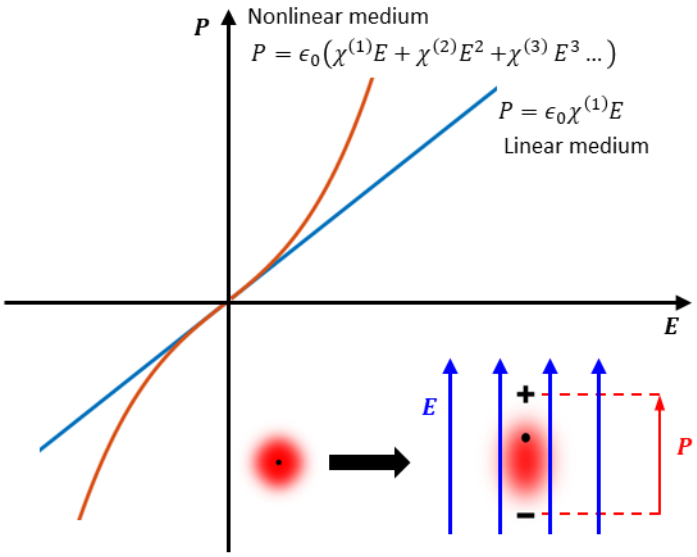

Figure 2.9 Illustration of electric field-induced nonlinear polarisation of molecules.

Nonlinear absorption

The nonlinear absorption in silicon is primarily due to TPA, where a carrier is excited from the valence band to the conduction band by simultaneously absorbing two photons, with assistance of a phonon, as shown in Fig. 2.10 (a). When two photons have the same energy, the process is called

degenerate TPA. The TPA is a nonlinear process, it happens when the light intensity is sufficiently high. To study the effect of TPA on optical transmission, we neglect all other attenuation factors, then the TPA process can be described as [79]

$$\frac{dI}{dz} = -\beta_{TPA} I^2, \tag{2.35}$$

where β_{TPA} is the TPA coefficient. Eq. (2.35) can be solved as

$$I = \frac{1}{1/I_0 + \beta_{TPA} z}. \tag{2.36}$$

When the initial light intensity I_0 is small, the term $\beta_{TPA} z$ can be neglected so $I = I_0$. When I_0 is large, the term $1/I_0$ can be neglected and $I = 1/\beta_{TPA} z$, which is defined as the saturation Intensity of TPA. β_{TPA} is related to the imaginary part of $\chi^{(3)}$ as

$$\beta_{TPA}(\omega) = \frac{3\omega}{2\epsilon_0 n^2 c^2} Im\left[\tilde{\chi}^{(3)}(\omega)\right]. \tag{2.37}$$

For silicon, the cut off wavelength of degenerate TPA is near 2.2 μm, when the total energy of the two photons is lower than the bandgap. Beyond this point, three photon absorption (3PA) dominates the nonlinear absorption. It is a $\chi^{(5)}$ process and follows similar absorption scheme as TPA.

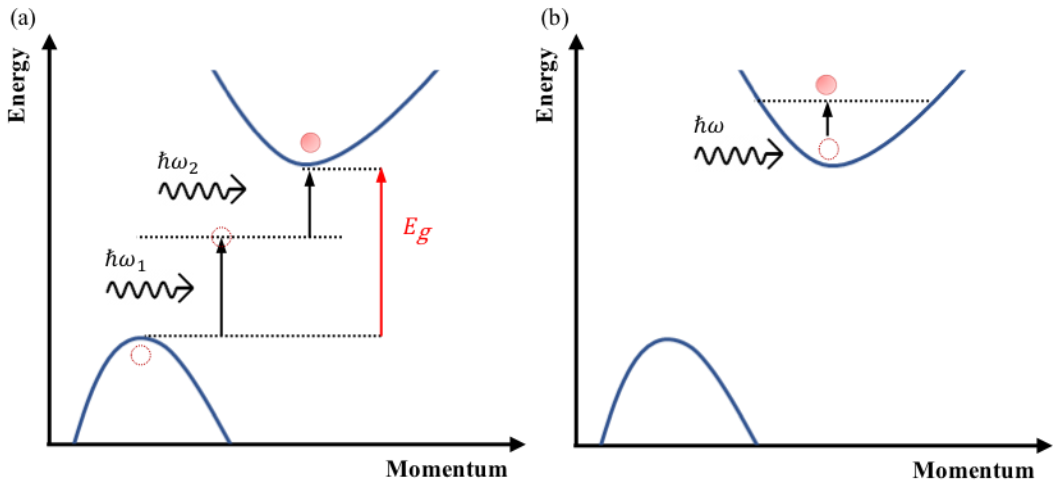

Figure 2.10 (a) TPA process in a momentum energy diagram. $\hbar$ is the reduced Planck constant and E_g is the band gap energy. (b) FCA process in a momentum energy diagram.

FCA is another light attenuation factor in silicon. It happens when a carrier absorbs the energy of a photon and is raised into a higher energy state, as shown in Fig. 2.10 (b). The light attenuation due to FCA can be described as

$$I(z) = I_0 e^{-\alpha_{FCA} z}, \quad (2.38)$$

where α_{FCA} is the loss coefficient. It is modelled as [80]

$$\alpha_{FCA} = \frac{q^3 \lambda^2}{4\pi^2 \epsilon_0 c^3 n} \left(\frac{N_e}{(0.26 m_0)^2 \mu_e} + \frac{N_h}{(0.39 m_0)^2 \mu_h} \right), \quad (2.39)$$

where N_e, N_h, are the density of free electrons and holes, ϵ_0 is the permittivity in vacuum, q is electronic charge, μ_e and μ_h are mobilities of free carriers, m_0 is the electron rest mass and c is the speed of light in free space. In the two-band approximation, the density of free electrons and holes are assumed to be equal as $N_e = N_h = N_c$. Eq. (2.39) can then be simplified as

$$\alpha_{FCA} = \frac{q^3 \lambda^2}{4\pi^2 \epsilon_0 c^3 n} \left(\frac{1}{(0.26 m_0)^2 \mu_e} + \frac{1}{(0.39 m_0)^2 \mu_h} \right) N_c = \sigma_{FCA} N_c, \quad (2.40)$$

where σ_{FCA} is FCA coefficient.

Free carriers can also modify the refractive index of the material and cause free carrier dispersion (FCD) effect. The free carrier coefficient σ that contains both FCA and FCD is described in Ref. [81] as

$$\sigma = \sigma_{FCA}(1 + i\mu) N_c, \quad (2.41)$$

where μ governs the FCD and is described as $\mu = 2k_c k_0 / \sigma_{FCA}$, with $k_c = 1.35 \times 10^{-27} m^3$.

Free carriers can be generated from the TPA process. The free carrier density induced from TPA can be described as [82]

$$\frac{dN_c}{dt} = \frac{\beta_{TPA}}{2\hbar\omega} I^2 - \frac{N_c}{\tau_c}, \quad (2.42)$$

where N_c and τ_c are free carrier density and carrier life time, $\hbar$ is the reduced Planck constant.

Nonlinear refraction

Nonlinear refraction, also called the Kerr effect, arises from the real component of $\chi^{(3)}$. It manifests as an intensity dependent change in the refractive index due to high-power light. It is one of the fundamental processes in nonlinear optics. The modified refractive index $\bar{n}$ can be described as [70]

$$\bar{n} = n_0 + n_2 I, \quad (2.43)$$

where n_2 is the nonlinear refractive index, which is related to the real part of $\chi^{(3)}$ as

$$n_2(\omega) = \frac{3}{4\varepsilon_0 n^2 c} Re\left[\tilde{\chi}^{(3)}(\omega)\right]. \quad (2.44)$$

Since the nonlinear interactions depend on both nonlinear absorption and nonlinear refraction, a nonlinear figure of merit (FOM_{NL}) is defined as

$$FOM_{NL} = \frac{n_2}{\lambda \beta_{TPA}}. \quad (2.45)$$

The FOM_{NL} describes the overall strength of the nonlinearity of a material. It tells us that a high nonlinear refractive index does not necessarily means high nonlinearity when the β_{TPA} is high. For silicon, β_{TPA} is quite large around telecommunication band, leading to a small FOM_{NL}. The nonlinear FOM of SCFs will be discussed in Chapter 4 with more details.

2.3.3 Nonlinear short pulse propagation

Nonlinear Schrodinger Equation

Short pulse propagation in a silica optical fibre can be well-described by the NLSE [70]:

$$i\frac{\partial A}{\partial z} + \frac{i\alpha}{2}A - \frac{\beta_2}{2}\frac{\partial^2 A}{\partial T^2} + \gamma|A|^2 A = 0. \quad (2.46)$$

Here γ is the nonlinear coefficient and is related to nonlinear refractive index and TPA coefficient as

$$\gamma = \frac{k_0 n_2}{A_{eff}} + \frac{i\beta_{TPA}}{2A_{eff}}. \quad (2.47)$$

To estimate the propagation length required to generate significant nonlinear effects, the nonlinear length of a fibre is defined as

$$L_{NL} = \frac{1}{\gamma P_0}. \quad (2.48)$$

Nonlinear effects become significant when the propagation length $L \gg L_{NL}$. This length is usually compared with the dispersion length which is defined as

$$L_D = \frac{T_0^2}{|\beta_2|}. \quad (2.49)$$

When $L_D \ll L_{NL}$, the pulse propagation is dominated by the GVD; when $L_D \gg L_{NL}$, the pulse propagation is dominated by nonlinear processes. When L_D and L_{NL} are comparable, the pulse broadening and nonlinear processes will act together.

For ultrashort pulse (femtosecond regime) propagation in the SCFs, a more complete model including the high order dispersion and TPA induced free carrier effect is used [81]:

$$\frac{\partial A}{\partial z} = \sum_{m\geq 2}^{\infty} \frac{i^{m+1}\beta_m \partial^m A}{m!\,\partial t^m} + i\gamma|A|^2 A - \frac{1}{2}(\alpha+\sigma)A. \quad (2.50)$$

The NLSE is usually solved numerically via the split-step Fourier method. The philosophy of this method is to divide the fibre into small segments and consider the dispersion, propagation loss and nonlinear effects separately. The equation is written in the form using operators $\widehat{D}$, $\widehat{N}$ and $\hat{L}$ as

$$\frac{\partial A(z,t)}{\partial z} = \left(\widehat{D} + \widehat{N} + \hat{L}\right)A(z,t), \quad (2.51)$$

where $\widehat{D}$, $\widehat{N}$ and $\hat{L}$ represent the dispersion, nonlinear effects and losses terms

$$\widehat{D} = \sum_{m\geq 2}^{\infty} \frac{i^{m+1}\beta_m \partial^m}{m!\,\partial t^m}, \quad (2.52)$$

$$\widehat{N} = i\left(k_0 n_2 + \frac{i\beta_{TPA}}{2}\right)\frac{|E|^2}{A_{eff}}, \quad (2.53)$$

$$\hat{L} = -\frac{\alpha_l}{2} - \frac{\sigma}{2}(1+i\mu)N_c. \quad (2.54)$$

By assuming the pulse propagates over a very small distance Δz each time, these effects can be calculated separately. Then pulse can be then estimated by

$$A(z+\Delta z\,,\mathrm{t}) \approx A(z\,,\mathrm{t})\mathrm{e}^{(\widehat{D}+\widehat{N}+\hat{L})\Delta z}. \quad (2.55)$$

Eq. (2.55) can be solved step by step numerically. The nonlinear step is solved in the time domain and the dispersion and loss step can be solved in the frequency domain, where the temporal derivatives $\frac{\partial^m}{\partial t^m}$ in Eq. (2.52) can be replaced by $(j\omega)^m$.

Pulse broadening by dispersion

When an ultrashort pulse propagates in a dispersive medium, the different wavelengths of the pulse travel at different speeds, so the pulse is stretched in the time domain. This broadening effect can be studied using the NLSE. By setting the nonlinear part and loss to zero, Eq. (2.46) can be written as [70]

$$i\frac{\partial A}{\partial z} - \frac{\beta_2}{2}\frac{\partial^2 A}{\partial T^2} = 0. \quad (2.56)$$

Then, it can be solved in the frequency domain to yield

$$A(z,\omega) = A(0,\omega)e^{\frac{i\beta_2}{2}\omega^2 z}. \quad (2.57)$$

As $|A(z,\omega)| = |A(0,\omega)|$, the spectrum of the pulse does not vary when it propagates. However, the phase of the pulse is a function of frequency and distance. The pulse envelop in time domain can be obtained by Eq. (2.57) using inverse Fourier transform

$$A(z,T) = \frac{1}{2\pi}\int A(z,\omega)e^{i\omega T}d\omega. \quad (2.58)$$

Self-phase modulation

SPM is a fundamental nonlinear phenomenon where the phase of an intense ultrashort short pulse is modulated by itself though the Kerr effect. To analyse SPM on pulse propagation, the NLSE can be simplified excluding the dispersion and loss terms as

$$\frac{\partial A}{\partial z} = i\gamma|A|^2 A. \quad (2.59)$$

It can be solved as

$$A(z,T) = A(0,T)(e^{i\varphi}e^{i\varphi_{NL}}), \quad (2.60)$$

where φ_{NL} is the nonlinear phase shift and is described as

$$\varphi_{NL}(z,t) = \frac{z}{L_{NL}}|A(0,t)|^2. \quad (2.61)$$

Eq. (2.61) shows that the nonlinear effects do not change the pulse envelope, they only modulate the temporal phase of the pulse. This phase shift not only depends on z, but also is affected by the intensity of the pulse. A time dependent pulse intensity can lead to a time dependent nonlinear phase change. Thus, new frequency components $\Delta\omega$ will be introduced by this phase shift. $\Delta\omega$ can be obtained by taking the derivative of nonlinear phase shift against time as

$$\Delta\omega(z,T) = -\frac{\partial\varphi_{NL}}{\partial T} = -\frac{z}{L_{NL}}\frac{\partial|A(0,T)|^2}{\partial T}. \quad (2.62)$$

This indicates that there will be a continuous phase shift accumulated along propagation, with new frequencies being constantly generated that are related to the initial pulse envelope.

Fig. 2.11 (a) shows the spectra evolution of a 1 ps hyperbolic secant pulse at λ = 1.55 μm, after propagation through a length of 10 L_N. New frequencies are generated at two sides of the central wavelength. Fig. 2.11 (b) shows the nonlinear phase shift and chirp of the pulse. At the rising edge

of the pulse, the chirp is negative, so the new frequencies generated are smaller, corresponding to longer wavelengths. At the trailing edge of the pulse, the chirp is positive, so the new frequencies generated are larger, corresponding to shorter wavelengths.

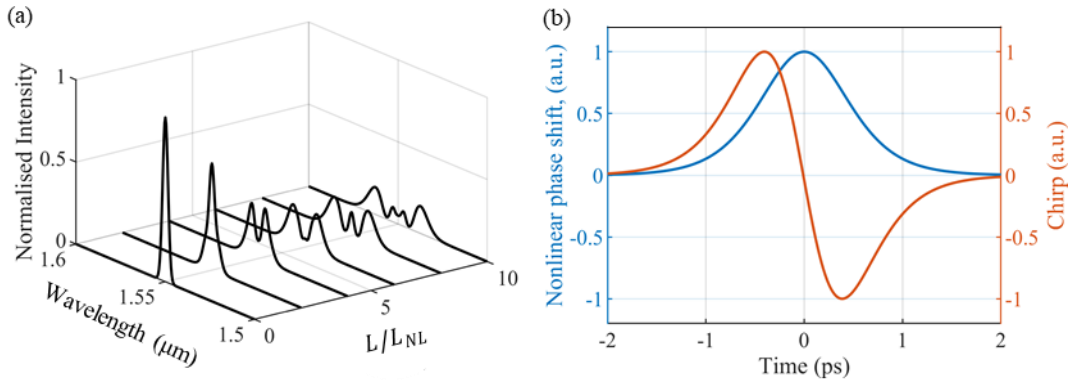

Figure 2.11 (a) Spectral evolution of SPM for a 1 ps Gaussian pulse at 1.55 μm propagating over the nonlinear length 10 L_N. (b) Nonlinear phase shift and chirp of the output pulse.

Soliton propagation

An optical soliton is an important kind of pulse in fibre optics. When the fibre dispersion is in the anomalous dispersion region with a positive nonlinear refractive index, the nonlinear and dispersion effects can cancel each other if the pulse power is exactly right. In this condition, the pulse remains undistorted in temporal shape and spectral profile over a long distance, and so is called a fundamental soliton. To form a fundamental soliton, the input pulse needs to satisfy

$$A(z=0,T)=\sqrt{P_0}sech\left(\frac{T}{T_0}\right), \tag{2.63}$$

$$N=\sqrt{\frac{L_D}{L_{NL}}}=\sqrt{\frac{\gamma P_0 T_0^2}{|\beta_2|}}=1, \tag{2.64}$$

where N is the soliton order.

Higher order solitons can exist for N > 1, but it must be an integer. For these pulses, the shape and spectrum periodically compress and broaden. The spatial period z_{sol} of a higher order soliton is related to the dispersion length as

$$z_{sol}=\frac{\pi}{2}L_D. \tag{2.65}$$

In practice, solitons can be perturbed by various factors, such as loss, high order dispersion and nonlinear effects. Particularly, for a femtosecond pulse, the soliton can be severely perturbed by the TOD when it plays a significant role. High order solitons can then be unstable and break up into

multiple constituent fundamental solitons. The distance before the breakup is called the fission length, which is related to the soliton order and nonlinear length as

$$L_{fiss} = NL_{NL}. \quad (2.66)$$

Dispersive wave emission

When a fibre is in the anomalous dispersion region at the operational wavelength and the initial pulse transmitted does not match the parameters with any orders of soliton, the energy will be transferred to dispersive wave (DW). It can also be triggered by disturbation during pulse propagation, such as higher order dispersion and sudden change in fibre dimension during propagation. The physical explanation of this phenomenon is called the Cherenkov radiation described in Ref. [83]. Here in this thesis, the focus is mainly on DW emission from the femtosecond soliton propagation, when the third order dispersion plays a significant role.

For DW formed by third order dispersion, the position of the DW depends on the phase matching condition in the fibre and can be estimated by [84]

$$\Delta v_d \approx \frac{3|\beta_2|}{2\pi\beta_3} + \frac{(2N+1)^2\beta_3}{6\pi|\beta_2|T_0^2}, \quad (2.67)$$

where Δv_d is the frequency shift of DW.

It can be also seen that the position of the DW also depends on the soliton number N, which is related to the fibre nonlinearity and pump power. Although N represents the soliton order number, it does not necessarily to be an integer here in this equation.

Chapter 3 Fabrication of tapered silicon core fibres

3.1 Introduction

This chapter introduces the fabrication method used to produce the tapered SCFs. First of all, it reviews the MCD technique used for fabricating the as-drawn fibre. Then, the tapering process for the SCFs is introduced in several parts. The first part talks about the hands-on experience of the tapering rig operation and two methods for mounting the SCFs. Then, the tapering process, including the fibre deformation in the hot region is studied both experimentally and numerically by a model based on the fluid dynamics theory. Some problems during the tapering process are discussed, such as fibre breakup and errors in the fibre profile. Then the fabrication of nanoscale core SCFs is discussed, with the main focus on controlling the quality of the core in the tapering process. Finally, the sample preparation technique to facilitate optical coupling is introduced.

3.2 Molten core drawing technique

The as-drawn SCFs used in this work were fabricated using the molten core drawing (MCD) technique by our collaborators from the Norwegian University of Science and Technology (NTNU) and Clemson University (CU). This technique has proven to be successful in producing large core SCFs in previous work [23]. Later, it was found that adding an additional calcium oxide interface layer between the fibre core and cladding can improve the mechanical properties of the fibres. Fibres without this interface layer usually exhibit large stress in the core, which can cause cracking during handling and even in the drawing process [54]. Fig. 3.1 shows the as-drawn SCF fabricated from the MCD method [63], [64].

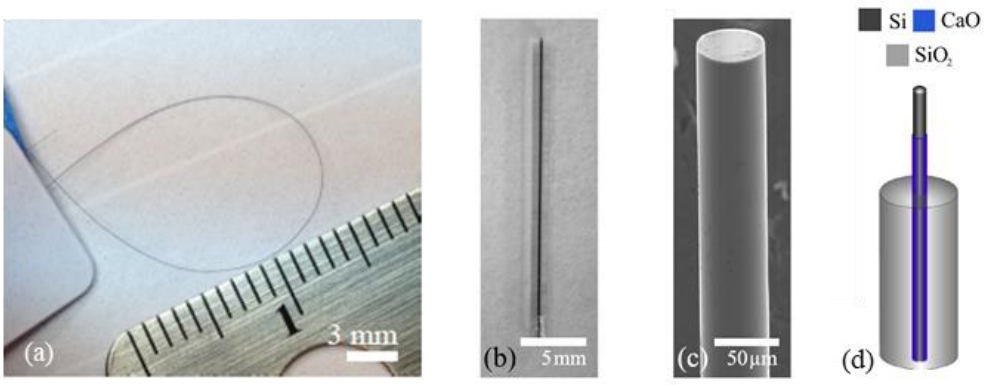

Figure 3.1 SCFs fabricated using the MCD technique. (a) Photo of a small core SCF [64], illustrating its flexibility. (b) Photo of a large core SCF that is more rigid [63]. (c) SEM

image of a SCF core with its silica cladding etched by hydrofluoric solution [63]. (d) Illustration of SCF structure with the interface modifier [63].

The fabrication procedure of as-drawn SCFs is described in [54], [63]. Firstly, high purity CaO powder (>99.9%) is mixed with deionised water to form lime solution (calcium hydroxide) in a beaker. Then, the solution is forced into a long silica tube using a vacuum pump, during which the calcium hydroxide solution attaches to the side wall of the tube. The tube is then dried overnight and one end is sealed with an oxy-acetylene torch. A silicon rod is inserted inside the tube and drawn into fibres in a drawing tower with 1950 °C, a pulling rate of 2.7 m/min and feeding rate of 3 mm/min [63]. This technique can produce meters of SCF with outer diameters larger than 150 µm and core diameters typically around 10 µm, or larger. Fig. 3.2 illustrates the fabrication process of the as-drawn fibre.

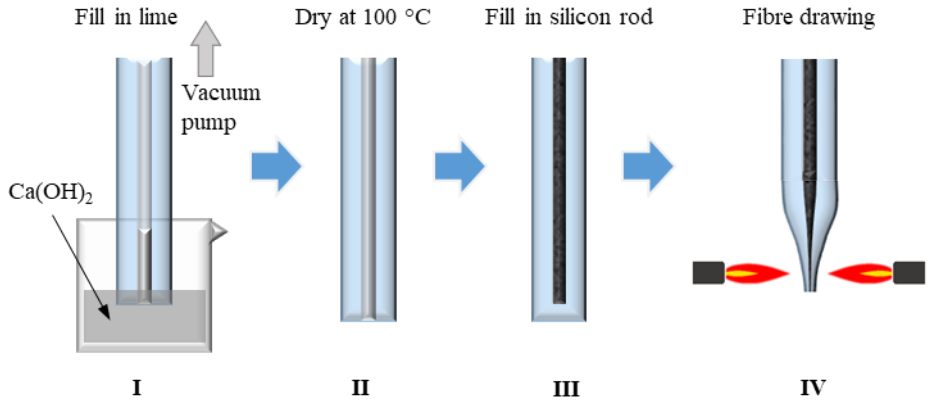

Figure 3.2 Fabrication process of MCD with CaO interface modifier.

The chemical composition distribution of the as-drawn fibre was characterised using a microprobe scan, as shown in Fig. 3.3 (a) and (b), taken from [54]. It shows that the CaO interface layer successfully blocks the oxide diffusion, as there is little oxide content in the core region. The thickness of the interface layer can be controlled by the fabrication process described in Fig. 3.2. Fig. 3.3 (c) shows a microscope image (backlight configuration) of one of the as-drawn SCFs used in this work. The interface layer can be distinguished as the thin circle between the core (dark region) and the cladding (bright region). The interface layer is estimated to be around 1 µm in this fibre. The refractive index of calcium oxide is estimated to be ~1.8 in the near infrared [85]. It is slightly higher than silica but much lower than silicon. For a SCF with a core diameter of a few micron, the thickness of its interface layer will be a few hundred nanometres in scale. Numerical simulations have shown that the thin (nanometre scale) CaO layer has a negligible effect on the fibre modal behaviour and dispersion.

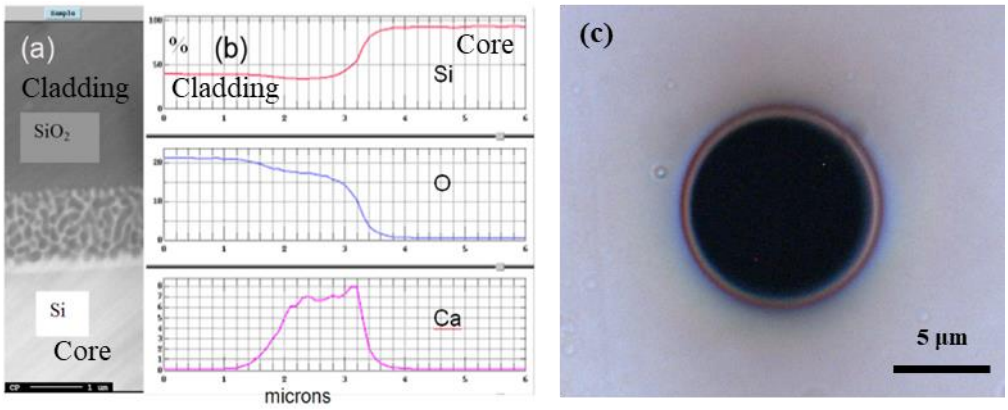

Figure 3.3 (a) SEM image at core/cladding interface of the as-drawn SCF [54]. (b) Microprobe data of the cladding core interface. (c) Microscope image of silicon core (backlight illumination).

3.3 Tapering technique of SCF

Fibre tapering has been a widely used post-processing technique for many years. It is principally used as a means to modify the dimensions of the fibre in order to change its optical properties such as dispersion, nonlinearity and modal behaviour. It follows a similar process to conventional fibre drawing, where a fibre is softened in a hot zone and stretched to obtain smaller dimensions. The hot zone can be induced by a flame [86], laser heating [87], [88] or an electrical powered graphite filament [89].

The tapering technique used in this work is modified from a popular tapering scheme that is called flame brushing technique. The flame brushing technique uses a movable hydrogen gas torch as the heating unit. The fibre is fixed by two stages, with the tapered region heated by the flame of the torch. The two stages pull the fibre slowly in opposite directions as the flame swings back and forth to spread the heat evenly in the fibre. The taper shape can be controlled by the flame temperature and motion, including speed, start and end position, and the number of times the flame moves back and forth. The drawback of this technique is that the heating process could introduce contaminants to the fibre. Furthermore, the flame has a non-uniform heating profile and its temperature cannot be controlled precisely.

3.3.1 Vytran glass processor

In this work, a Vytran GPX-3300 glass processor is used for tapering the SCFs. It uses a modified tapering scheme that is very similar to the flame brushing technique. The hot zone is induced by a graphite filament which provides a more accurate, stable and uniform temperature profile with a wide tuneable range. Thus, it does not require the multiple back and forth movement of the hot zone and instead the whole tapering process is completed in a single sweep. As shown in Fig. 3.4,

the machine consists of three parts: the left stage, the right stage and the splice head. The filament is in a fixed position during tapering. The left stage is used as the drawing stage and the right stage is used as feeding stage. These stages can move forward, backwards, as well as rotate and translate for various purposes. The minimum step of the stages for moving forward and backwards is 1 µm. The fibre is heated in an Ω shaped graphite filament, which is powered electrically. The filament is protected from being oxidised in the air by a flow of argon gas. The mirror stage and microscope are used to monitor the fibre alignment from different angles. Mirror *a* and *b* shown in the diagram are used to monitor the cross-sectional view of the fibre facet. Mirror *c* and *d* are used to monitor the fibre from side for alignment. There are two tension monitors installed on the two stages to monitor the overall tension along the fibre in the drawing process.

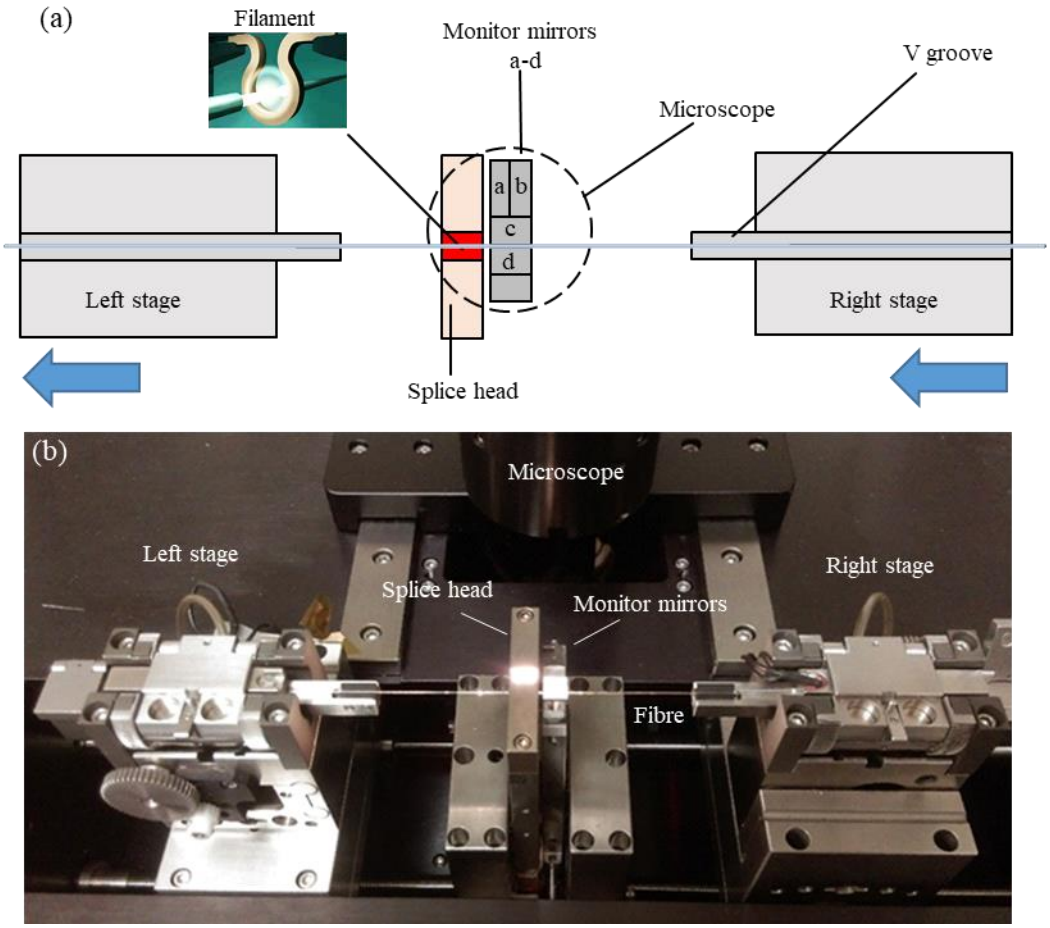

Figure 3.4 (a) Diagram of Vytran GPX-3300 glass processor. (b) Photo of Vytran is tapering a fibre.

The tapering parameters that can be controlled via this machine are shown in Table. 3. These parameters need to be set properly to obtain an accurate taper profile. The filament power is the power applied to the graphite filament. Its value depends on the size of the fibre cross section area and the filament type used. For the filament (FTAV4) used in this work, the value is between 30 W to 100 W for processing various fibre dimensions. However, one drawback of the graphite filament is that its heating performance changes over time, proportional to its use. To maintain the

repeatability of the tapering process, the filament needs to be calibrated periodically. The filament delta is used for controlling the power variation of the filament during the tapering process. As the waist region is much smaller than the other regions, it requires smaller amount of heat to soften, thus, a negative delta value is used to lower the power when tapering the fibre waist region. The pull velocity is the drawing speed of the left stage during tapering. In this work, I established that the best drawing speed for tapering SCFs is 1 mm/s. The machine becomes unstable when using speeds beyond this point due to some mechanical issues. The gas flow rate is the argon flow rate, used for filament protection.

Table 3 The tapering parameters for the Vytran GPX-3300

Taper dimensions [mm]	**Dimension of the target taper.**
Filament power [W]	The electrical power of the filament.
Filament delta [%]	Power variation in the taper waist region.
Pull velocity [mm/s]	The drawing speed.
Taper pull delay [s]	The heating time before fibre drawing.
Gas flow rate [l/min]	Argon gas flow rate during tapering.

3.3.2 Tapering SCF with mechanical support

Capillary method

The SCFs need to be long enough (> ~20 cm) to be mounted on the tapering rig. After each taper process, only the tapered section in the middle of the SCF is useful. The remaining parts of the SCF will be removed and disposed of as they do not have enough length to be mounted back on the tapering rig. The amount of fibre we can access is limited by what our collaborators can supply. To save material, the SCFs can be cut into small pieces in lengths of around 5 mm and inserted into a hollow core silica tube before tapering, as described in Ref. [24]. The SCF is manually cleaned by acetone with lens tissue and inserted in the opening of the tube and pushed into the middle of the tube using a bare single mode fibre (Corning SMF-28). The silica tube acts as a mechanical support for the SCF and an extension of the fibre length for mounting. The silica tube used in this work has a 150 µm inner diameter and 200 µm outer diameter, as shown in Fig. 3.5 (a). The inner diameter of the tube needs to be a few tens of micrometres larger than the SCF cladding, otherwise the fibre insertion can be very difficult, as the SCF can easily get stuck due to small glass fragments inside the tube. Some of this gap can still exist in the fibre after tapering, but it has a negligible effect on the tapering process as there is always part of the sidewall of the SCF and silica tube that are fused together at the drawing temperature. However, it can make the tapering ratio unpredictable and make fibre cleaving difficult.

The tube can be fused with the SCF cladding completely if the starting position of the tapering is set to be a few millimetres before the starting position of the SCF. In this way, the silica tube is initially tapered down to a slightly smaller inner diameter, which can fuse with the SCF more easily. The fusion process is shown in Fig. 3.5 (b) and (c), where the SCF is squeezed by the tapered silica tube. When the SCF surface is properly cleaned before inserting into the silica tube, the fusion interface can have a good quality such that the silica tube is no longer distinguishable from the SCF. Using this method, the as-drawn SCF lengths are used to their maximum, without waste of material, i.e., a tapered fibre device will only cost a few millimeters of as-drawn fibre. This method can also be used to modify the core/cladding ratio by repeatedly cladding the SCF with silica tubing, which can be very useful in the SCF integration. This will be discussed further in Chapter 6.

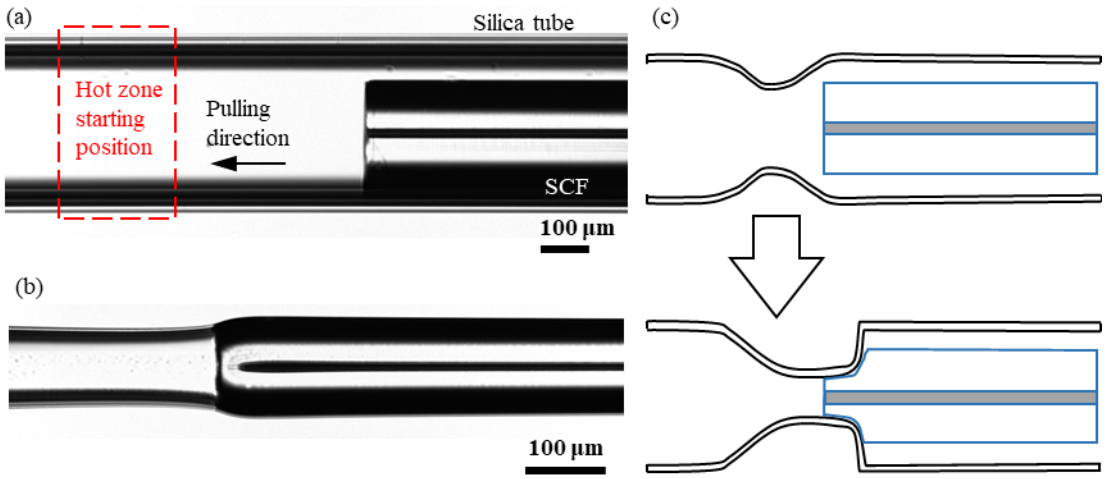

Figure 3.5 (a) Microscope (Vytran) image showing a SCF inside of a silica tube. The red dashed line shows the starting position of the filament to obtain complete fusion. (b) Microscope (Vytran) image showing perfect fusion of the tube and SCF in (a). (c) Schematic of perfect fusion between the silica tube and a SCF.

SMF splicing method

Although using silica tubing as a mechanical support can greatly save the material, the sample preparation can be time consuming. Also, dust and perspiration attaches to the SCF surface during handling, which can affect the tapering quality. Thus the SCF requires careful cleaning before it is inserted into the glass tubing, which increases the complexity of the process. Another method is to splice one side of the SCF to a SMF-28 as a means to extend its length for mounting. The silica fibre acts as the mechanical support similar to that of silica tube. The splicing process can be achieved using in the same Vytran tapering rig. Fig. 3.6 shows an SMF-28 at the left side of the image and the SCF on the right side. Using a standard splicing process, the cladding of the two fibres can be fused together easily. The core of the SCF melts and forms silicon spheres as shown in the Fig. 3.6 (b).

However, this is not a problem as this splicing is only used for connecting the SCF and SMF-28 mechanically and not for light coupling.

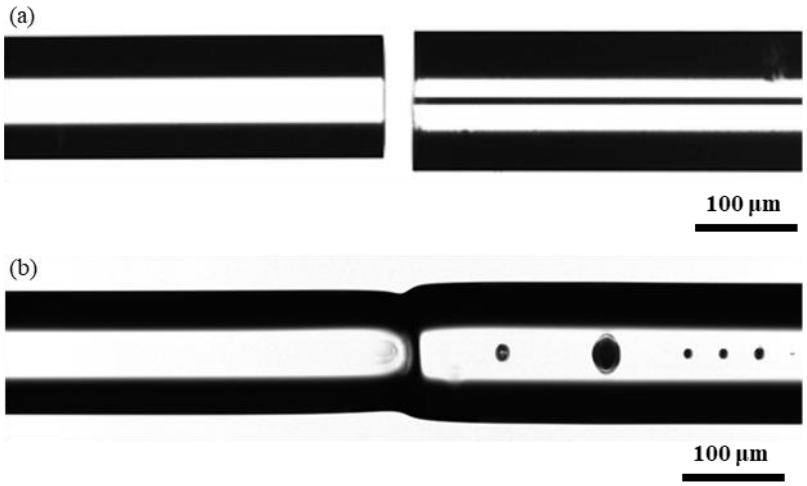

Figure 3.6 Splicing SMF to SCF as mechanical support before tapering. Image taken from Vytran microscope.

3.3.3 Profile of tapered SCF

Using these tapering methods, a number of tapered SCFs were fabricated to test the performance of the tapering system. At the beginning, the main task is to find proper tapering parameters. For various cases, the fibre broke during the tapering process, as the filament power was not enough to soften the fibre. When the power is high enough, the SCF can be successfully tapered with a smooth profile. Fig. 3.7 shows a fibre profile measured from a tapered SCF. The down transition, waist and up transition lengths were set to be 10 mm, 10 mm and 10 mm with a taper ratio of 0.2. The resulting down transition is slightly longer than 10 mm and the up transition is slightly shorter than 10 mm. Further improvement of the profile accuracy can be achieved by the trial and error method.

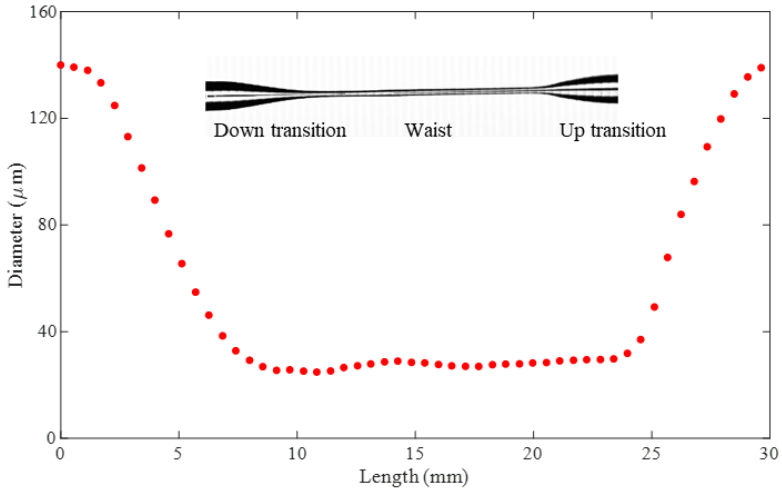

Figure 3.7. Measured fibre profile of a tapered SCF. Inset is a microscope image of the SCF.

Numerical model for tapering

To further investigate the profile of the tapered SCF and the tapering process, a model was built to simulate the tapering process numerically. The tapering process is described in Fig. 3.8. The tapering rig consists of three stages: a pulling stage, a feeding stage and a hot zone. The feeding stage slowly feeds the untapered fibre into the hot zone with the feeding speed $\tilde{v}_f$. The pulling stage draws the fibre, with a faster speed $\tilde{v}_d$. The hot zone has a length of L_{hz}, which is typically a few millimetres. The untapered fibre has a diameter of D_0 and the target taper waist diameter is D_w.

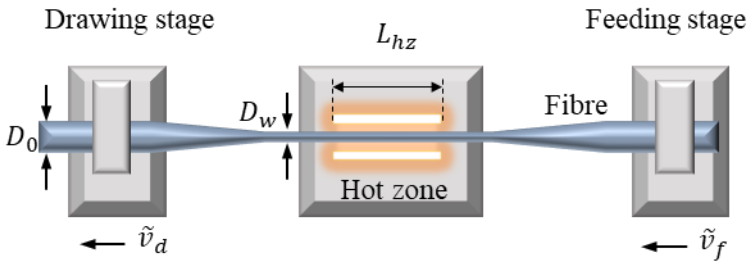

Figure 3.8 Diagram of single sweep tapering process.

In the drawing process, the hot zone temperature rises above the softening point of the fibre material (fused silica), which allows the fibre to deform. The fibre satisfies mass conservation, which leads to the relation between fibre dimension and tapering speed as [90]

$$\frac{D_w(t)}{D_0} = \sqrt{s(t)}, \tag{3.1}$$

$$s(t) = \frac{\tilde{v}_f(t)}{\tilde{v}_d(t)}. \tag{3.2}$$

Then Eqs. (3.1) and (3.2) can be represented in the spatial domain using drawing length z as

$$z = \int_0^t \tilde{v}_d(\tau)d\tau, \tag{3.3}$$

$$\frac{D_w(z)}{D_0} = \sqrt{s(z)}, \tag{3.4}$$

$$s(z) = \frac{\tilde{v}_f(z)}{\tilde{v}_d(z)}. \tag{3.5}$$

Eqs. (3.4) and (3.5) indicate that the tapered profile can be designed by controlling the speed ratio of the two stages. However, the non-negligible length of the hot zone makes the tapering process

more complicated, as the deformation of the softened glass is a gradual process that is affected by the material viscosity [90]. To have a better understanding of the fibre tapering process, we refer to the model described in Ref. [91]. In this model, the fibre deformation is described by the equations:

$$\frac{\partial}{\partial z}(3\tilde{\mu}\tilde{A}\frac{\partial \tilde{v}}{\partial z}) = 0, \quad (3.6)$$

$$\frac{\partial \tilde{A}}{\partial t} + \frac{\partial}{\partial z}(\tilde{v}\tilde{A}) = 0, \quad (3.7)$$

$$\tilde{F} = 3\tilde{\mu}\tilde{A}\frac{\partial \tilde{v}}{\partial z}, \quad (3.8)$$

with the boundary conditions [90]

$$\tilde{v}|_{z=0} = \frac{\tilde{v}_d - \tilde{v}_f}{2}, \quad (3.9)$$

$$\tilde{v}|_{z=l} = -\frac{\tilde{v}_d - \tilde{v}_f}{2}, \quad (3.10)$$

$$\tilde{A}\big|_{t=0} = \tilde{A}_0, \quad (3.11)$$

where $\tilde{\mu}$ is the viscosity distribution of the silica cladding along the fibre axis, $\tilde{A}$ is the cross-sectional area of the fibre cladding, $\tilde{v}$ is the axial velocity distribution of the fibre, $\tilde{F}$ is the force distribution along the fibre. These parameters are two-dimensional variables that are dependent on the z and t. Eqs. (3.6) - (3.11) can be solved numerically by the finite difference method. To solve this model numerically, Eqs. (3.6) and (3.7) can be rewritten in their expanded form as:

$$\frac{\partial \tilde{v}}{\partial z}(\tilde{A}\frac{\partial \tilde{\mu}}{\partial z} + \tilde{\mu}\frac{\partial \tilde{A}}{\partial z}) + \tilde{\mu}\tilde{A}\frac{\partial^2 \tilde{v}}{\partial z^2} = 0, \quad (3.12)$$

$$\frac{\partial \tilde{A}}{\partial t} + \tilde{A}\frac{\partial \tilde{v}}{\partial z} + \tilde{v}\frac{\partial \tilde{A}}{\partial z} = 0. \quad (3.13)$$

Writing them in the finite difference form, using the centred differentiation formulas yield:

$$\frac{\tilde{v}_{i+1} - \tilde{v}_{i-1}}{2\Delta z}(\tilde{A}_i\frac{\tilde{\mu}_{i+1} - \tilde{\mu}_{i-1}}{2\Delta z} + \tilde{\mu}_i\frac{\tilde{A}_{i+1} - \tilde{A}_{i-1}}{2\Delta z}) + \tilde{\mu}_i\tilde{A}_i\frac{\tilde{v}_{i+1} - 2\tilde{v}_i + \tilde{v}_{i-1}}{\Delta z^2} = 0, \quad (3.14)$$

$$\frac{\tilde{A}_{i+1} - \tilde{A}_{i-1}}{2\Delta t} + (\tilde{A}_i\frac{\tilde{v}_{i+1} - \tilde{v}_{i-1}}{2\Delta z} + \tilde{v}_i\frac{\tilde{A}_{i+1} - \tilde{A}_{i-1}}{2\Delta z}) = 0. \quad (3.15)$$

Eq. (3.14) can then be written in the form as

$$X\tilde{v}_{i-1}+Y\tilde{v}_i + Z\tilde{v}_{i+1} = 0, \qquad (3.16)$$

where X, Y, Z are coefficients that are functions of $\tilde{A}$ and $\tilde{\mu}$, derived from Eq. (3.14). Thus, Eq. (3.16) can be described in a matrix as below:

$$\begin{bmatrix} X_1 & Y_1 & Z_1 & 0 & \dots & 0 & 0 & 0 \\ 0 & X_2 & Y_2 & Z_2 & \dots & 0 & 0 & 0 \\ 0 & 0 & X_3 & Y_3 & \cdots & 0 & 0 & 0 \\ \vdots & \vdots & \vdots & \vdots & \ddots & \vdots & \vdots & \vdots \\ 0 & 0 & 0 & 0 & \cdots & Z_{N-2} & 0 & 0 \\ 0 & 0 & 0 & 0 & \cdots & Y_{N-1} & Z_{N-1} & 0 \\ 0 & 0 & 0 & 0 & \cdots & X_N & Y_N & Z_N \end{bmatrix} \begin{bmatrix} \tilde{v}_0 \\ \tilde{v}_1 \\ \tilde{v}_2 \\ \vdots \\ \tilde{v}_{N-3} \\ \tilde{v}_{N-2} \\ \tilde{v}_{N-1} \end{bmatrix} = \begin{bmatrix} 0 \\ 0 \\ 0 \\ \vdots \\ 0 \\ 0 \\ 0 \end{bmatrix}. \qquad (3.17)$$

From Eqs. (3.9) and (3.10), $\tilde{v}_0$ and $\tilde{v}_{N-1}$ are known boundary conditions, which can be substituted into Eq. (3.17). $\tilde{v}_i$ is then solved for numerically using Matlab. The fibre cross section can be updated for small units of time using Eq. (3.15), as illustrate in Fig. 3.9. $\tilde{v}_i$ and $\tilde{A}_i$ are then repeatedly calculated until the final fibre profile is obtained. In this process, the relative position between the viscosity distribution $\tilde{\mu}$ and the fibre profile needs to be updated with a relative speed of $\tilde{v}_\mu = (\tilde{v}_d + \tilde{v}_f)/2$. The viscosity distribution $\tilde{\mu}$ is assumed to have a super Gaussian as:

$$\tilde{\mu}(z) = \tilde{\mu}_{max} - (\tilde{\mu}_{max} - \tilde{\mu}_{min})\left(e^{-2\left(\frac{z}{L_{hz}/2}\right)^m}\right), \qquad (3.18)$$

where $\tilde{\mu}_{min}$, $\tilde{\mu}_{max}$ are the minimum and maximum viscosity of the fibre during tapering, as shown in Fig. 3.9 (b), and m is the super Gaussian power. This model is verified by comparing the numerical results of the fibre tapering process described in [90]. Same taper profile is obtained which indicates the effectiveness of this model.

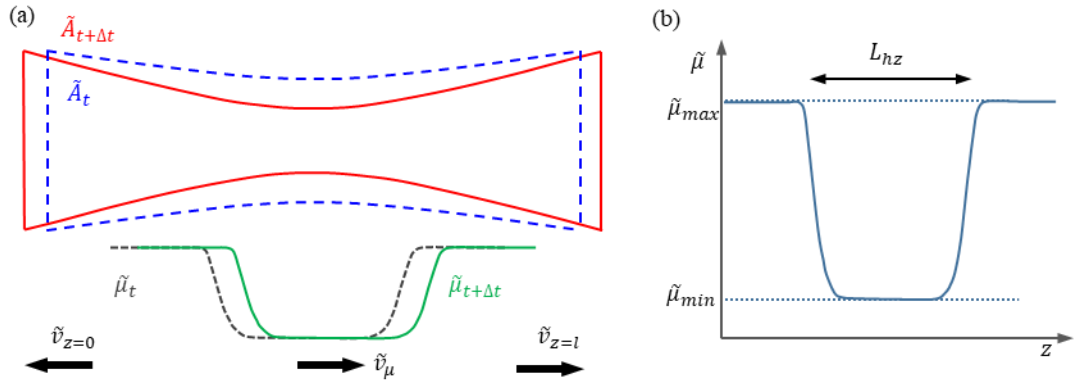

Figure 3.9 (a) Schematic of model used for numerical modelling of the tapering process. The blue and red lines show the small profile change before and after pulling in a small amount of time. The grey and green lines show the changes in the viscosity distribution. (b) Viscosity distribution of a fibre during tapering process.

Profile of tapered fibre

The numerical model is used for investigating the profile of the tapered fibres. The simplest example is when the designed taper profile is a step function, that is, the drawing speed and feeding speed are fixed throughout the tapering process. Fig. 3.10 shows the tapering profile evolution as a function of time. The drawing speed is set to be 1 mm/s with a feeding speed of 0.25 mm/s, which corresponds to a taper ratio of 0.5 according to Eqs. (3.4) and (3.5). The viscosity distribution is assumed to be a super Gaussian distribution with power m = 5 and L_{hz} = 1 mm. $\tilde{\mu}_{max}$ and $\tilde{\mu}_{min}$ are assumed to be 10^4 Pa·s and 10^2 Pa·s, as described in Ref. [92]. It takes around 1 s for the fibre to reach the waist diameter, shown in the Fig. 3.10 (a). There is a small overshoot at the end of the initial transition region, before the fibre waist diameter gradually stabilizes. The overshoot is independent of the initial fibre diameter, instead it depends on the taper ratio and hot zone length [90]. Larger tapering ratios will result in larger overshoots at the transition region. When the taper ratio is fixed, the overshoot can be reduced by shortening the length of the hot zone or increasing the length of the down transition. When a long down transition region is applied, the overshoot is not as significant. As shown in Fig. 3.10 (b), when the down transition is set to be 3 mm, the overshoot at the end of the down transition is greatly reduced. The up transition of the fibre does not suffer an overshoot problem, as shown in Fig. 3.10 (a) and (b). Therefore, in practice the taper profile is more or less asymmetric, even if the down and up transition are designed to have the same length, especially when the transition region is short. When the down and up transition are set to be the same length, the actual fabricated down transition length is usually slightly longer than the up transition. These characteristics need to be considered when designing the tapered profile to obtain more accurate shapes.

In the case of tapering the SCFs, as the silicon core is small compared to the silica cladding, the process can be approximately treated as tapering a silica fibre. The transition is usually set to be a few millimetres or longer to minimise overshoot of the fibre profile. By carefully designing the taper profile and correctly setting the tapering parameters, the overshoot of the waist diameter can be controlled within the order of ±5%.

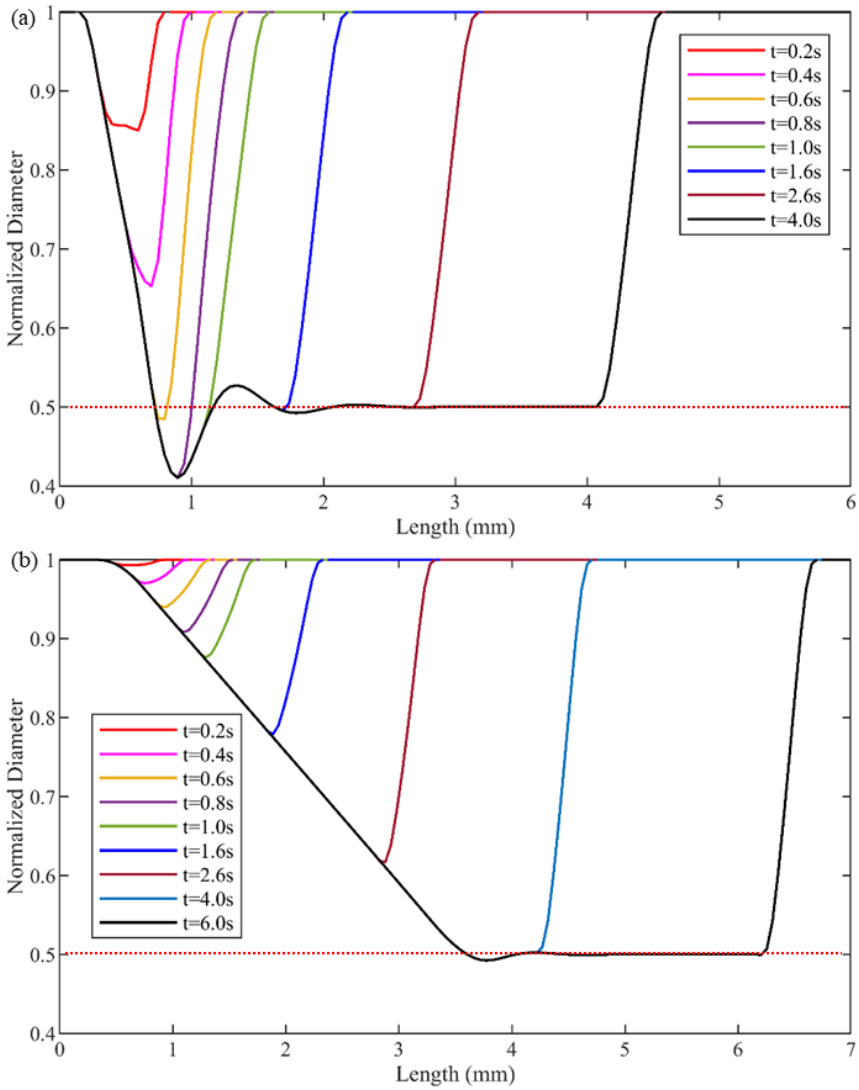

Figure 3.10 Simulated taper profile evolution (y axis is normalised outer diameter of the fibre). (a) Fixed tapering ratio of 0.5 with 0 mm target down transition length. (b) Fixed tapering ratio of 0.5 with a 3 mm down transition length. The dotted line is to guide the eye to the designed fibre waist diameter.

3.3.4 Fabrication of silicon nanowire

For nonlinear photonics applications, efficient frequency conversion in the SCFs requires not only a high light intensity, but also a proper dispersion to meet the phase matching conditions. As the dispersion of the SCFs is dependent on the operating wavelength and fibre geometry, in some cases, the SCFs need to be fabricated smaller than 1 µm to obtain a desired dispersion profile. The fabrication process is slightly different when tapering nanoscale SCFs.

As silicon has a lower melting temperature than silica, when tapering a SCF the silicon core is in a molten state, thus, it typically follows the same shape as the inside wall of the cladding. This is true for fibre cores that are larger than a few micrometres in diameter. However, when the targeted core dimension reaches sub-micron sizes, the core can easily breakup. Fig. 3.11 shows a comparison

between a continuous core SCF and a SCF that has undergone core breakup. This is expected to happen as it has been found that, for crystalline materials such as semiconductors, there exists a fundamental size limit of the core diameter that can be drawn [93]. Below this limit the core will become extremely unstable and easily breakup due to the Plateau–Rayleigh instability.

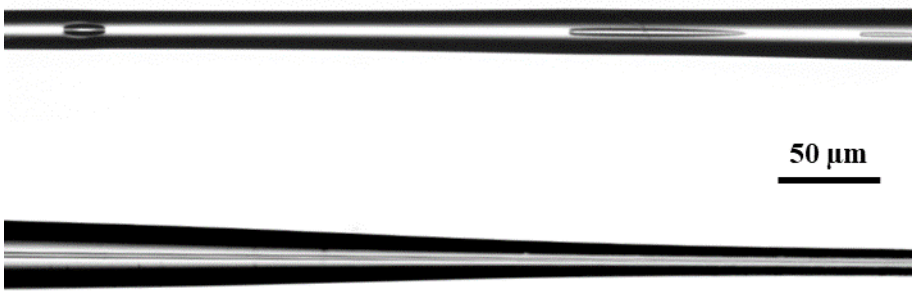

Figure 3.11 Microscope image showing SCF with core breakup (top) and SCF with continuous core (bottom).

Capillary number

Although the physical force that causes this breakup is still unknown, a simple model has been suggested to study this effect by calculating the capillary number C_a of the fibre [93]. The capillary number for a molten core fibre is defined as the ratio between the viscous stress in the cladding $\tilde{F}/D_0$ and the Laplace pressure due to the interfacial tension of the core $\tilde{\gamma}/D_{cw}$ as

$$C_a = \frac{\tilde{F} D_{cw}}{\tilde{\gamma} D_0}, \qquad (3.19)$$

where D_0 is initial fibre outer diameter, D_{cw} is the diameter of the fibre core at the waist region, $\tilde{F}$ is the drawing force and $\tilde{\gamma}$ is the interfacial tension (also known as the surface tension) of the core. The interfacial tension leads to the core breakup and the viscous stress prevents the core breakup. When $C_a > 1$, the viscous stress dominates so the core is more likely to be continuous, and when $C_a < 1$, the interfacial tension dominates so the core is more likely to breakup. C_a needs to be large enough to maintain a continuous core when tapering a SCF to nanoscale core dimensions.

When a SCF with an initial cladding/core diameter D_0/D_{c0} is tapered down to D_w/D_{cw} at the waist region, Eq. (3.19) can be rewritten with Eq. (3.8) as

$$C_a = \frac{(3\tilde{\mu}\tilde{A}\frac{\partial \tilde{v}}{\partial z})D_{cw}}{\tilde{\gamma} D_0} = \frac{3\tilde{\mu}\pi D_w^2 D_{cw}\frac{\partial \tilde{v}}{\partial z}}{4\tilde{\gamma} D_0} = \frac{3\pi\tilde{\mu}}{4\tilde{\gamma}} \cdot \frac{D_{cw}^3}{D_{c0}} \cdot \frac{\partial \tilde{v}}{\partial z}. \qquad (3.20)$$

Therefore, when the target D_{cw} is fixed, C_a can be increased by increasing $\partial\tilde{v}/\partial z$, which is proportional to the drawing speed. The term $\tilde{\mu}/\tilde{\gamma}$ is the ratio between the viscosity of silica and surface tension of the silicon. This ratio is inversely proportional to the temperature [92], [94],

which means that lower heating temperatures leads to a smaller C_a. In summary, to successfully taper a SCF down to nanoscale core dimensions, some tips are listed below:

1. Keep the drawing temperature low.
2. Use a fibre with a small initial core diameter (This can be achieved by pre-tapering of the fibre).
3. The drawing speed needs to be fast.

Optimisation of hot zone temperature

To find the lowest temperature suitable for fibre tapering, the tension along the fibre is monitored by a built-in force gauge in the tapering rig during the drawing process. The tension along the fibre changes with time as the tapering process proceeds. Fig. 3.12 shows an example of a typical tension evolution curve measured during a tapering process. As shown in this plot, before tapering the fibre is strained with a small initial tension of 8 gram-force (gf) to counteract the effect of gravity. At the beginning of the tapering process, position *a*, the filament heats the fibre for a short while before drawing, causing the tension to drop slightly to position *b*. Then the drawing begins and the fibre starts to deform. The down transition, waist and up transition region corresponds to *b*-*c*, *c*-*d* and *d*-*e*, respectively. The two peaks between *b*-*c* and *d*-*e* are caused by the speeding up and speeding down of the feeding stage. After the tapering process, there still remains a small tension on the fibre due to thermal contraction. When the filament temperature is low, the overshoot region between the down transition and waist region has the smallest cladding diameter where the fibre is most likely to break.

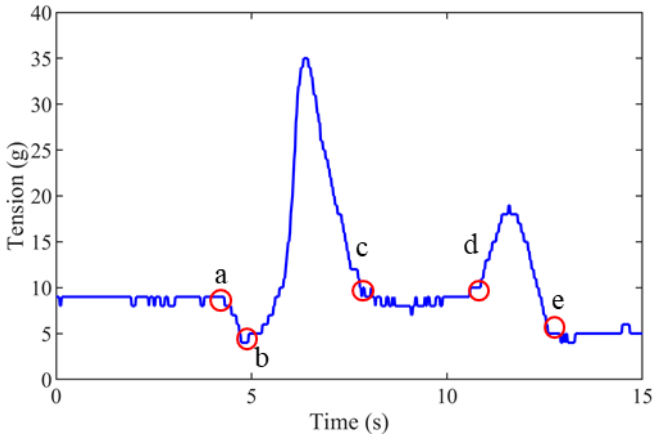

Figure 3.12 A typical tension curve for a SCF during the tapering process.

To avoid the fibre breaking, some tips to choose the best target parameters are listed below for reference. These tips are mostly based on hands on experience.

1. Decreasing the up/down transition length can reduce the overall tension during the tapering.

2. Longer sections of the waist region can withstand larger tensions due to the elasticity of the fibre.
3. Increasing the initial heating duration before pulling can decrease the overall tension along tapering.

3.4 Sample polishing and mounting

As the tapered SCF usually has a cladding diameter of a few micron to a few tens of micron in diameter over length of a few centimeters, it is difficult to cleave both ends of such a small fibre with available laboratory facilities. As a result, the fibre is placed inside a thick polymer capillary with adhesive wax, which provides mechanical support and allows for facet polishing. The tapered region of the SCF is manually cut and put into a capillary tube with a similar length, as shown in Fig. 3.13 (d). The gap between the capillary and the fibre is filled with wax adhesives (Crystalbond 509, Agar Scientific Ltd) using a hotplate to help the wax flow. The polymer adhesive used in this work has a flow point of 121 °C that will melt completely on the hot plate into a liquid form. After the tube is filled completely, it is taken off from the hotplate to cool down. The polymer tube is then cleaned using acetone to remove the wax around its surface. Finally, it is mounted on a sample holder and a standard polishing process is applied using optical polishing films. The polishing process has three steps, each step uses a polishing film with a reduced surface roughness. The final polishing film has particle sizes of 20 - 50 nm. The polished sample has a clean and smooth surface as shown in Fig. 3.13 (a) and (b).

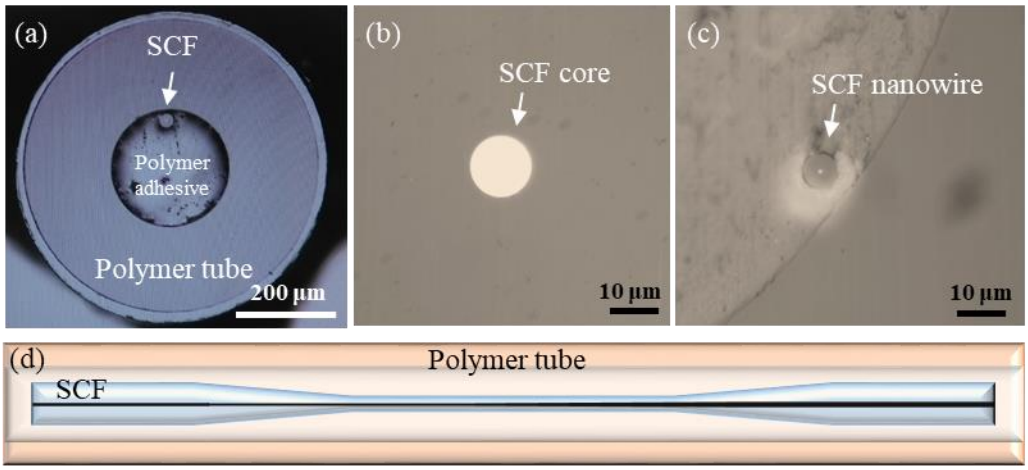

Figure 3.13 (a) Microscope image of a SCF sample in cross section view. (b) Microscope image of a large core SCF after polishing. (c) Microscope image of a SCF with a nanoscale core. (d) Illustration of the SCF sample preparation before polishing.

However, there are some disadvantages of this sample preparation scheme. As the adhesive wax has a flow point of 121 °C, it can easily melt when the fibre is pumped with a high average power laser. The threshold of the melting is related to the average pump power, coupling efficiency at the

front fibre facet and also the pumping wavelength, as the polymer absorption is wavelength dependent. In this work, the highest average power applied on a SCF sample is ~600 mW when using this preparation scheme. When the wax melts, it will flow out of the polymer tube and block the fibre facet. This can badly damage the input facet and decrease the coupling efficiency.

To overcome this problem for higher power operation, the preparation scheme is modified, as shown in Fig. 3.14. First of all, the input side of the fibre facet is polished, then the sample is placed on the hot plate again to melt the adhesive inside. The input side of the SCF in the tube is pushed out for ~1 mm from the polymer tube using a silica fibre inserted from the other side. Finally, the output end of the facet is polished. In this way, the fibre input facet has some distance from the wax and will no longer be affected by high input powers.

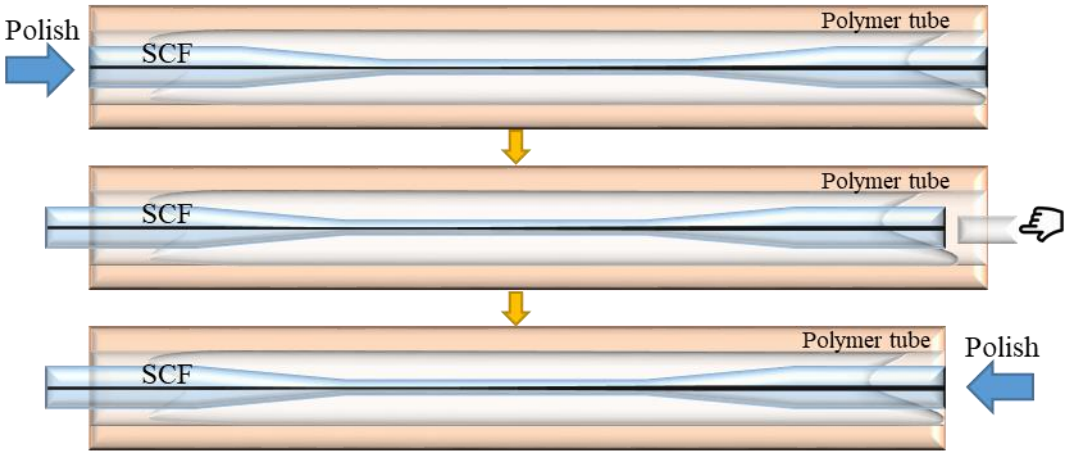

Figure 3.14 Sample preparation of SCFs for high-power applications.

3.5 Conclusion

This chapter has presented a detailed study of the tapering process for SCFs, including the tapering rig operation, profiles of the tapered fibres, silicon nanowire fabrication, and SCF sample preparation for optical characterisation. The fabrication technique of the as-drawn fibres using the MCD method is reviewed. A numerical model of the fibre drawing has been provided, which can be used for studying SCF tapering, but also for general fibre tapering and fibre drawing. The technique of fabricating of silicon nanowires is studied qualitatively. Information has also been given based on hands-on experience of SCF processing, which can be useful for increasing the quality of tapered SCFs and may be used as reference for other semiconductor core fibre fabrication and processing.

Chapter 4 Characterisation of silicon core fibres

4.1 Introduction

In this chapter, characterisation of the SCFs is introduced in three sections. To begin with, the material crystallinity of the tapered SCF is introduced. Two crystallinity characterisation methods, Raman spectroscopy and X-Ray diffraction (XRD) are reviewed. Then, the linear transmission losses of the various tapered SCFs are characterised via the cutback method and the Fabry–Pérot method extending over the telecommunication band to the mid-IR region. The results show that the micron-sized core tapered SCFs exhibit low linear losses on the order of a few dB/cm in the infrared region. In the third section, the nonlinear transmission properties, including the TPA coefficients and nonlinear Kerr indices are characterised from 1.54 to 2.35 μm. The wavelength dispersion of the TPA coefficients and nonlinear Kerr indices, obtained by fitting the experimental data with numerical simulations, are determined, and then used to calculate the nonlinear figure of merit (FOM_{NL}) of the tapered SCFs. These results are a guideline for identifying nonlinear applications for the SCFs in the mid-IR regime.

4.2 Crystallinity of tapered silicon core fibres

This section focuses on the material crystallinity of the SCF cores. There are three common types of allotropes of silicon: amorphous silicon (a-Si), crystalline silicon (c-Si) and polycrystalline silicon (p-Si). As shown in Fig. 4.1, for a-Si, the atoms are in a short range order, for c-Si, the atoms are arranged orderly and p-Si exhibits an intermediate state between c-Si and a-Si, which is a mixture of small crystal grains in random order. The core of the as-drawn fibres are in p-Si form, with the crystal grains in various orientations [54]. The size of the crystal grains depends on the drawing condition and fibre dimensions [95]. The optical transmission depends on the degree of crystallinity. Large gain sizes mean that less scattering loss is introduced from the grain boundaries. The optical transmission losses of these as-drawn fibres are usually high, typically larger than 10 dB/cm. This can be caused by the fabrication condition of the drawing process, such as relatively large hot zone, high drawing speed (typically in metres per minute) and large preform diameters (usually in millimetres). As silicon melts at 1414 °C [96], which is lower than the softening temperature of high purity fused silica (1675-1800 °C [97]), the core of the SCF is recrystallised during the tapering process. Although the tapering process is fundamentally the same process as drawing, the crystallinity of the core could be very different to that of the as-drawn fibres as the cooling dynamics are different.

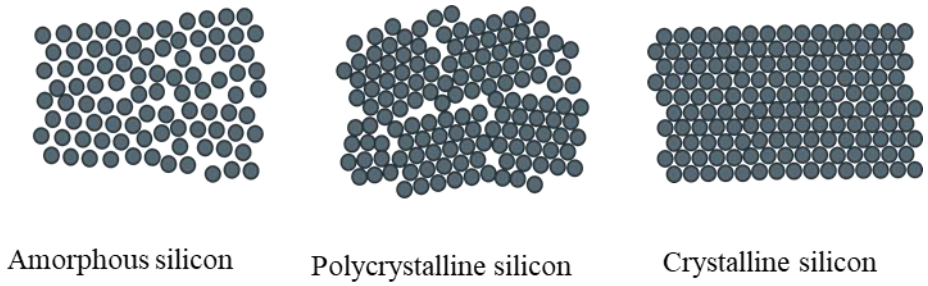

Figure 4.1 Common allotropes of silicon.

The crystallinity of the tapered SCF is characterised by two methods, the first is the Raman spectroscopy and the second is XRD. Raman spectroscopy characterises vibrational modes of molecules. It is a fast and non-destructive method for crystallinity characterisation. It can provide information of the degree of crystallinity of the silicon core, thus, providing quick feedback as to the fibre core quality. As shown in Fig. 4.2 [98], a-Si, p-Si and c-Si have different Raman response spectra. The peak width of the spectra depends on the degree of crystallization of silicon. The peak position depends on both the crystallization and the strain of the material. Single crystal silicon has the narrowest Raman peak at around 520 cm^{-1}. This peak is shifted to lower frequency with a larger bandwidth for a-Si.

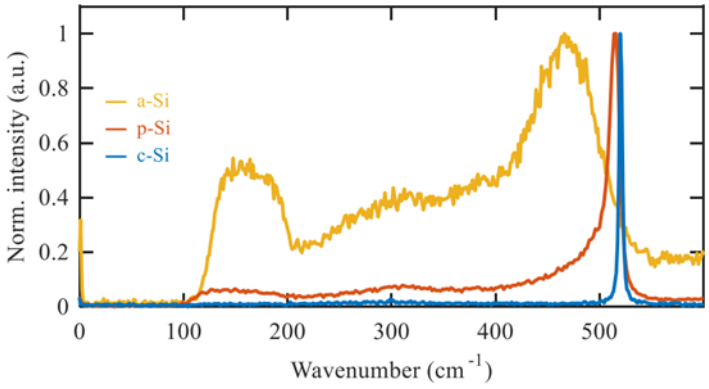

Figure 4.2 Raman response of the a-Si, p-Si and c-Si [98].

The Raman spectra of the tapered SCFs have been reported in Ref. [99]. However, the result is not conclusive enough to characterise the crystallinity of the SCF, as the Raman peak and bandwidth also depends on the stress level in the core [98]. The tapering process can modify compression or tensile stress in the fibre core due to the complex thermal dynamics.

XRD was used to further investigate the material properties of the SCF core in Ref. [99]. The XRD technique can determine the structure of a crystal by measuring the beam diffraction caused by the crystalline structure. A tapered SCF with a 2 µm core diameter and an as-drawn fibre were characterised and compared. As shown in Fig. 4.3, the core of tapered SCF has a more uniformed crystalline orientation along the fibre compared with the as-drawn fibre. Its grain length is also

much longer, up to 9 mm, whereas the as-drawn SCF has various different crystal orientation along the length. During the drawing process, the silicon core melts completely, and any crystal orientation is rewritten. The new orientation of the crystal is either depends on on the material interface or a random, spontaneous process.

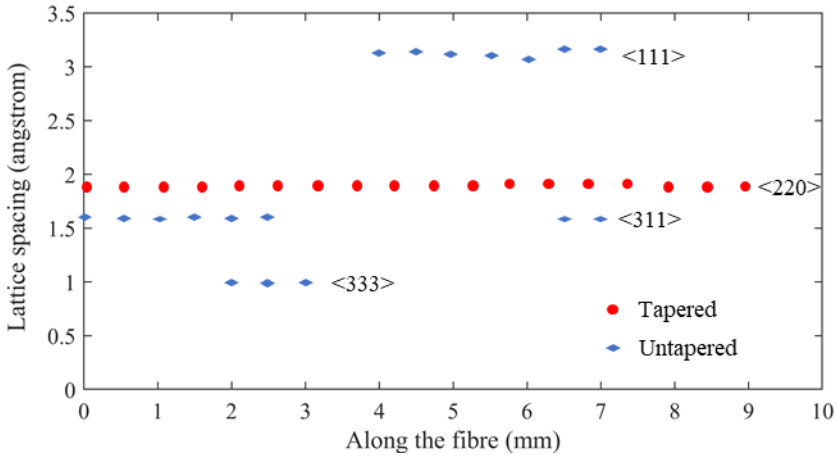

Figure 4.3 Lattice spacing of diffraction spots measured using XRD along tapered and untapered as-drawn SCF [99].

4.3 Linear transmission characterisation

4.3.1 Cutback method

The cutback method measures the difference in insertion loss of the fibre with different lengths, as illustrated in Fig. 4.4. It is a widely used method that is considered to be reliable and convincing. This method gives a good unit loss assuming the fibre loss is uniformly along the length. The drawback of this method is that it destroys the measured fibre section. Another limitation of this method is that it only reflects the average loss of the region removed from the fibre. If the fibre loss is not uniform, it will lead to large measurement errors. Maintaining the same coupling loss between measurements is also a challenge in practice.

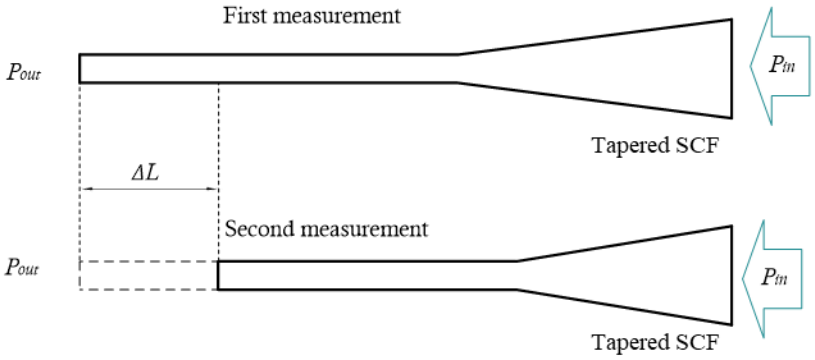

Figure 4.4 Loss measurement using cutback method.

Experiment setup

The experimental setup is shown in the Fig. 4.5, where a CW source is coupled into and out of a SCF using objective lenses. The light is collimated by an objective lens L_3 on $stage_4$. After passing through a beam splitter (BS, 90/10), the beam is launched into the fibre core via the objective lens L_1. CCD_1 camera (MicronViewer 7290A) is used for imaging the input fibre facet to precisely launch the beam into the fibre core. The coupling condition is controlled via $stage_1$, $stage_2$, $stage_4$ and mirrors M_1 and M_2. The objective lens L_2 is used to collect the light from the SCF. A pinhole is used to block the light transmitted in the cladding of the fibre. The output of the SCF is imaged on the CCD_2 camera to monitor the output mode profile. The input/output power is measured by the power detector (InGaAs Photodiode, Thorlabs S132C) PD_1/PD_2.

The insertion loss is defined as the ratio of the measured input and output power. After the insertion loss is measured, a short section of the fibre is removed via polishing before the fibre is replaced on the setup for another measurement. This process is repeated to obtain as many measurements as possible. The linear regression between the insertion loss (in dB) and fibre length is calculated, where the slope of the linear regression line represents the loss per unit length of the fibre.

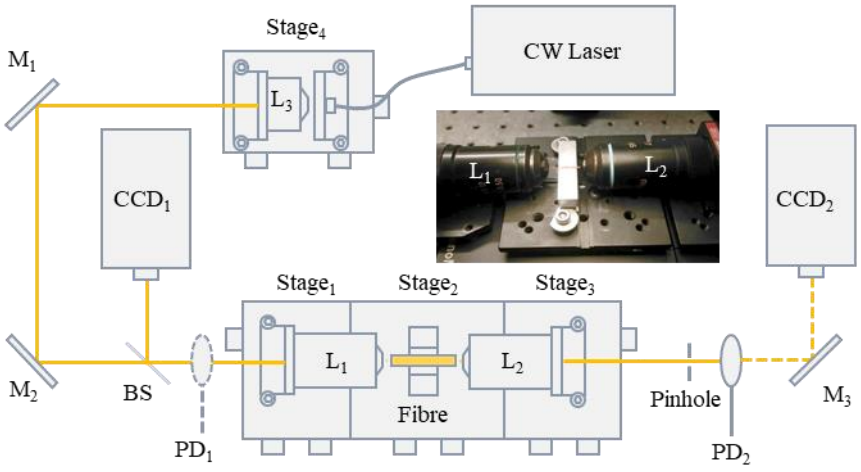

Figure 4.5 Schematic of transmission characterisation setup. Mirror (M), beam-splitter (BS), microscope objective lens (L), charge-coupled device camera (CCD), photo detector (PD).

Primary loss measurement results

In the early stage of this work, the as-drawn fibres were primarily designed for solar cell applications, thus the silicon used for the core was heavily doped, n-type silicon (D429, EL-CAT Inc.). The purity of the fibre core material was improved by using a purer silicon during later stages of the

work. Here in this section, the linear loss characterisations were carried out with the solar grade SCFs.

Fig. 4.6 (a) shows an example of cutback measurement of a tapered SCF with 2.5 µm core diameter. The output transition region is removed such that the core size at the output of the fibre is constant in each measurement, as shown in the inset. The insertion loss of this fibre was measured for 9 different lengths. The linear regression of the measured data is calculated. The fitted equation is $y = (4.7 \pm 0.36)x + 6.6$ (here y represents insertion loss, x represents fibre length). Therefore, the loss of this fibre is 4.7±0.36 dB/cm and the coupling loss is 6.6 dB. The coupling loss includes the reflection from the fibre facets, losses of the lenses, and the loss from the mode mismatch between the incoming beam and fibre facet.

Using the cutback method, a number of tapered SCFs with different fabrication conditions, core sizes and qualities were characterised. The losses of these solar grade as-drawn fibres were usually above 10 dB/cm at $\lambda = 1.55$ µm and 2-7 dB/cm after tapering. A summary of the lowest losses obtained with each different core diameter are plot in Fig. 4.6 (b). The red dashed line is a guide to the eye. It can be seen that as the core size decreases, the losses decrease dramatically. This is due to the larger grain sizes caused by higher cooling rates for smaller fibre core [24].

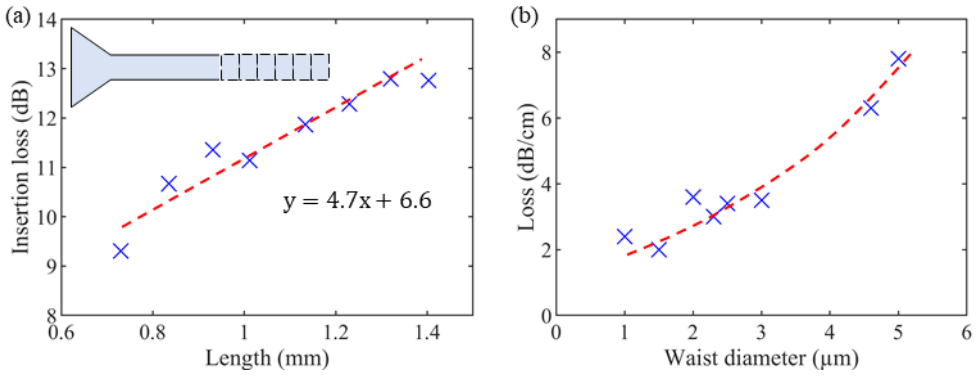

Figure 4.6 Cutback measurements of a SCF at 1.55 µm. (a) Insertion loss at different lengths. (b) The lowest loss obtained with various SCF core diameters. The red dashed line is a guide to the eye.

The wavelength dependency of the loss of these early SCFs was also characterised. The experimental setup is shown in Fig. 4.7, where the laser source used was a supercontinuum laser (Fianium SC450, with 6 ps pulse width and 20 MHz repetition rate) with an acousto-optic tunable filter (AOTF) used to select the wavelength. As the output beam profile from the AOTF depends on the wavelength, the beam after the AOTF is first coupled into a patch cord fibre in stage$_5$ and then collimated in stage$_4$ to maintain the same coupling condition into SCF for different wavelengths. All measurements were taken using a modest power (less than 100 µW) to minimise the nonlinear

absorption. To cover a wider wavelength range, a CW fibre laser source at 2 µm was also used in this measurement.

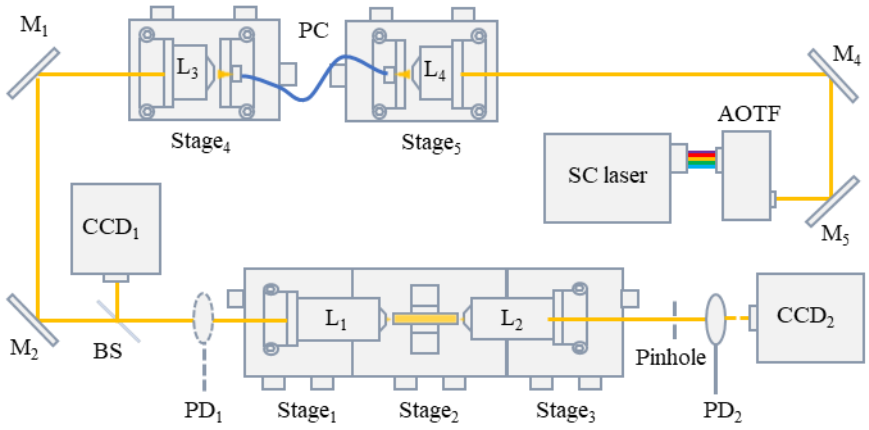

Figure 4.7 Schematic of multiple wavelength transmission characterisation setup. Mirror (M), beam-splitter (BS), microscope objective lens (L), charge-coupled device camera (CCD), photo detector (PD), patch cord (PC), acousto-optic tunable filter (AOTF), supercontinuum laser (SC).

The measured results are shown in Fig. 4.8. For wavelengths below 1.2 µm, the loss increases dramatically as the band edge of silicon is around 1.1 µm. The lowest losses are around 1.2 - 1.6 µm. The losses increase at longer wavelengths due to the effect of intrinsic FCA in this solar grade silicon material. The resistance of the raw silicon material used for the as-drawn fibre was 0.05-0.15 Ω·cm, which corresponds to carrier density of $4.6\text{x}10^{16}$-$2.4\text{x}10^{17}$ cm^{-3}. This level of free carrier density is high enough to cause significant FCA (a few dB/cm) [2]. Thus, it is important to use pure silicon as the core material to obtain higher transmission for longer wavelengths.

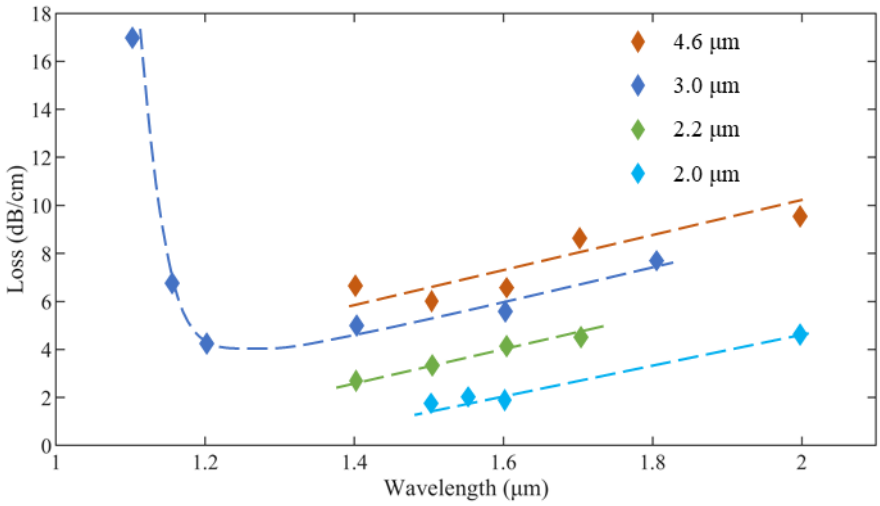

Figure 4.8 Losses of various core diameters solar grade tapered SCF at different wavelengths. Dashed lines are guides to eye.

Error in the cutback method

The main drawbacks of the cutback method for SCF loss measurements are that, firstly it destroys the measured sample, secondly, the measurements require extreme care to be conducted properly. To minimise the measurement error, the coupling condition of the input and output of the fibre need to remain unchanged. This is difficult in practice, as the sample needs to be polished for each measurement. The fibre facet condition can be slightly different after polishing. Variation of the size of the fibre core can change the coupling efficiency at the output of the fibre. When using a CW laser, the linewidth of the laser needs to be large enough to avoid the Fabry–Pérot cavity effect. Interference effects from the Fabry–Pérot cavity can easily introduce a few dB error in each measurement. These measurement errors can be reduced by taking repeated measurements, which is very time consuming, especially when measuring the losses for various wavelengths.

4.3.2 Fabry–Pérot method

Light transmission in a Fabry–Pérot cavity

The Fabry–Pérot cavity method is a fast and non-destructive method for the SCF loss measurements. It uses the interference pattern on the transmission spectrum to estimate the loss of the SCF. As the refractive index of silicon is much higher than air, the input and output fibre facets form a Fabry–Pérot cavity, as shown in Fig. 4.9.

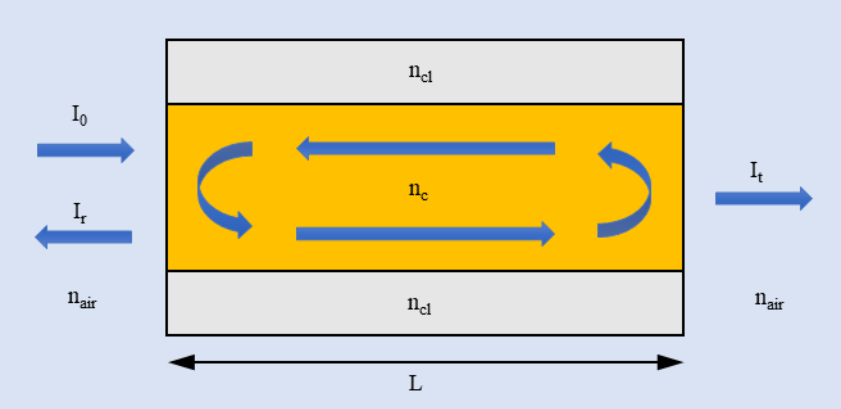

Figure 4.9 Schematic of a Fabry–Pérot cavity formed by SCF. I_0, I_r and I_t are input, reflected and transmitted light intensity.

The transmitted light intensity can be described by the well-known equation [28]

$$\frac{I_t}{I_0} = \frac{(1-R)^2 e^{-\alpha L}}{(1-Re^{-\alpha L})^2 + 4Re^{-\alpha L}\sin^2(\varphi/2)}, \qquad (4.1)$$

where R is the facet reflectivity, L is the cavity length, I_0, I_r, and I_t, are the input, reflected and transmitted light intensity. φ is the phase difference between successive waves in the cavity. I_t has

a maximum when $\sin^2(\varphi/2) = 0$ and a minimum when $\sin^2(\varphi/2) = 1$. Thus, Eq. (4.1) can be rewritten as

$$\xi = \frac{I_{max}}{I_{min}} = \frac{(1 + Re^{-\alpha L})^2}{(1 - Re^{-\alpha L})^2}, \quad (4.2)$$

where ξ is the ratio between the local maximum and minimum power transmission I_{max} and I_{min}. This equation can be rearranged to obtain the loss coefficient α as

$$\alpha = -\frac{1}{L} ln\left(\frac{1}{R}\frac{\sqrt{\xi} - 1}{\sqrt{\xi} + 1}\right). \quad (4.3)$$

As a result, the absorption coefficient can be obtained from measuring the maximum and minimum spectral response of the SCF and the fibre length.

Experiment and results

The experimental setup is similar to that for cutback measurements and is shown in Fig. 4.10. A tunable CW laser with very narrow linewidth is used. Light is first collimated via L_3 and coupled into the fibre via a microscope objective lens L_1 through mirrors M_1 and M_2. The output light from the SCF is then collected via another lens L_2 and coupled into a power meter via objective lens L_4. The power meter and the laser are controlled by a computer for wavelength tuning and data recording.

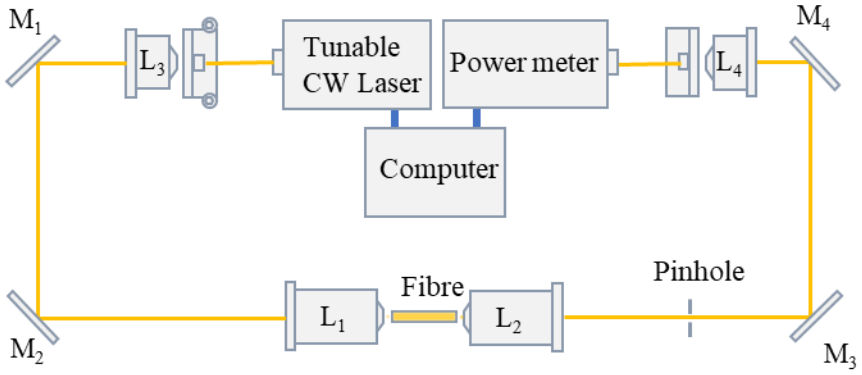

Figure 4.10 Experimental setup for Fabry–Pérot cavity measurements.

The tested sample was a tapered SCF with a 4 µm core diameter and 2.6 cm length. Its transition regions were removed so that the fibre diameter and material properties were approximately constant along the entire length. The silicon material used in this fibre (O212, EL-CAT Inc.) has a higher resistance of 15~22 Ω·cm than in Section 4.3.1, which has negligible intrinsic FCA. The tunable wavelength increment of the laser was set to be 1 pm. Fig. 4.11 shows the measured spectral response of the sample. The y axis is the ratio of transmitted/input light intensity. The interference pattern on the spectrum can be clearly seen in the figure. The loss coefficient is then

calculated to be 1 dB/cm using Eq. (4.2) and (4.3), assuming the reflectivity of the silicon/air interface is 30%.

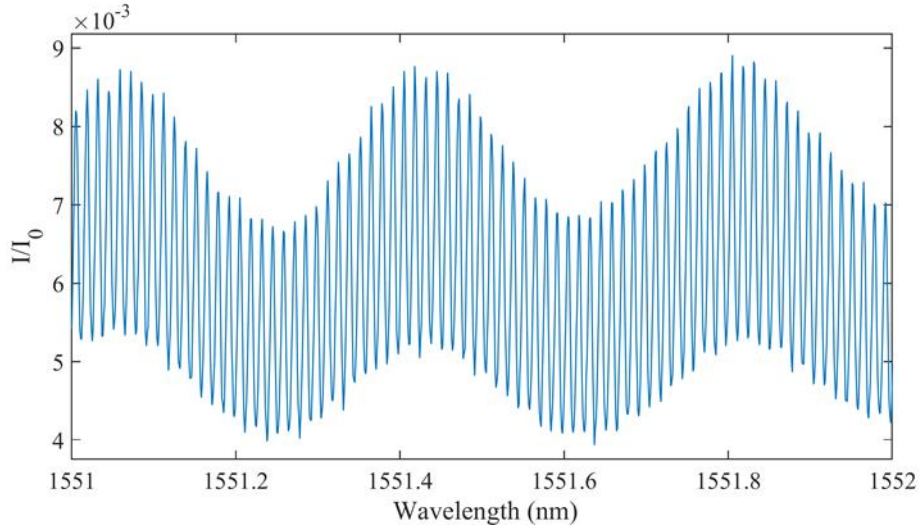

Figure 4.11 Spectra response of the SCF Fabry–Pérot cavity.

The free spectra range (FSR) of the interference pattern is defined as the distance between two peaks in the spectra. It is related to the centre wavelength λ_0, refractive index n and the effective length L of the cavity

$$FSR \approx \frac{\lambda_0^2}{2n \cdot L}. \qquad (4.4)$$

Using Eq. (4.4), the FSR of this fibre is calculated to be 0.01329 nm, with n = 3.4757 [73], L=2.6 cm, and λ_0 = 1.55 µm. It is almost identical to the value 0.0133 nm measured from the Fig. 4.11. This is evidence of the reliability of this method.

Discussion

There are a few considerations when using the Fabry–Pérot method for SCF loss measurement. It can be seen in the Fig. 4.11 that the envelop of the spectrum oscillates with a period of around 0.4 nm. This could be caused by other Fabry–Pérot cavities in the system (for example, patch cables and objective lenses). As the period of the envelop fluctuation is a much larger (30 times) than the FSR of SCF spectrum, using Eq. (4.4), the cavity length is calculated to be 2 mm. This indicates that this oscillation is most likely caused by the objective lenses whose thicknesses are in the order of a few millimetres. However, this assumption is proved to be wrong. When the SCF is absence, the oscillation disappears. It still requires further investigation to explain this envelop oscillation. In practice, the focused beam at the fibre facet could have a small angle with the fibre axis, the facet reflectivity will then be smaller than 30%, which can also lead to a larger calculated loss value. Therefore, the loss coefficient measured by the Fabry–Pérot provides the upper bound on the loss

of the sample. The loss values from the Fabry–Pérot method are comparable with the values from the cutback method. However, the bandwidth of this method is limited by the laser facility available (λ = 1.5–1.6 μm). Thus, most of the loss characterisation is measured by the cutback method.

4.4 Nonlinear properties of the SCFs

The nonlinear parameters of silicon such as TPA and nonlinear Kerr coefficient n_2 across the telecoms band up to the mid-IR have been reported in bulk crystalline silicon wafers and SOI waveguides [100]–[102]. However, the nonlinear property of SCFs fabricated via the MCD method were yet to be fully characterised. The nonlinear properties of the SCFs were first characterised in telecommunications band in our group via analysing the nonlinear transmission using a short pulsed pump source [24]. In this section, I extend the characterisation of the SCFs to the mid-IR from 1.5-2.5 μm, which covers the telecommunication c-band up to the TPA cut-off wavelength of silicon.

4.4.1 Transmission characterisation

The sample used in this characterisation is a tapered SCF with a core diameter of 3 μm (material type: high purity silicon, O212, EL-CAT Inc.). Both sides of the taper transition were removed so that the fibre diameter was constant along the length. This core dimension is chosen as the fibre has a normal dispersion in the wavelength range of interest. We prefer the fibre to have normal dispersion as nonlinear effects such as FWM and modulation instability can be avoided. The optical transmission measurement was conducted using the experimental setup shown in Fig. 4.12. Two different lasers were used to cover the wavelength range of interest. The wavelength region from 1.7-2.5 μm was studied using a Ti:sapphire pumped femtosecond optical parametric oscillator (OPO) with an 80 MHz repetition rate and pulse width between 90-200 fs (FWHM). To study propagation in the telecommunications band, a fibre laser at 1.54 μm with a 650 fs pulse duration and 40 MHz repetition rate was used. The light was coupled into and out of the SCF via free space coupling using a silica microscope objective lens L_1 and L_2 (NA=0.85). The output beam was then coupled into a mid-IR optical spectrum analyser (OSA: Yokagawa AQ6375) via another objective lens L_3. The pump power was controlled via a variable optical attenuator. The linear propagation loss was measured using the cutback method.

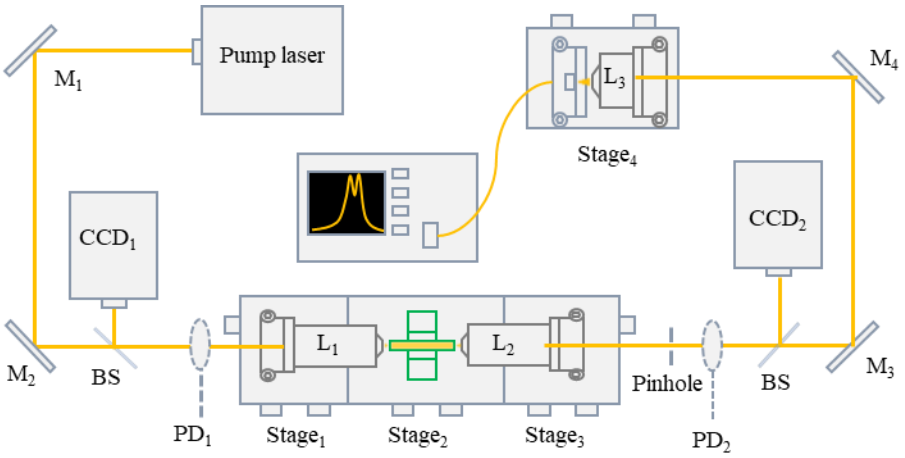

Figure 4.12 Schematic of the transmission setup. Beam-splitter (BS), photo detector (PD1 & PD2), microscope objective lenses (L1 & L2), CCD Cameras (CCD1 & CCD2), optical spectrum analyser (OSA).

As shown in the Fig. 4.13 (a), the loss of this SCF measured by the cutback method stays consistently around 2 dB/cm over the entire wavelength region. The remaining fibre has a length of 11 mm. There is a small difference (1 dB/cm) between the value measured by the cutback method and the Fabry–Pérot method, also reported in Fig. 4.13 (a). This could be caused by a non-uniform loss distribution along the fibre. The slightly increasing loss for longer wavelength could be caused by the mode interaction with the silica cladding, which has higher absorption at longer wavelengths. The coupling loss is 5.6 dB at 1.54 µm. It increases to 11.8 dB at 2.5 µm, as shown in Fig. 4.13 (b). This is primarily caused by the increasing light absorption of the microscope lenses. The absorption of the two silica lenses increases by 2 dB each as the wavelength increased from 1.5 to 2.5 µm. The coupling loss due to the mode mismatch at the fibre input and light collection efficiency at the fibre output increased by 2 dB, as the focused beam size changes slightly with the wavelength due to the chromatic aberration of the objective lens.

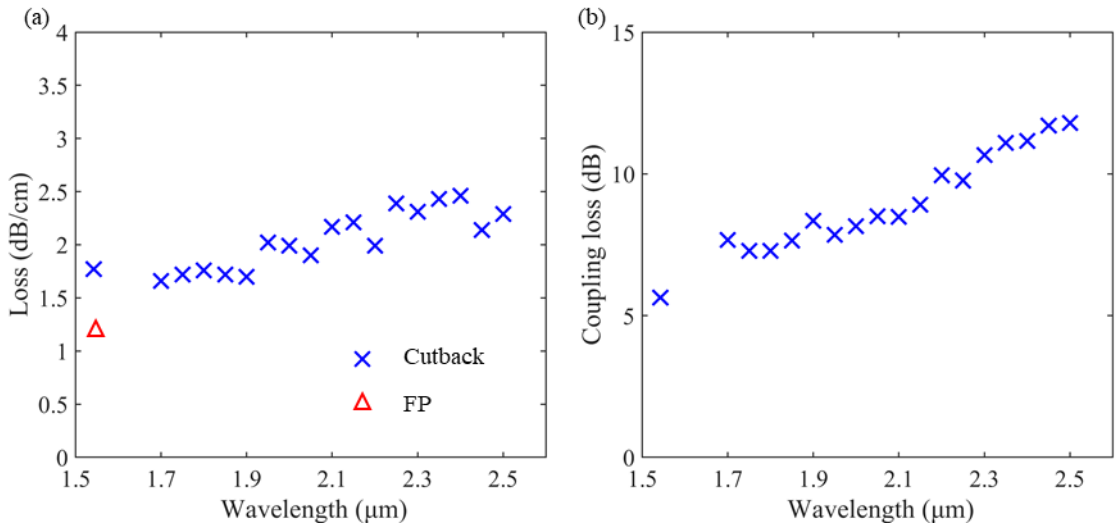

Figure 4.13 (a) Transmission loss measured by the cutback method compared with the Fabry–Pérot method. (b) The coupling loss at different wavelengths.

4.4.2 Nonlinear absorption characterisation

To measure the TPA coefficient, the transmission of the fibre was measured with different input powers. When the input power increases, the nonlinear absorption becomes stronger until the transmitted power is saturated. The nonlinear transmission of a SCF can be described as [47]

$$\frac{dI}{dz} = -\alpha I - \beta_{TPA} I^2 - \sigma_{FCA} N_c I, \qquad (4.5)$$

with N_c determined by the TPA coefficient β_{TPA} and free carrier lifetime τ_c in Eq. (2.68). To determine the value of β_{TPA}, the measured input and output powers were fit using numerical calculations based on Eq. (4.5).

The experimental setup is the same as described in Section 4.4.1. The coupled pulse peak power is derived from the input and output average power excluding the coupling efficiencies. As most of the power is coupled into the fundamental mode, the effective mode area of this mode was calculated to be 3.7 μm^2. This value is used for all wavelengths as it has only a negligible change with the wavelength. Fig. 4.14 (a) shows the nonlinear absorption curves at different wavelengths (the output power of each wavelength is normalised for comparison). It can be seen that the nonlinear absorption decreases with increasing wavelength. For wavelengths from 1.75 to 2.15 μm, the nonlinear absorption starts to be obvious when the power exceeds ~2 GW/cm^2. At 1.54 μm, the nonlinear absorption is particularly severe, so that it starts to saturate after 1 GW/cm^2. At 2.35 μm, where the wavelength is beyond the TPA edge (2.2 μm) of silicon, the output power has an almost linear relation with the input power, with the additional loss from nonlinear absorption being only ~0.3 dB at a coupled peak intensity of 8 GW/cm^2, which is negligible. The peak intensity level used in this experiment is insufficient to observe the power saturation caused by the 3PA, though it will limit the intensity level beyond the TPA edge [103].

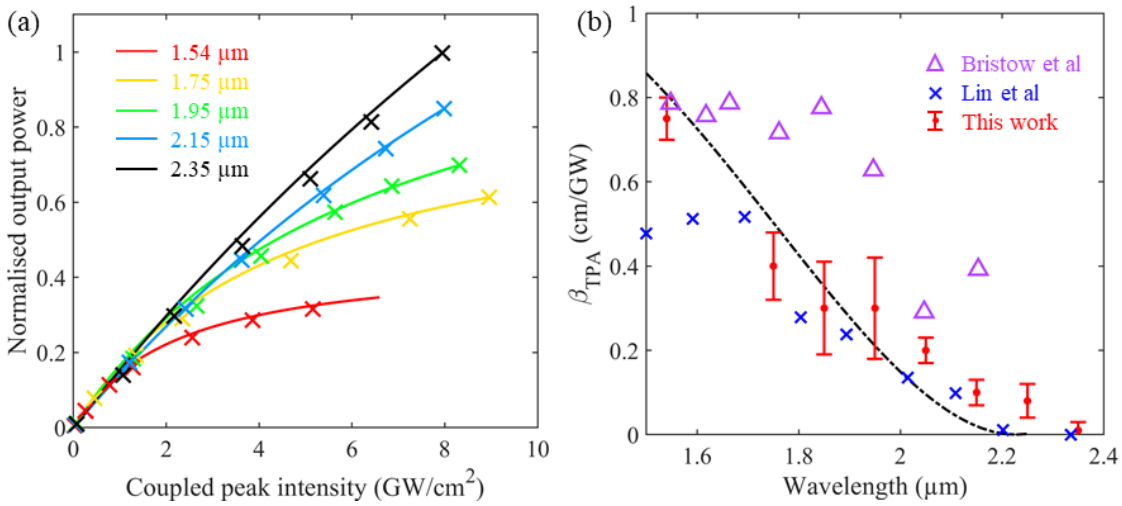

Figure 4.14 (a) Nonlinear absorption measurements for different pump wavelengths. The solid curves are the simulated fits for the corresponding wavelength given in the legend. (b) Measured TPA parameter as a function of wavelength, together with data points from measurements by other groups [100], [101]. Error bars represent the uncertainty in the input powers. Dashed line is theoretical fits based on calculations of Garcia and Kalyanaraman [104].

The obtained TPA coefficients are presented in Fig. 4.14 (b). The β_{TPA} drops from ~0.75 cm/GW to ~0.1 cm/GW from 1.54 μm to 2.3 μm. That is, it becomes negligible after the TPA edge. Previous measurements of the TPA parameters that were presented in Refs. [100], [101] are also listed for comparison. It can be seen that although there are small differences for the different studies, these measurements follow a similar decreasing trend with decreasing wavelength. We believe that some of the differences are caused by the silicon material used, as our fibres are p-Si so the values will depend on the number of grains present. It could also be due to measurement errors, such as uncertainties in the coupling efficiency and pulse profile (that is, pulse peak power). It is worth noting that all of these these works have made use of mid-IR femtosecond laser sources, whose pulse duration and pulse profile usually contains large uncertainties. To reduce the measurement error, the pulse durations of the OPO at different wavelengths were measured via an auto-correlator. As shown in Fig. 4.15, these results have large uncertainties due to the poor stability of the OPO. Reducing the uncertainty to obtain highly accurate values of the nonlinear parameters in the SCFs will be part of our future wok when more advanced mid-IR sources are avaliable. Nevertheless, these experimental measurements follows the theoretical fits based on calculations of Garcia and Kalyanaraman [104], as shown by the dashed line in Fig. 4.14 (b).

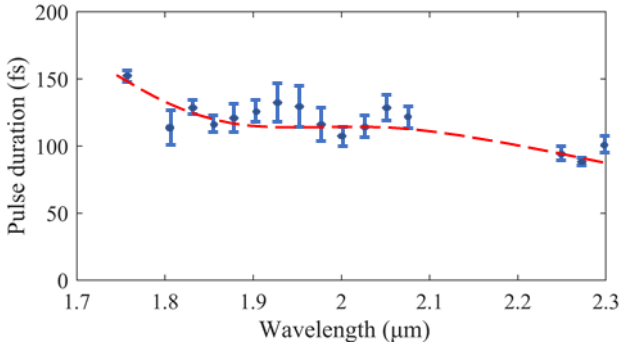

Figure 4.15 Pulse duration of the OPO measured by a mid-IR auto-correlator. The red dashed line is a guide to the eye.

4.4.3 Nonlinear refraction characterisation

The nonlinear Kerr index n_2 of a bulk optical material is usually characterised by the Z-scan technique. For waveguides, the n_2 is usually studied by measuring the size of nonlinear effects such as SPM [105] and or XPM [106] with different power levels. The SCFs in this work were characterised by measuring the spectral broadening induced by SPM. The value of n_2 can then be determined by fitting the numerical data obtained from the NLSE Eq. (2.50) to the experimental results. n_2 is first characterised at λ =1.54 μm. The experimental setup is the same as used for the TPA characterisation, as described in the previous section in Fig. 4.12. The spectral evolution with increased coupled peak intensity is shown in the Fig. 4.16. The numerical curves (shown as the black dashed lines) are in reasonable agreement with the measured spectra with the same input peak intensity. Table 4.1 shows the -20 dB bandwidth of these spectra, it can be seen that the numerical results are in good agreement compared with the experimental measurements. The estimated value of n_2 is ~0.42×10^{-13}cm^2/GW, which is similar to the value reported from previous work [24].

To study the dispersion of n_2, the same protocol is repeated for wavelengths between 1.75-2.35 μm with the OPO source. A selection of results are shown in Fig. 4.17. The spectral broadening increases as the wavelength increases with same coupled peak intensity. We found that the pulses from the OPO are not transform limited by comparing the spectral bandwidth and the pulse duration before propagating through the SCFs. Therefore, a small chirp C ∼ −1.1 is added to the input pulse [107]. Although this could increase the uncertainty of the obtained n_2, we found the measured spectra are still in good agreement with the simulations in terms of bandwidth, as shown in the Table 4.2.

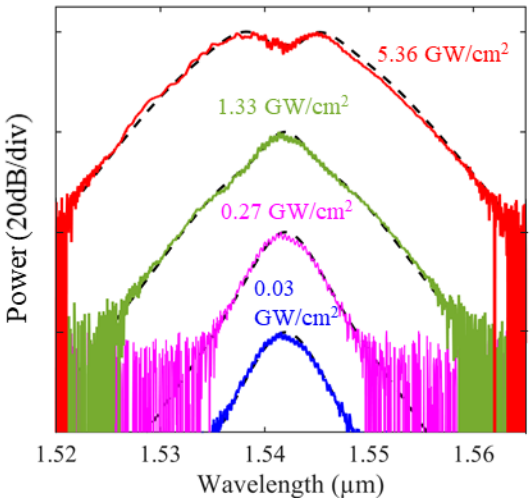

Table 4.1. -20 dB band width for λ=1.54 μm

Coupled Intensity (GW/cm²)	0.03	0.27	1.33	5.36
Experimental bandwidth (nm)	13	13	20	30
Simulated bandwidth (nm)	13	13	20	30

Figure 4.16 Spectral evolution with different coupled peak intensities at 1.542 μm.

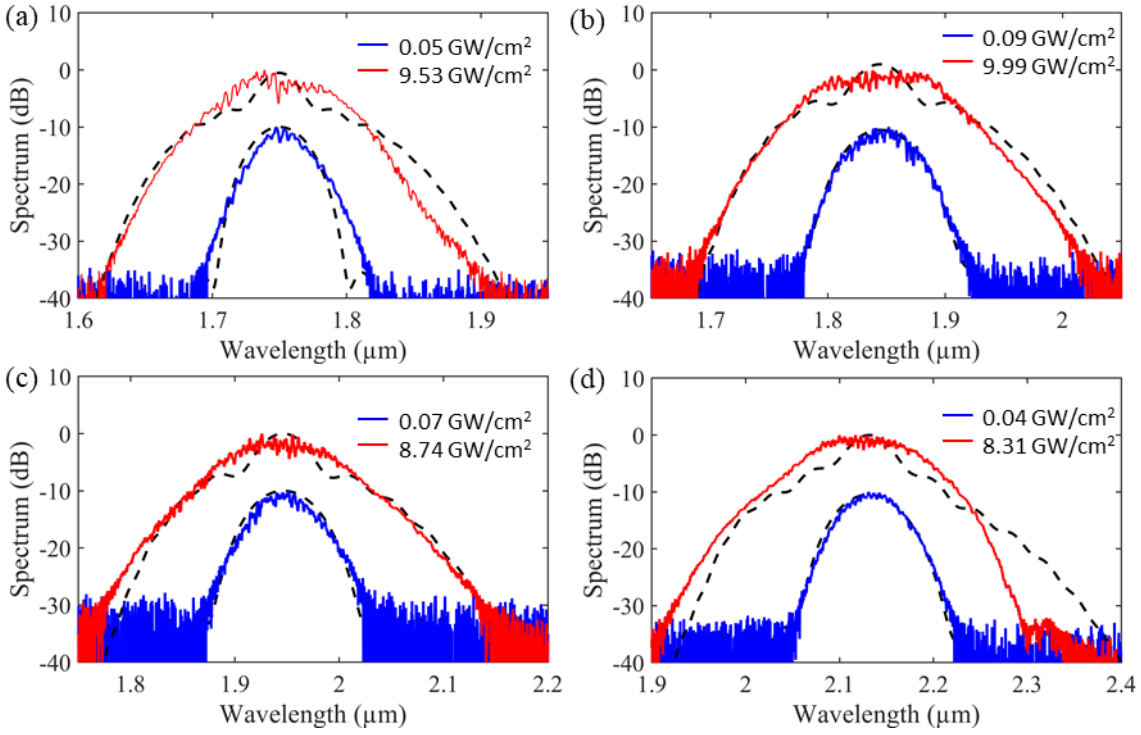

Figure 4.17 Experimental transmission spectra as a function of pump centre wavelength: (a) 1.75 μm, (b) 1.85 μm, (c) 1.95 μm and (d) 2.15 μm. The dashed lines are numerical fits obtained by solving the generalised NLSE. The normalised spectra are offset for clarity.

Table 4.2. -20 dB band width for selected pump wavelengths

Wavelength (μm)	1.75	1.85	1.95	2.05	2.15	2.25	2.35*
Experimental bandwidth (nm)	192	250	281	281	303	321	168
Simulated bandwidth (nm)	218	264	280	285	326	318	178

*Bandwidth taken at -10 dB due to OSA's maximum measurable wavelength of 2.4 μm.

The corresponding values of n_2 are shown in Fig. 4.18 (a). As the wavelength changes from 1.54-2.35 µm, the n_2 first increases significantly from 0.4×10^{-13} cm^2/GW to 1×10^{-13} cm^2/GW, then it decreases slowly as the wavelength increases, down to 0.7×10^{-13} cm^2/GW at 2.35 µm.

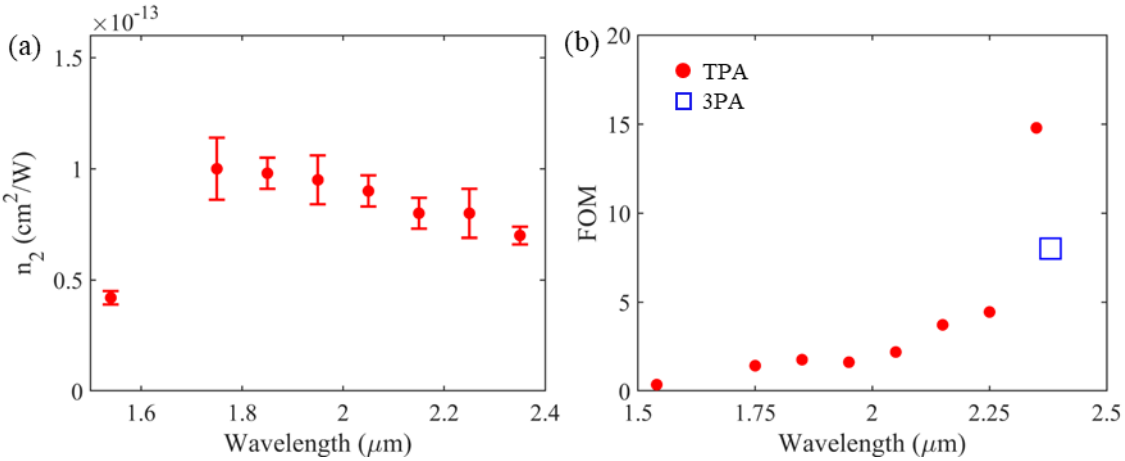

Figure 4.18 (a) Wavelength dependence of the Kerr nonlinear coefficient n_2 for a tapered SCF. Error bars represent the uncertainty in the input pulses power. (b) Wavelength dispersion of the FOM_{NL}.

The dispersion of the nonlinear figure of merit (FOM_{NL}) of the SCF is calculated by using the definition $n_2/\lambda\beta_{TPA}$, as shown in the Fig. 4.18 (b). It can be clearly seen that, the FOM_{NL} increases with increasing wavelength. The FOM_{NL} in the telecommunications band has the lowest value of ~0.36, which limits the nonlinear performance of the SCFs in this region. However, this is also a general conclusion for all silicon-based waveguides. The increasing trend of the FOM_{NL} suggests that these fibres are more suitable for nonlinear applications for wavelengths toward mid-IR region. At 2.35 µm, where TPA disappears, the FOM_{NL} is no longer an accurate measure of the nonlinear performance as 3PA becomes the dominant nonlinear absorption effect in this wavelength region. The FOM_{NL} is then defined as $n_2/\lambda\beta_{3PA}I$, where I is the light intensity inside the nonlinear medium. Using data for the 3PA parameter of single crystal silicon from the literature [103], the FOM_{NL} just beyond the TPA cut-off wavelength is calculated using a typical value I=1 GW/cm^2 for comparison. This is shown as the square data point in Fig. 4.18 (b). Even using this definition, the FOM_{NL} keeps increasing for longer wavelengths, so the SCF is expected to have higher nonlinear performance in this region. However, this should be verified by future work as it is possible that multiphoton absorption such as 3PA may eventually limit the nonlinear performance [108].

4.5 Conclusion

In summary, this chapter has reviewed the material properties of the tapered SCFs in terms of their crystallinity and then characterised both the linear and nonlinear transmission properties of MCD

SCFs from telecom wavelengths up to the TPA edge in the mid-infrared regime. The linear loss was characterised using both the cutback method and the Fabry-Pérot method. The nonlinear refractive index and TPA were characterised by fitting simulations of the nonlinear propagation with experimental data. The low loss, high nonlinear properties of the SCFs make them a promising platform for nonlinear photonic devices in the infrared regime, especially beyond 2 μm where applications include free-space communications, gas detection and medical diagnostics.

Chapter 5 Mid-infrared supercontinuum generation

5.1 Introduction

In this chapter, we experimentally and numerically study femtosecond pumped SCG in the SCF platform. To begin with, the group velocity dispersion and cladding loss SCFs with different diameters are studied. On this basis, we first tried to observe SCG in straight SCFs, with some preliminary results obtained. To improve the SC bandwidth, SCFs with tapered profiles were tested. By analyzing the results, we found that the tapered fibre profile can greatly improve the spectral broadening. The studies of SCG in tapered fibres are divided into two sections, where the fibre profile has been designed for different wavelength bands (SWIR and MWIR). The broadest spectrum obtained in this work is from 1.65 μm to 5.3 μm (1.7 Octave). Using numerical simulations, this SCG is shown to be highly coherent. Furthermore, we show that theoretically the SC spectrum can be further optimised by tailoring the taper profile so that it can cover the full transmission window of silicon in the mid-IR. This work could provide a crucial step toward cheap, robust all-fibre mid-IR broadband sources.

5.2 Review of mid-IR SCG

To date, mid-IR SC has been demonstrated in a range of materials in both fibre and planar waveguide platforms. The best mid-infrared spectra have been demonstrated in the non-silica soft glass fibre systems made from chalcogenide [109], fluoride [110] and non-silica oxides [111], primarily due to their power handling capabilities and broadband transmission properties. However, there are challenges to working with these materials as they are not as stable or robust as their silica counterparts and, in the case of the chalcogenides, they often contain toxic compounds. Alternatively, SC systems employing highly nonlinear Group IV semiconductor materials can avoid these issues. The most common form of group IV waveguides are the SOI nanophotonic wires and these small core waveguides usually suffer high coupling loss (typical 5-10 dB per facet) and increased core/cladding interactions. As a result, the best SCG in SOI waveguides has been so far limited to the SWIR band, due to the heavy material absorption from the silicon dioxide layer. A few state-of-art platforms have been developed to extend the transmission window to the MWIR band and achieved broader SC to longer wavelengths. A review of mid-IR SCG over the past 10 years in Group IV platforms is shown in Table 5.1 and Fig. 5.1. Most of these SC sources were pumped with femtosecond laser sources in the range λ = 2 - 4 μm. The conversion efficiency of SCG in is defined as the ratio between input and output power, which is usually very low for silicon

waveguide, typically below 10% due to propagation loss and unoptimised waveguide structure. A recent work using a SiGe platform is shown in Ref. [112] has been the best SCG so far in the Group IV platforms. It has a 1.5 octave frequency span and 48% conversion efficiency. Though, for most Group IV platforms, generating broad band SC efficiently in the mid-IR is still a challenge.

Table 5.1 Summary of SCG in Group IV waveguide in recent 10 years.

Year	Platform	Linear loss (dB/cm)	SCG Bandwidth (μm)	Pump wavelength (μm)	Pump duration (fs)	Efficiency (on-chip)	Ref
2018	SiGe	1	3 - 8.5	4.15	200	~48%	[112]
2018	Si-Al_2O_3	5 - 7	2.5 - 6.2	3	100	4%-8%	[113]
2018	SOI	1.5	1.2 - 2.4	1.9	>50	N/A	[114]
2015	Si-Al_2O_3	1	1.9 - 6	3.7	320	<10%	[13]
2015	SiGe	2	1.4 - 2.8	2.4	90	~16%	[115]
2015	SOI	0.2	1.5 - 3.2	2.3	70	N/A	[116]
2014	SOI	N/A	1.5 - 3.67	2.5	300	N/A	[43]
2014	SCF	0.8-2.8	1.64 - 3.1	2.4	300	N/A	[20]
2011	SOI	2.5	1.5 - 2.5	2.15	2000	N/A	[9]

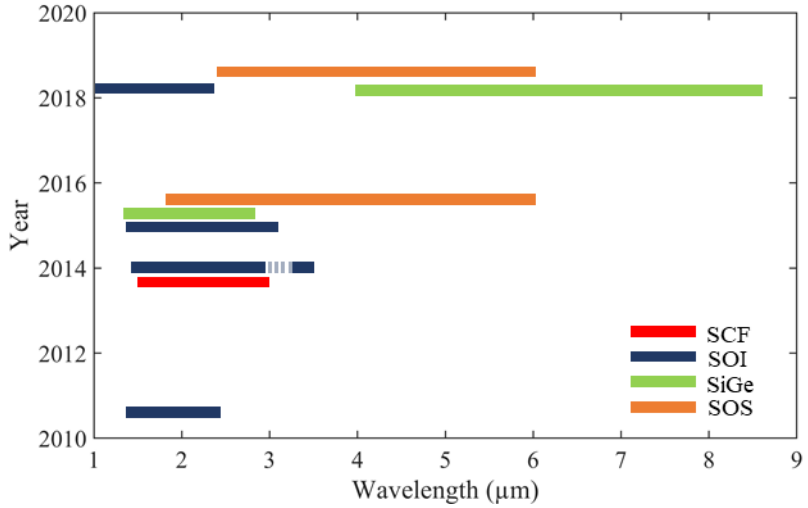

Figure 5.1 Summary of SCG in silicon-based waveguide in recent 10 years.

5.3 Transmission window and dispersion map

Silicon is transparent up to 8 μm. However, when silicon is surrounded by silica, such as in SOI waveguides and SCFs, the transmission window will be affected by the cladding absorption for wavelengths beyond 2.5 μm, where silica starts to be less transparent. The degree of this effect depends on the mode field distribution that spreads in the cladding and the wavelengths. It also depends on the material purity of silica glass. To study the cladding absorption in the SCFs, the loss from the cladding is numerically calculated by the finite element method (FEM) by including the imaginary component of the refractive index of silica adapted from literature [117]. Fig. 5.2 (a) shows the absorption map of the fundamental mode in a SCF as a function of core diameter and

wavelength. It can be seen that the losses at mid-IR wavelengths are not significant when the core size is large. For example, a SCF with a core diameter of 3 µm exhibits a propagation loss of 10 dB/cm at a wavelength of 5.2 µm, but when the core diameter is 6 µm, this loss is reduced to 1 dB/cm. When the core diameter is 9 µm, the transmission window is extended to 7.7 µm if 3 dB/cm is used as a dividing line.

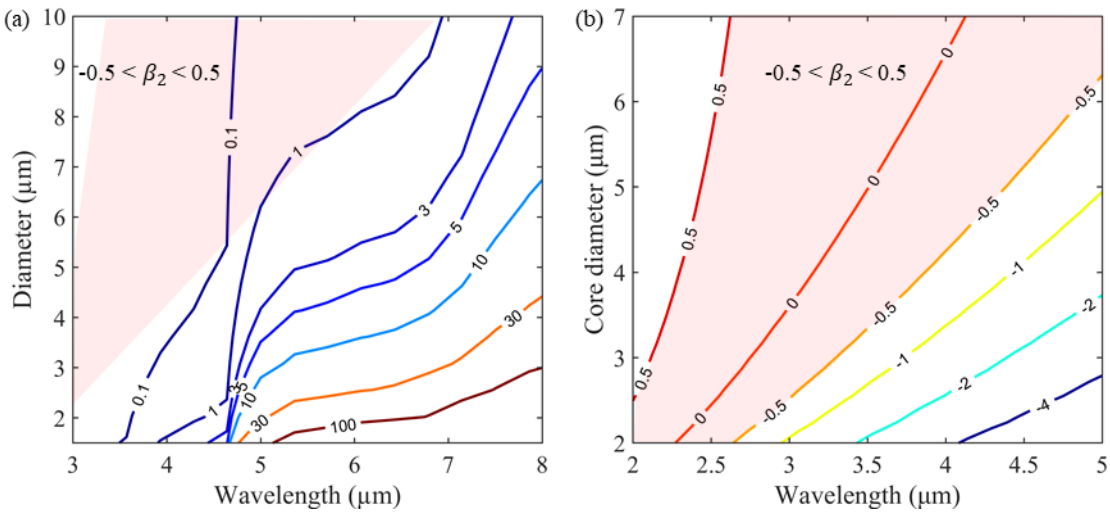

Figure 5.2 (a) Simulated absorption map in dB/cm as functions of wavelength and fiber core diameter. (b) Contour map of GVD parameters $\beta_2(\mathrm{ps}^2/m)$ as functions of fiber core diameter and wavelength. The pink areas in (a) and (b) shows when β_2 lies between -0.5 and 0.

The physics of SCG primarily depends on the pump pulse duration and the GVD of the fibre. When using femtosecond pulses, SCG is dominated by SPM and soliton dynamics. When pumping in the normal dispersion region, SCG is dominated by SPM. When pumping in the anomalous dispersion region, SCG is dominated by soliton fission and dispersive wave (DW) emission [39]. The broadest SCG often happens when β_2 is negative and close to zero [39]. As β_2 depends on both the fibre core size and wavelength, β_2 is shown on a contour map in Fig. 5.2 (b). In the upper left region, β_2 is positive; in the bottom right region, β_2 is negative. For efficient wavelength conversion, ideally the pump wavelength and fibre core diameter need to be in the region where the absolute value of β_2 is small. For example, if β_2 is between 0.5 and -0.5 ps^2/m, the pump wavelength and fibre diameter should be in the pink area of Fig. 5.2 (b). This area is also highlighted in Fig. 5.2 (a). It can be seen that the cladding absorption is below 1 dB/cm in this area, indicating that the cladding absorption has a negligible effect at the pump wavelength.

5.4 Modelling of supercontinuum generation in silicon core fibres

5.4.1 Modified NLSE model for supercontinuum

We use the NLSE to model the SCG process. As the SCG process is a combination of all the nonlinear effects in the fibre. To be effective, additional terms including the third order dispersion, 3PA effect, and wavelength dependent loss are included in the equation. The Raman effect is considered to be negligible for femtosecond pump sources and therefore is not included in the model. As the pump is positioned beyond TPA edge of silicon, the TPA term is also not included in the equation. The modified NLSE is an extension of Eq. (2.67) and can be written as [13]

$$\frac{\partial A}{\partial z}+\frac{i\beta_2(d)}{2}\frac{\partial^2 A}{\partial t^2}-\frac{\beta_3(d)}{6}\frac{\partial^3 A}{\partial t^3}=i\gamma(d)|A|^2A-\frac{\beta_{3PA}|A|^4}{2A_{eff}^2(d)}A-\frac{1}{2}(\alpha(d,\lambda)+\sigma)A \qquad (5.1)$$

where d is the fibre core diameter which depends on the location of taper profile, β_{3PA} is the 3PA coefficient and $\alpha(d,\lambda)$ is the wavelength dependent absorption coefficient, which is also related to the fibre diameter. The wavelength dependent loss is obtained from the finite element method (FEM) simulations as discussed in Section 5.2.

The free carrier density N_c introduced via 3PA in the fibre due to the presence of the pump can be calculated by [13]

$$\frac{\partial N_c}{\partial t}=\frac{\beta_{3PA}}{3h\nu}\frac{|A|^6}{{A_{eff}}^3(d)}-\frac{N_c}{\tau_c}. \qquad (5.2)$$

5.4.2 Flow chart of modelling

The flow chart of the numerical modelling is shown in the Fig. 5.3. As discussed in Section 2.3.3, Eq. (5.1) can be solved numerically via the split-step Fourier method. For a tapered fibre where its core diameter changes along the fibre, its dispersion properties, linear loss and effective mode area change with the fibre core diameter. These parameters need to be updated for every small step the pulse propagates. As shown in the figure, the nonlinear effect, dispersion and losses are applied to the pulse step by step. The nonlinear step needs to be solved in time domain and the dispersion and linear loss needs to be solved in frequency domain.

The propagation step size is usually set to be a few microns to tens of microns to have a relatively accurate result. The criteria for the step size can be determined by the maximum step size that gives convergent results. The same rule applies to the window size and resolution of the pulse in the time and spectral domains. The window size needs to be much larger than the pump pulse

duration, whilst the sampling frequency needs to be power of 2 for fast Fourier transform (FFT) calculations and is typically in the order of 2^{12}-2^{16}.

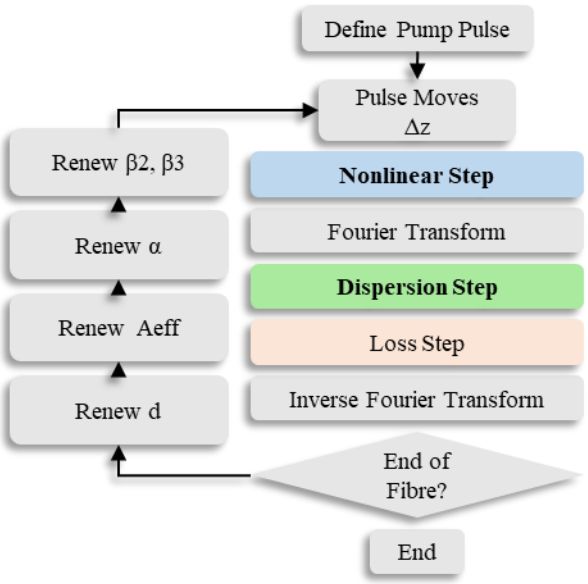

Figure 5.3 Flow chart of the NLSE modelling for propagation in a tapered SCF pumped by an ultrafast laser.

5.5 SCG in straight fibre structure

In our initial investigations we tried to generate SCG in a tapered SCF with both down and up taper transitions removed. As the core size is constant, the dispersion, loss and effective mode area are all constant along the fibre, which makes the fibre design and analysis of the results much easier compared to studies of fibres with tapered profiles.

The experimental setup for SCG is shown in Fig. 5.4. A Ti: sapphire-pumped OPO with a pulse duration in the range 90-200 fs (FWHM) and a 80 MHz repetition rate was used as the pump source. The beam is guided by two mirrors M_1 and M_2 and launched into the SCF via lens L_1. The reflection from the fibre input facet is collected by the lens L_1 and guided by a beam splitter BS_1 to a CCD_1 camera to monitor the input injection. The output light is collected by another lens L_2 and guided into CCD_2 camera for output monitoring. The input coupling can be optimised by the mirrors M_1, M_2, and the optical stages to ensure most of the light is coupled into the fundamental mode of the fibre. Finally, the output light is coupled into a mid-IR fibre that is connected to an OSA via lens L_3. When the output spectrum is beyond the range of the OSA (2.4 µm), it is guided to a monochromator (Bentham TMc300), which has a wider working range detector (1-5.5 µm, Photodiode, DH_INSB Dewar-Cooled). The signal is then amplified and recorded by a computer.

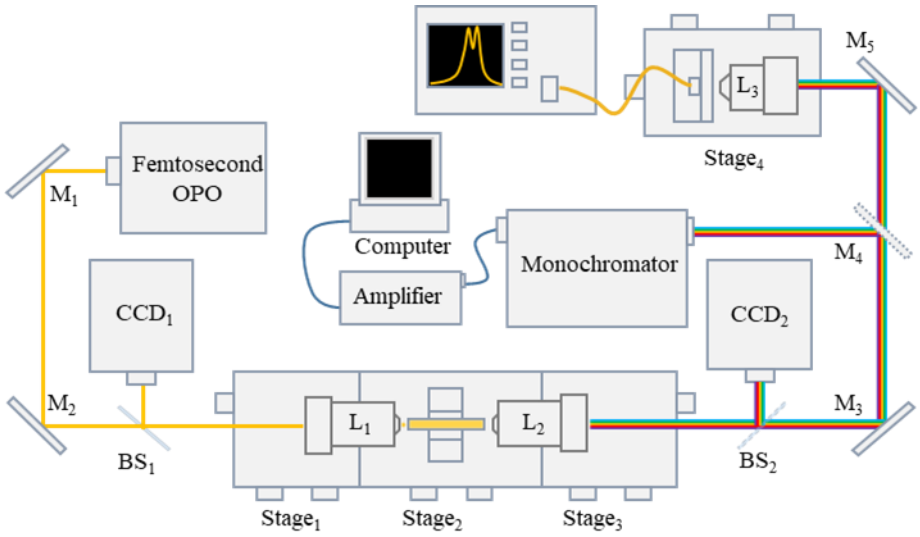

Figure 5.4 Experimental setup of SCG in a SCF. The pulsed pump source is coupled into the tapered SCF with a lens (L1). The output light is collected with a second lens (L2) and measured by an OSA or a Monochromator. Beam splitters (BS1 and BS2) are used to direct light at the fibre input and output facets onto CCD cameras (CCD1 and CCD2) to monitor the coupling.

5.5.1 SCF with a 2 µm core diameter

The pump wavelength for SCG in silicon is usually beyond 2 µm to avoid strong TPA. Thus, referring to Fig.5.2 (b), the fibre should have a small core size to have a small β_2. Furthermore, smaller fibres offer tighter mode confinement and thus higher intensities that lead to lower power thresholds for SCG. As a result, a fibre with a 2 µm core diameter was chosen (Material of core: O212, EL-CT Inc.). Although SCFs with smaller core sizes can be fabricated, the coupling efficiency will be much lower. The zero-dispersion wavelength (ZDW) for this fibre is 2.25 µm. The loss of the fibre was ~3 dB/cm, measured near the ZDW wavelength using the cutback method. After the cutback measurement, the remaining fibre length was 8 mm.

The fibre was pumped at wavelengths from 2 µm to 2.35 µm with various pump powers. As shown in Fig. 5.5, the generated spectrum broadens when the pump power increases. The power values used in the figure are the coupled average power. As shown in Fig. 5.5 (a), when the fibre is pumped at 2 µm, the pump is in the normal dispersion region that is away from the ZDW, thus, the SCG process is dominated by SPM. The spectrum of the pump pulse needs to cross the ZDW into the anomalous dispersion region to allow for significant spectral broadening. It can be seen that pumping at λ = 2 µm is not close enough to the ZDW so the SC bandwidth is limited. When the pump wavelength moves slightly closer to the ZDW at λ = 2.1 µm, as shown in Fig. 5.5 (b), the

spectrum of the pulse can easily across the ZDW at λ = 2.25 µm, leading to a much wider SC bandwidth.

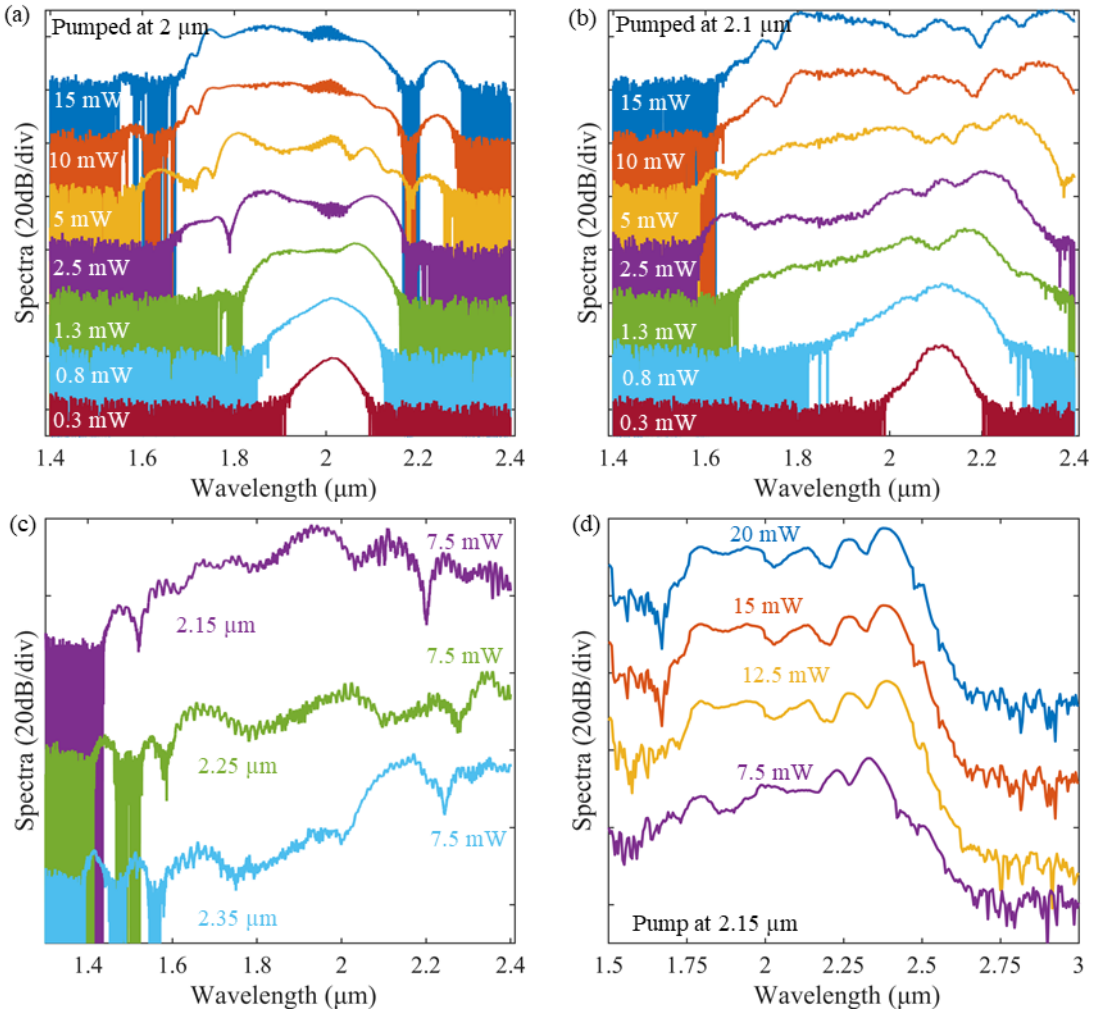

Figure 5.5 SCG spectra from a 2 µm core SCF. (a) Pumped at λ = 2 µm. (b) Pumped at λ = 2.1 µm. (c) Pumped at λ = 2.15 µm, λ = 2.25 µm and λ = 2.35 µm. (d) λ = 2.15 µm with different pump powers.

When pumping the fibre at longer wavelengths at 2.15 µm, 2.25 µm and 2.35 µm, the spectral broadening is easier to achieve as the pump wavelength is close to the ZDW, or in the anomalous dispersion region. The spectra extend further in the blue region, down to 1.4 µm, shown in Fig. 5.5 (c). The longer part of the spectra extends beyond 2.4 µm, which is the cut-off wavelength of the OSA. The full spectra were measured using the monochromator, but the long wavelength edge dropped sharply at around 2.6 – 2.7 µm for these longer pump wavelengths. For example, when using λ = 2.15 µm as the pump, the spectral evolution with increasing pump powers is shown in Fig. 5.5 (d). The spectra drop sharply at 2.7 µm and maintain the same profile when the pump power is increased beyond 12.5mW. The spectra pumped at 2.25 µm and 2.35 µm have same bandwidth from 1.4-2.6 µm. The spectral bandwidths measured in these results were not as broad as expected

and were also less broad than the previous results obtained in an amorphous SCF [20] with a similar fibre diameter. As none of these spectra extend beyond 2.7 µm, we suspect the reason could be absorption from the silica cladding, as it has an absorption peak around 2.7 µm, and/or from the interface layer. It is possible that this peak stops the SCG expanding further into mid-IR. The simulated cladding absorption values were obtained using the imaginary refractive index provided in Ref. [117]. However, these values are larger than in Ref. [118].

5.5.2 SCF with a 3 µm core diameter

Based on the assumption that the cladding absorption was the most likely limitation to generating SC bandwidths at the longer wavelengths. To reduce the cladding absorption, I simply tried another fibre (Material of core: O212, EL-CT Inc.) with a larger core size to reduce the mode interaction with the silica cladding. The fibre had a 3 µm core diameter and a length of 11 mm, the linear loss was measured to be ~2 dB/cm over the region 1.5-2.5 µm by the cutback method. The pump wavelength was chosen to be close to the ZDW near 2.4 µm, where the TPA is also negligible. The results are shown in Fig. 5.6. The broadest spectrum is from 1.4–3.5 µm at the -40 dB level, which is much broader than the previous results (The artefact is caused by the monochromator). The coupled average power to obtain this spectrum was double that used in the 2 µm core fibre Section 5.5.1, as the effective mode area is twice as large. These results indicate that the cladding absorption is not an insurmountable obstacle. The drawback of this SCG is the power level, as the core size is large and the pump is in normal dispersion regime, the SCG is dominated by SPM and requires a relative high pump power.

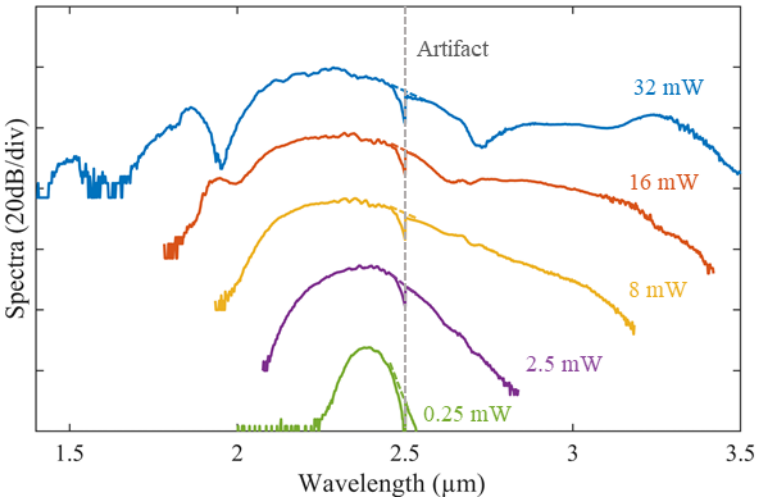

Figure 5.6 SCG in a straight 3 µm core diameter SCF pumped at 2.4 µm.

5.6 SCG in tapered SCF in the SWIR

There are a few disadvantages of using straight SCFs for SCG. First of all, the fibre core diameter is usually required to be very small to obtain a GVD parameter that facilitates efficient wavelength conversion. Small core SCFs have lower coupling efficiencies, which can lead to extra heating of the surrounding adhesive wax. When the wax melts, it can easily flow out of the capillary and block the fibre facet. Secondly, small core SCFs have higher cladding absorption. To reduce the absorption, one solution is to use shorter fibre lengths. However, limited by the sample preparation technique, it is very difficult to polish and mount a SCF with a few millimetres' length. To solve these problems, SCG in a SCF with a tapered profile was investigated.

As illustrated in Fig. 5.7, the fibre was designed to have an asymmetric taper profile. This profile was chosen as the large input core allowed for a high coupling efficiency, before the core was tapered down slowly to ensure tight confinement in the waist (with minimum mode coupling and radiation loss). The sharp up-taper was then employed at the output to reduce the interaction with the lossy cladding and maintain a high collection efficiency for all generated wavelengths. The principles behind this design are explained below.

Essentially, there are six parameters that can be controlled in the taper design: input core diameter D_{in}, waist diameter D_w, output core diameter D_{out}, down transition length L_{Td}, Waist length L_w and up transition length L_{Tu}. Here I simply summarise the design criteria that was established from these, which balance the nonlinear pulse dynamics with the overall losses of the fiber:

1. Large input/output cores to facilitate light coupling.

2. An input down-taper transition that is long enough for convenient sample. This section can also induce some initial spectral broadening, which helps to seed further nonlinear processes.

3. A tapered waist with a diameter that is in the anomalous dispersion region of the pump and a length that is long enough to induce a large nonlinear phase shift.

4. An up-taper transition at the output that is as short as possible to minimize absorption of the longer mid-infrared wavelengths.

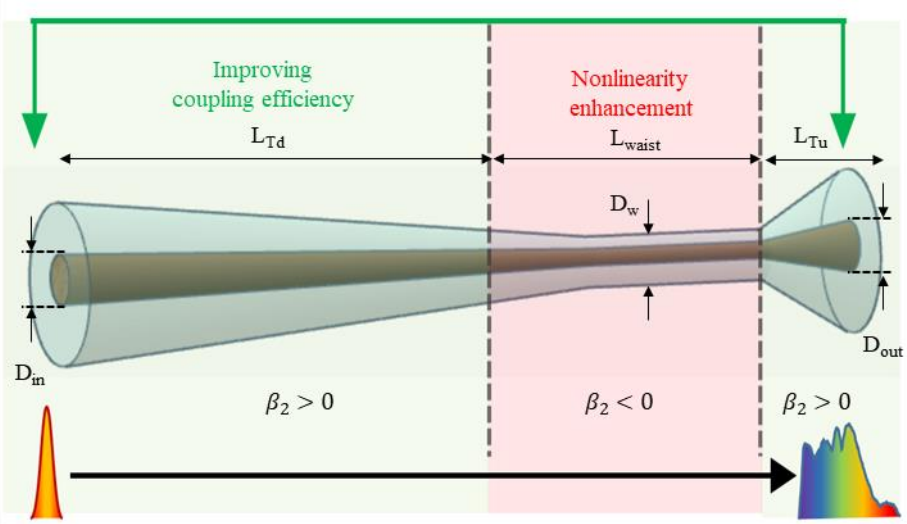

Figure 5.7 Schematic of the asymmetric taper design.

5.6.1 Design of the fibre profile

To test the improvement of the tapered design, a tapered SCF was fabricated with its profile following the design criteria. The pump wavelength is again chosen near 2.4 µm, where the nonlinearity of the fibre is relatively high and TPA can be neglected. The fibre profile is shown in Fig. 5.8 (a). The ZDW is also shown in the same figure with the dashed purple line indicating the location of the pump wavelength. The fibre core diameter changes from 4 µm to 1.5 µm and back to 7 µm at the output. At the designed pump wavelength, the first 3 mm of the fibre is in the normal dispersion region; from 3 mm to 10.5 mm of the fibre is in the anomalous dispersion region; and the last 4 mm of the fibre is again in the normal dispersion region.

As the fibre has a tapered profile, the cutback method cannot be used to determine the transmission characteristics. However, the absorption from the fibre can be estimated by excluding the coupling loss from the total insertion loss. The coupling loss includes the loss from the input and output lenses, radiation loss at the fibre input (mode mismatch), fibre-air interface reflection and light collection efficiency from the output lens. Among these terms, the loss from the lenses can be measured experimentally; the silicon/air reflection is usually assumed to be 1.5 dB per facet; the loss from the light collection is determined numerically by a commercial software (Lumerical Mode solution); the radiation loss at the fibre input can also be numerically estimated from the beam profile and the lens properties. To have a better estimation of the radiation loss at the fibre input, the beam profile from the OPO was measured using a mid-IR camera (Pyrocam IIIHR, Ophir Optronics), as shown in Fig. 5.8 (b). The transmission loss near the pump wavelength was estimated to be less than 5 dB/cm.

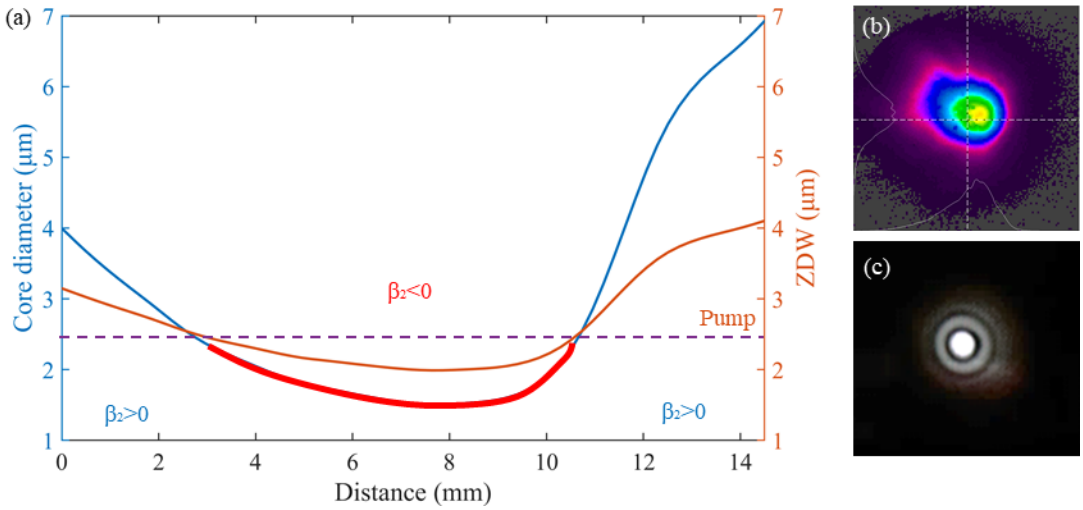

Figure 5.8 (a) Fibre profile with the corresponding ZDW when the pump wavelength is at 2.4 μm. (b) The beam profile from a mid-IR camera (Pyrocam IIIHR, Ophir Optronics). (c) The mode image from the output of the fibre in the CCD camera.

5.6.2 Experimental results

The experiment setup has been described in Section 5.4. The alignment was optimised for fundamental mode coupling and the output mode profile is shown in Fig. 5.8 (c). The SC spectra are shown in Fig. 5.9 (a). The broadest spectrum spans from 1.35 to 3 μm with only 4 mW coupled average power. It is much wider than the results in previous sections when using straight SCFs. When further increasing the pump power, the spectral bandwidth saturates, which could be due to cladding absorption and 3PA. The fibre was then pumped at different wavelengths across 2.2 μm–2.5 μm. The bandwidth of the obtained spectra are very similar, with only a small change in the spectral shape. Generally speaking, the spectra are flatter but narrower when pumped with shorter wavelengths, as a longer section of the fibre will be in the normal dispersion region and the spectrum will be more affected by SPM. The spectra pumped at longer wavelengths are wider but less flat, as the pump will be primarily in the anomalous dispersion regime, so that the continuum is dominated by pulse compression and DW emission. As the position of the DW is related to the third order dispersion of the fibre, a varying fibre profile can lead to multiple DWs generated at different wavelengths, resulting in an increased bandwidth of the spectrum [119], [120]. This is particularly obvious when pumping the fibre at 2.5 μm, as shown in Fig. 5.9 (b), where one DW occurs at 1.4 μm and another DW occurs at 1.6 μm. The position of DW can be roughly estimated by Eq (2.67) by assuming a constant fibre core diameter. For example, when pumping at 2.5 μm with 4 mW coupled average power (corresponds to 470 W coupled peak power), the soliton order is calculated using Eq (2.64) to be N=6.7 for an averaged 2 μm core, leading to a DW at 1.58 μm. This number is just between the two DWs measured, as a result of the varying fibre profile.

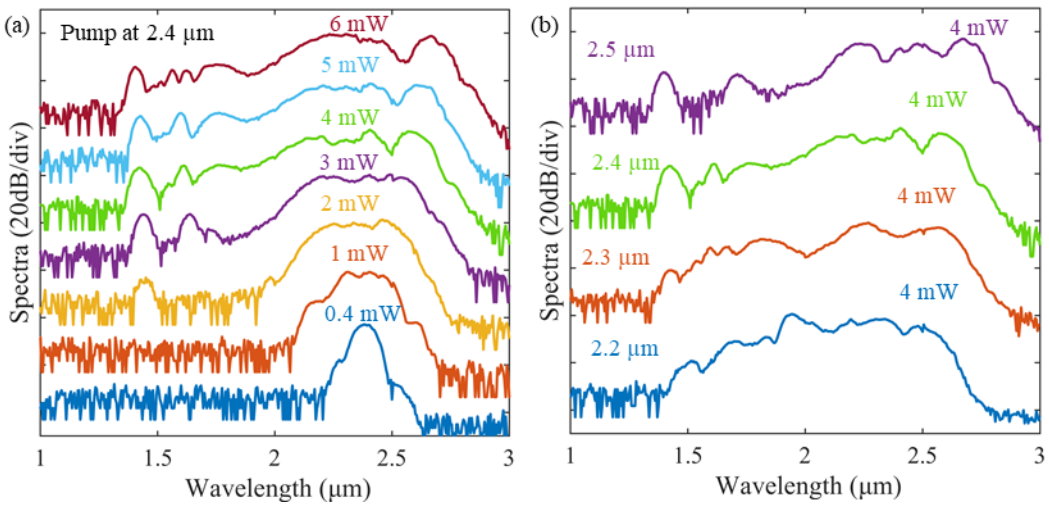

Figure 5.9 (a) SCG spectra generated in the tapered SCF, pumped at 2.4 μm with increasing coupled average power. (b) Wavelength tuning of the pump.

5.6.3 Numerical modelling analysis

To have a better understanding of the SC evolution in the tapered fibre, the pulse evolution in both frequency and time domains were studied numerically using the NLSE model. The parameters used in the modelling are shown in Table 5.2 and Fig. 5.10. The spectral and temporal pulse evolution are shown in Fig. 5.11 (a) and (b). It can be seen that the SCG process can be divided into three parts by the sign of GVD parameters. In the first part of the fibre from 0 to 2.5 mm, the pump pulse propagates in the down transition of the fibre. In this section, the core size is large and β_2 is positive, the pulse only has some initial spectral broadening through SPM. The peak power of the pulse also decreases due to the dispersion and loss. In the second part of the fibre from 2.5 mm to 11 mm, due to the negative β_2 and smaller fibre core, the pulse compresses and its intensity rises dramatically, which triggers soliton fission and DW emission. In the third part of the fibre from 11 mm to the end, the pump enters the normal dispersion again and the light intensity is greatly reduced. As a result, no nonlinear interaction happens in this section and the spectrum remains unchanged.

Table 5.2. SCG simulation parameters

Parameter	Symbol	Value (unit)
Pump wavelength	λ	2.4 μm
Linear loss	α_l	5 dB/cm at pump wavelength
Kerr effect coefficient	n_2	6.0×10^{-18} m^2/W
Pulse width	T_{FWHM}	100 fs (hyperbolic secant)
Carrier life time	τ	10 ns
FCA parameter	σ	0.55×10^{-21} m^2 from Ref. [121]
3PA coefficient	β_{3PA}	7×10^{-27} m^3/W^2 from Ref. [108], [122]
GVD parameter	β_2	Shown in Fig. 5.10 (a)

3rd order dispersion	β_3	Shown in Fig. 5.10 (b)
Effective mode area	A_{eff}	Shown in Fig. 5.10 (b)

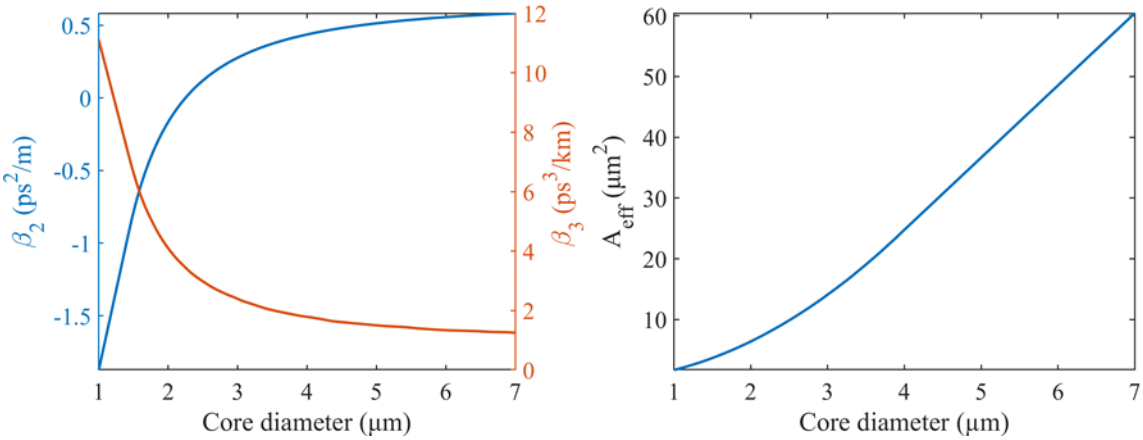

Figure 5.10 (a) Dispersion properties of the tapered SCF at the pump wavelength of λ = 2.4 μm. (b) Effective mode area of the tapered SCF at the pump wavelength of λ = 2.4 μm.

To investigate the wavelength distribution of the SC in the time domain, SCG in this fibre was also studied using numerical spectrograms, shown in Fig. 5.12. At z = 6 mm, the spectral bandwidth is at the broadest position (also as seen in Fig. 5.11 (a)). The pulse is temporally compressed, and its energy is concentrated. After this point, the SC gradually stretches temporally due to dispersion, which weakens the frequency mixing, as shown in Fig. 5.12 (b). The output SC has a ~2 ps pulse duration. As the broadest position of the spectral was produced in the middle of the fibre, the fibre section from 6 mm to 14 mm does not help to extend the spectrum further but purely introduces additional losses. This indicates that the fibre profile could be further optimised by using shorter fibre length.

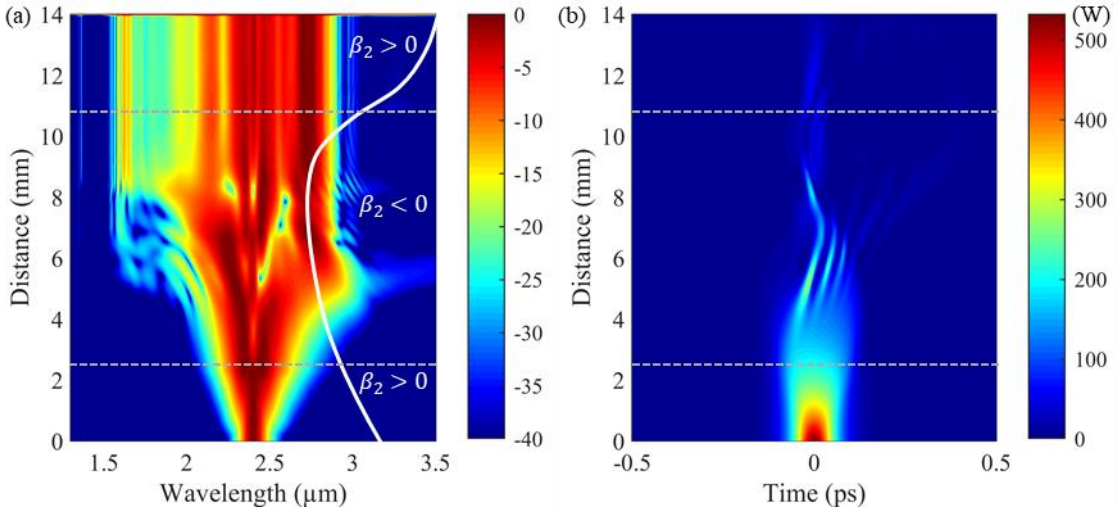

Figure 5.11 NLSE simulation of the SCG in the tapered SCF with 520 W pulse peak power. The white dashed lines divide the fibre by sign of dispersion at pump wavelength. (a) Spectral evolution along fibre. (b) Pulse propagation along the fibre.

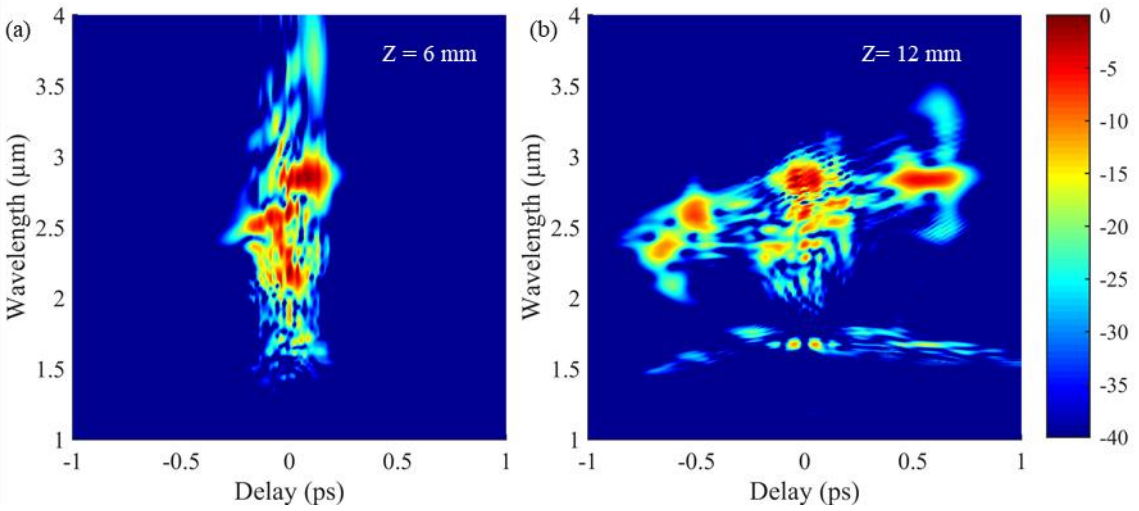

Figure 5.12. Spectrogram of the SCG at different fibre locations. (a) At 6 mm along the fibre. (b) At 12 mm along the fibre.

5.7 SCG in the tapered SCF in MWIR

5.7.1 Design of fibre profile

To further extend the spectrum to longer wavelengths in the MWIR band, the pump wavelength was moved to 3 μm. To determine the best tapered fibre profile, I used extensive modelling of the NLSE to establish the design that was likely to produce the broadest SC. To simplify the problem, modelling of each section was initially conducted independently in three steps. Firstly, I choose the waist diameter and length. The waist diameter was targeted to be ~3 μm such that it is close to the ZDW, in the anomalous dispersion regime, and yet still has relatively low cladding losses. The waist length was then determined from results of the NLSE simulation. In the simulation, a straight fibre with a core diameter of 2.8 μm was used. The pump peak power was set to be 1.5 kW. This power corresponds to an intensity of 40 GW/cm^2 in the fibre waist, which has a moderate nonlinear absorption in the region of the pump wavelength [122]. The spectral evolution is plotted in Fig. 5.13 (a). From this I targeted a length of ~2 mm as this corresponds to the shortest length to obtain maximum spectral broadening. The second step was to determine the fibre down transition. The input diameter was set to be 10 μm to allow for easy alignment and efficient coupling. The down transition length was determined numerically. Fig. 5.13 (b) shows SC spectra generated in down taper lengths of 0, 2.5, and 5 mm. It is clear from the figure that the 5 mm down transition produces the broadest spectrum with the longest red spectral edge. Longer lengths do not offer any additional broadening as the losses will also increase. The final step was to design the up transition. The output core diameter was set to be 10 μm for efficient light collection for the longer

wavelengths and the up-transition length was chosen to be as short as possible to minimize the cladding loss for the long wavelengths.

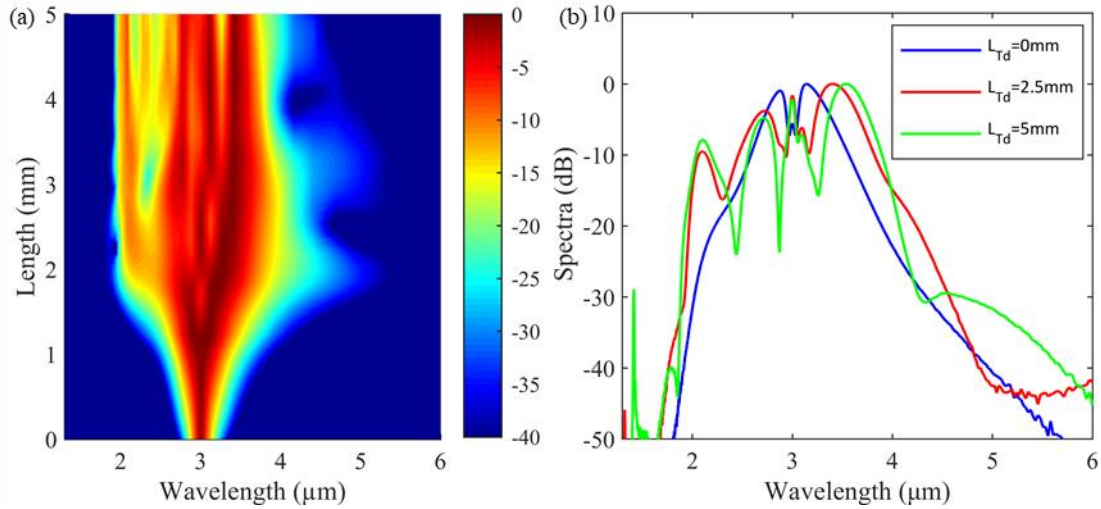

Figure 5.13 (a) Simulation of SCG evolution in a straight SCF with a 2.8 μm core diameter and 1.5 kW coupled pump power at λ = 3 μm. (b) Simulated SCG spectra with different down taper transition lengths.

With the target fibre profile parameters determined, I fabricated another tapered SCF with the technique described in Chapter 3. The measured fibre profile is shown in Fig. 5.14 (a) with the ZDW plotted in the same graph for comparison. The pump wavelength is indicated by the dashed purple line. Compared with the fibre profile in Section 5.5, this fibre is only 8 mm long and only a 2 mm fibre section from 5.2 mm to 7.2 mm is in the anomalous dispersion region. The up-transition length is also much shorter, less than 1 mm. The overall fibre diameter is much larger, which means the cladding absorption at longer wavelengths will be much smaller.

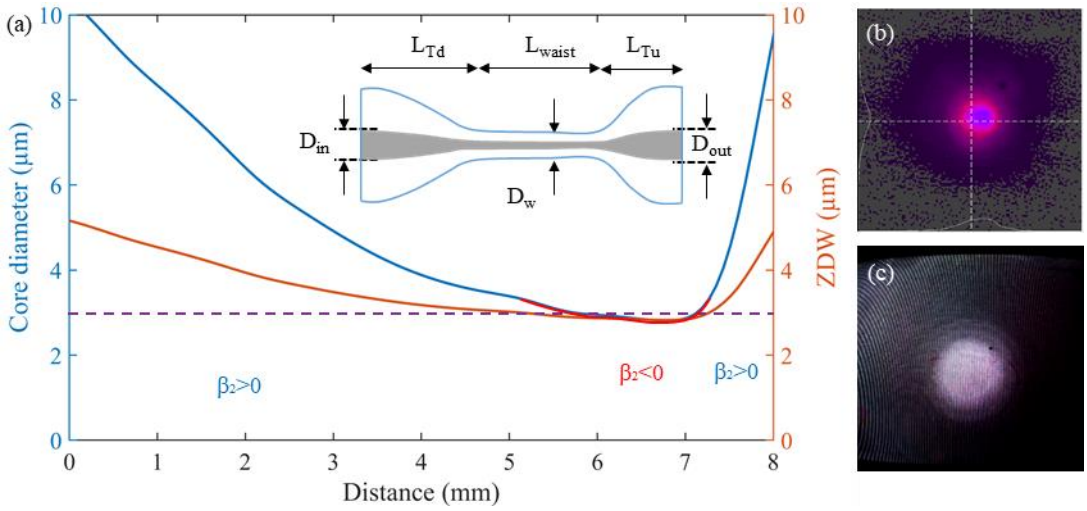

Figure 5.14 (a) Fibre profile with the corresponding ZDW when pumped at 3 μm. Inset is the schematic of the fibre. (b) The beam profile from a mid-IR camera (Pyrocam IIIHR,

Ophir Optronics). (c) The mode image of the SCG from the output of the fibre in the CCD camera.

5.7.2 Mode coupling and transmission

The experimental setup has been described in Section 5.4. As the input core diameter is large, care must be taken to select a proper lens to ensure most of the coupled light is in the fundamental mode. The input beam from the OPO was measured by a mid-IR camera (Pyrocam IIIHR, Ophir Optronics), as shown in Fig. 5.14 (b). The beam radius was measured to be ~1.5 mm. To find the proper lens for input coupling, the focused beam size was calculated numerically using different lenses. Then the focused beam size (assumed to be Gaussian distribution) and its overlap with the guided modes of the SCF were calculated numerically for the pump wavelength of 3 µm. Fig. 5.15 (a) shows the mode overlap between the incoming beam and fibre modes from a 10 µm core diameter SCF. Most of the power is coupled into the LP_{01} and LP_{02} modes. The fundamental mode percentage to the total coupled power is over 90% when the incoming beam radius is between 2.5 µm to 4.5 µm, as shown in Fig. 5.15 (b). Based on these criteria, a black diamond lens with NA = 0.56 was used for the input coupling, with a calculated focused beam radius of ~2.9 µm. Thus, we expect that for this configuration most of the coupled power is in the fundamental mode.

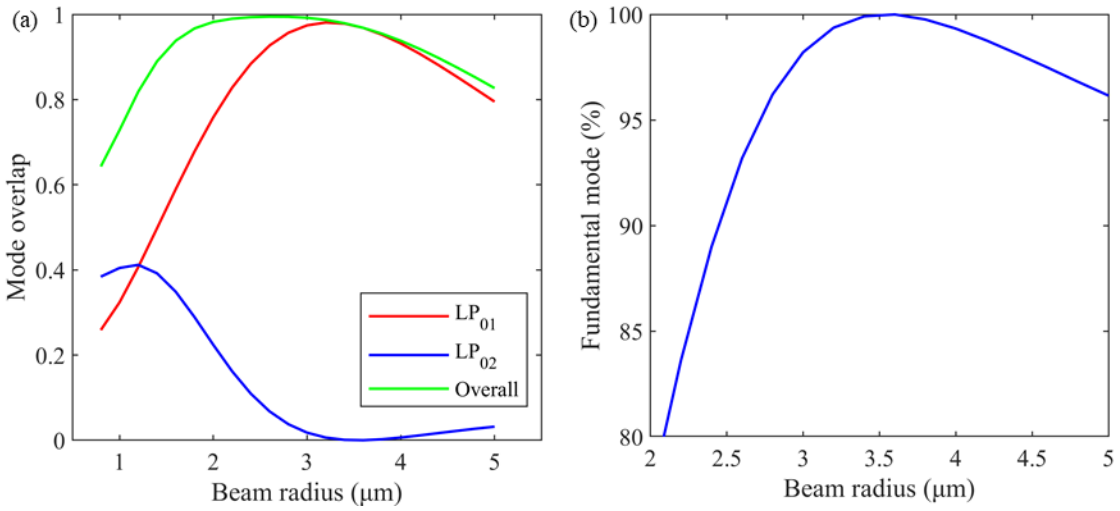

Figure 5.15 (a) Mode overlap of a Gaussian beam and the two lowest order LP_{0m} modes in the SCF with a 10 µm core diameter at a 3 µm pump wavelength. (b) Percentage of the fundamental mode for different input beam waist radi.

To characterise the transmission properties of this tapered SCF, the insertion loss of the device was measured for OPO wavelengths between 1.7-3.7 µm, using the lowest power setting to minimise the effects of nonlinear absorption. At the pump wavelength of 3 µm, the total insertion loss is only 7.3 dB. The fibre insertion loss and estimated loss per unit length are shown in Fig. 5.16. The large

error bars are due to the uncertainty of the coupling loss. The average propagation losses are extracted to range between 0.2 dB/cm up to 3 dB/cm over this wavelength region. This is comparable to the lowest values reported in planar silicon waveguides over a similar wavelength regime [12], [13].

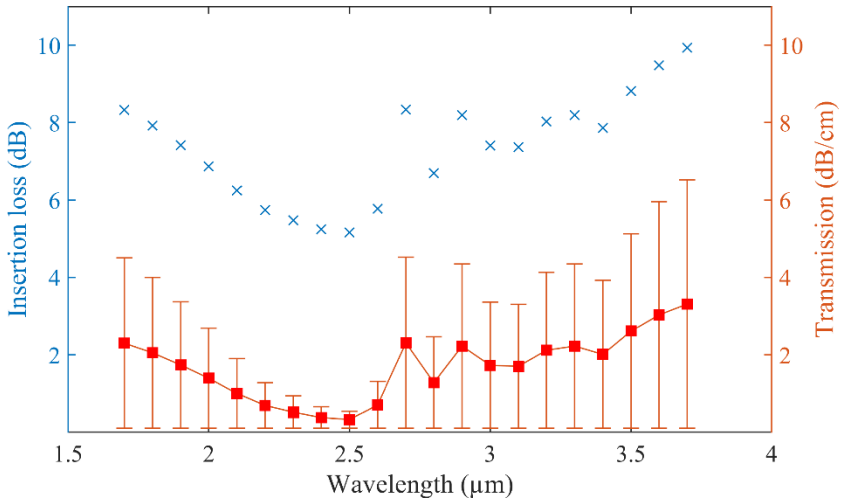

Figure 5.16 Transmission properties of the tapered SCF at different wavelengths. The error bars are from uncertainties of the coupling efficiency.

5.7.3 Experimental results

The fibre was pumped at 3 μm with various input powers. The output SC spectra are shown in Fig. 5.17 (a). The coupled average pump powers increase from 0.4 to 10.8 mW. The SC bandwidth and the power used are shown in Table 5.3. The spectrum spans over one octave from 1.94 μm – 3.96 μm with only 4.17 mW coupled average power. This is comparable to the SC spectra in Section 5.6 show in Fig. 5.9 (a), where the spectrum spanned 1.15 octaves from 1.35 μm to 3 μm with a similar coupled average power. For the highest coupled average power at 10.8 mW, the spectrum spans 1.72 octaves from 1.62 to 5.34 μm at the -40 dB level, which is much wider than the SC in Section 5.5, extending well beyond the absorption edge of the silica cladding, thanks to the specially designed tapered structure. Moreover, the long wavelength signals (>5.5 μm) in the high-power spectrum of Fig. 5.17 (a) are still above the noise level, however, we were not able to measure beyond this point due to the limited detector sensitivity. Owing to the free space coupling arrangement, the atmospheric CO_2 absorption dip at 4.25 μm can be clearly observed in all spectra when the coupled input average power is above 6 mW. As the pump is in the normal dispersion regime for most of the fibre sections, the spectral broadening is dominated by SPM followed by soliton fission and DW emission, as evident from the evolution of the spectral profile and as labelled in the top spectrum (SPM SB1, SB2 at λ = 2.67 μm and λ = 3.4 μm and DW at λ = 1.8 μm) in Fig. 5.17

(a). Using Eq (2.67), the calculated DW position is 1.8-2 µm corresponds to the core diameter 2.9-3.1 µm in the waist region of the taper.

Fig. 5.17 (b) shows the results from tuning the pump wavelength for four different wavelengths near 3 µm. For comparison, all the spectra have been recorded at their broadest bandwidth and the corresponding coupled average pump power is as labelled. As expected, the maximum spectral bandwidth is obtained for the optimum pump wavelength at 3 µm. In particular, when pumping at 2.7 µm in the normal dispersion regime the spectral broadening is mainly induced by SPM, so that it exhibits the smallest broadening. These results again highlight the important role dispersion plays to enhance the broadening, with the broadest spectrum being obtained when the phase matching conditions for DW emission are met.

Table 5.3 MWIR SC results

Coupled Average Power (mW)	Coupled Peak Power (kW)	Spectral Range (µm)	Octaves
10.8	1.19	1.62 - 5.34	1.72
8.75	0.96	1.66 - 4.51	1.44
6.25	0.69	1.68 - 4.45	1.41
4.17	0.46	1.94 - 3.96	1.03
2.08	0.23	2.48 - 3.59	0.53
0.41	0.045	2.62 - 3.37	0.36

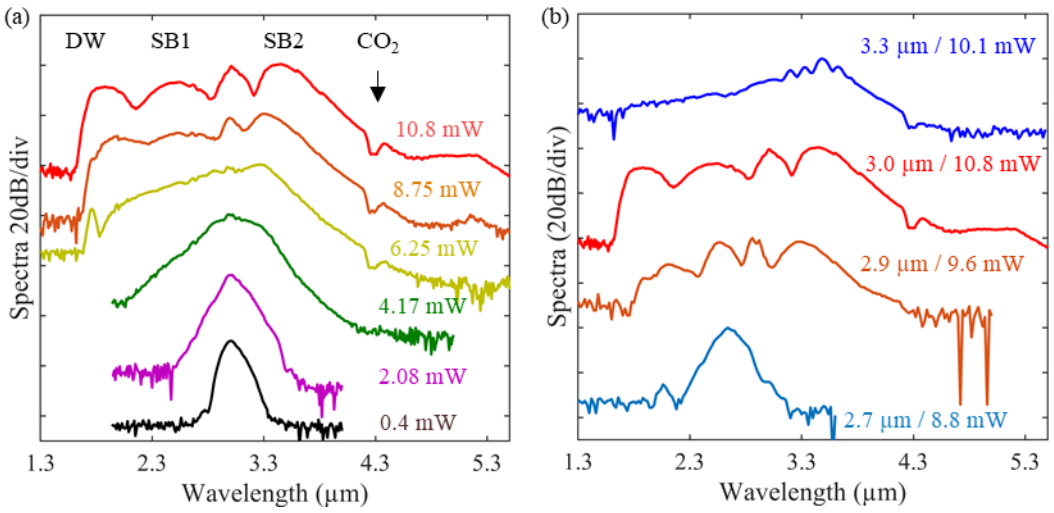

Figure 5.17 (a) Experimental spectral broadening as a function of coupled average input power. The wavelength converted peaks associated with FWM (FWM sidebands SB1 and SB2) and DW emission are labelled in the top spectrum. Black arrow shows the CO2 absorption dip. (b) Comparison of SC generation with different pump wavelengths.

Fig. 5.18 shows the converted SC power at the output fibre facet for increasing coupled average (peak) power up to 10.8 mW (1.19 kW). The converted SC powers are back calculated using the

values measured on the detector by excluding the coupling loss at the output facet. The input/output powers measured on the detector were 26 mW/3.8 mW. The transmission loss from the front/back lens (Molded IR Aspheric Lenses, Thorlabs) are 1 dB each. Assuming the reflectivity of silicon/air interface is 1.5 dB and mode mismatch at the front facet is 1.3 dB, the coupled average power can be then calculated to be 10.8 mW. The converted in-fibre SC power can be calculated to be 6.8 mW by excluding the 1.5 dB output facet reflection and 1 dB lens loss, leading to a power conversion efficiency as high as ~62%. This is the highest power conversion efficiency reported in any Group IV semiconductor platform, as shown in Table 5.1. The converted SC power reached a value of 6.6 mW for 10.8 mW coupled average power, resulting a spectrally bright SC with an average power spectral density of $PSD_{average}$= 2 μW/nm. The total nonlinear loss introduced in the SCF is only 1-2 dB due to the short taper waist length and low pump power. When combined with the high output coupling efficiency, a SC power of ~4 mW is obtained outside the fibre. This is a significant improvement over previous mid-IR SC demonstrations in silicon waveguides, which have been limited to out-coupled powers less than 1 mW [13]. As the pump power (21 mW average power at the fibre facet) is far below the damage threshold of crystalline silicon, stable operation is expected and the tapered SCF used in this experiment exhibited no measurable change in transmission over several months of experiments. Higher pump power was not used, as we found that when the coupled average power was further increased up to 14.5 mW, the spectrum did not get broader and the output power gradually saturated at ~4 mW due to 3PA. However, in this work, the maximum average power that was tested on a tapered SCF was ~600 mW, which further confirmed that the tapered SCF device is resistant to relatively high powers.

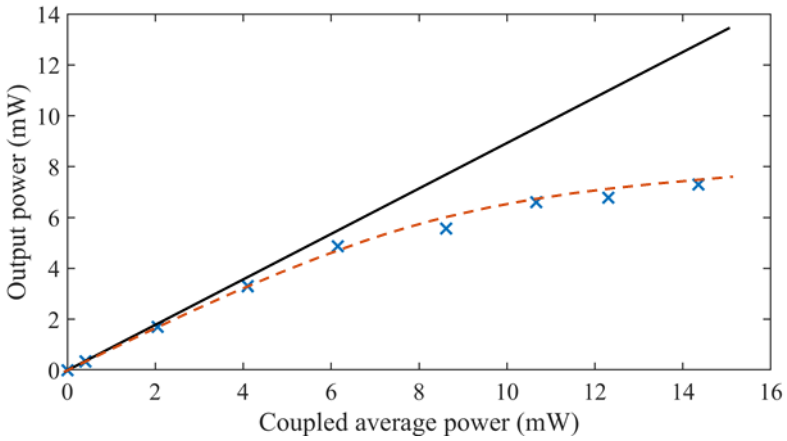

Figure 5.18 Output SC power versus coupled power, average power (bottom) and peak power (top), for the tapered SCF. Black line indicates linear loss.

5.7.4 Numerical analysis

The pulse evolution in frequency and time domain were studied numerically using the NLSE. The parameters used in the simulations are provided in Table 5.4 and Fig. 5.19 (a) and (b). The spectral evolution with increasing pump powers are shown in Fig. 5.19 (c). Compared with the experimental results in Fig. 5.17 (a), the stimulated spectra show reasonable agreement with the measured results, not only in terms of the bandwidth, but also their spectral features. The slight difference between the simulations and experiments arises in the position of the DW, where there is a mismatch of ~0.2 μm. This discrepancy could be caused by uncertainties in the higher order dispersion values used in the simulations, principally due to the difficulty in precisely mapping the core diameter variations along the taper profile and waist. In addition, the discrete peaks on the short wavelength side are not visible in the experimental spectra, which is artefact from the simulation.

Table 5.4. SCG simulation parameters

Parameter	Symbol	Value (unit)
Pump wavelength	λ	3 μm
Linear loss	α_l	Wavelength dependent losses shown in Section 5.2
Kerr effect coefficient	n_2	$3.0 \times 10^{-18}\ \mathrm{m^2/W}$
Pulse width	T_{FWHM}	100 fs (hyperbolic secant)
Carrier life time	τ	10 ns
FCA parameter	σ	$2.9 \times 10^{-21}\ \mathrm{m^2}$ from Ref. [121]
3PA coefficient	β_{3PA}	$2 \times 10^{-27}\ \mathrm{m^3/W^2}$ from Ref. [108], [122]
GVD parameter	β_2	Shown in Fig. 5.19 (a)
3rd order dispersion	β_3	Shown in Fig. 5.19 (a)
Effective mode area	A_{eff}	Shown in Fig. 5.19 (b)

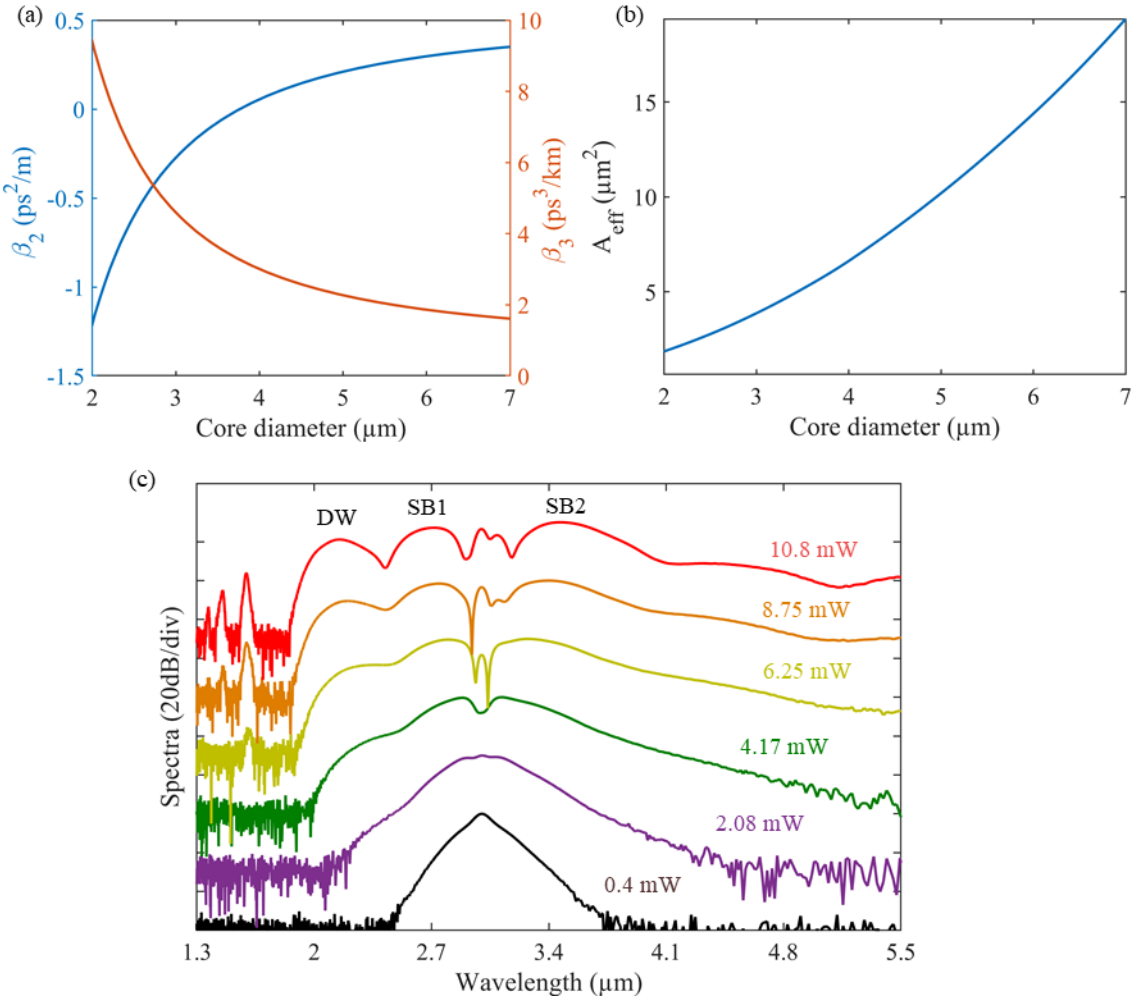

Figure 5.19 (a) Dispersion properties of the tapered SCF at the pump wavelength of λ = 3 μm. (b) Effective mode area of the tapered SCF at the pump wavelength of λ = 3 μm. (c) Numerical simulation results for SC spectra generated in the tapered SCF when pumped at 3 μm.

Fig. 5.20 (a) and (b) show the simulated spectral and temporal evolution along the SCF for the maximum coupled peak power of 1.19 kW, clearly illustrating the complete spectral dynamics. Similar to the SCG in tapered SCF for SWIR, the whole process is divided into three sections in the fibre. In the first section, between 0 and 4 mm, the pump pulse propagates in the normal dispersion regime and exhibits modest broadening due to SPM. In the second section from 4 – 7 mm, the core diameter continues to reduce, and the pump pulses access the anomalous dispersion region with a larger peak intensity. This forms high order soliton which eventually leads to compression, break-up and DW emission to produce a broadband SC spectrum. It can be seen that most of the SCG happens in the last 2 mm of the fibre. This is useful as it greatly reduces the cladding loss for longer wavelengths. The final section incorporates the sharp, 1 mm long, up-taper during which there is no significant absorption of the spectral components. The large output fibre core allows the light to be collected out of the fibre with minimal loss.

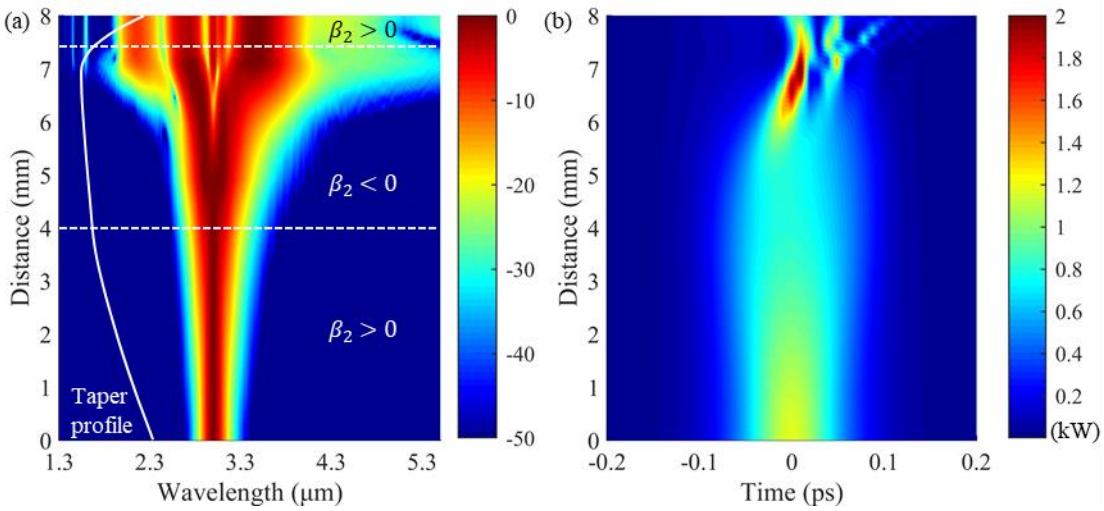

Figure 5.20 (a) Simulated spectral evolution of the SC along the tapered fibre on a normalised log scale. (b) Simulated temporal evolution of the SC along the tapered fibre for the maximum coupled peak power of 1.19 kW. The colour bar shows the peak power in kW.

To investigate the wavelength distribution of the SC in the time domain, the SCG process is plotted using spectrograms, shown in Fig. 5.21 (a). The SPM sidebands SB1, SB2 and the DW can be clearly distinguished in the figure when z = 8 mm. Fig. 5.21 (b) shows the output pulse in the time domain compared with the input pulse before the fibre. It can be seen that the output SC consists of many sub-pulses, with two of them having a peak power as high as ~1 kW. In fact, the peak power of the pulse in the fibre always maintains a high level, as shown in Fig. 5.20 (a). The maximum peak power of the propagating pulse is as high as 2 kW at z = 7 mm of the fibre. This is one of the reasons for the high nonlinear frequency conversion efficiency in this particular fibre design.

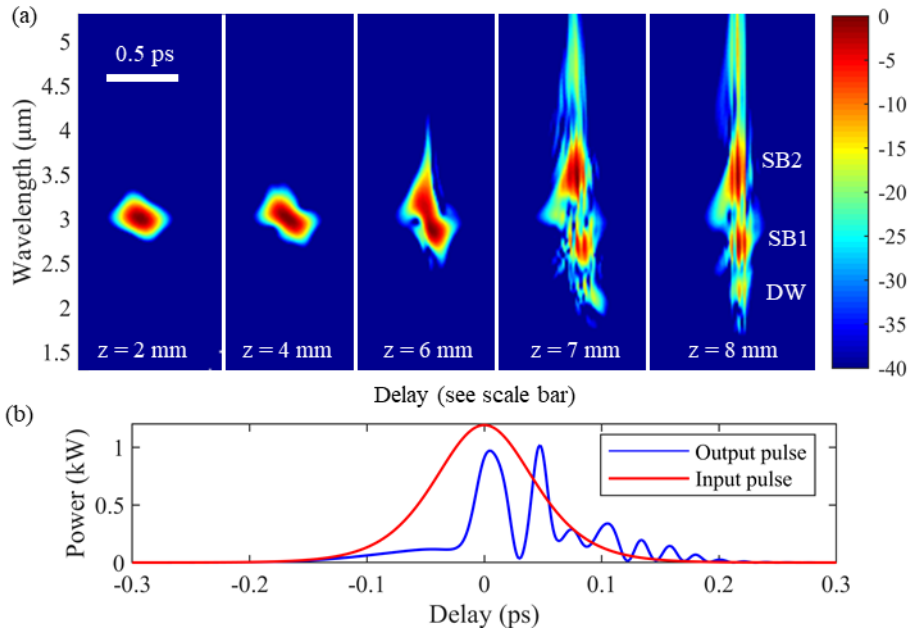

Figure 5.21 (a) Spectrogram of the SCG at different fibre locations. The scale of the horizontal axis is shown as scale bar. (b) Input and output SCG pulses in the time domain.

5.7.5 Coherence property

For applications such as spectroscopy and optical frequency comb metrology, it is important to ensure the generated SC can preserve the coherence of the pump laser. Unlike SC sources that make use of picosecond or longer pump pulses, where the broad spectral bandwidth is generated via amplification of background noise (modulation instability) [123], by relying largely on SPM and FWM, the SCG in Fig. 5.17 is expected to have maintained good coherence, as reported in Refs. [112], [116]. Coherence of the SC can be calculated by the equation in [123]:

$$|g_{12}(\lambda)| = \left| \frac{\langle A_1^*(\lambda) A_2(\lambda) \rangle}{\sqrt{\langle |A_1(\lambda)|^2 \rangle \langle |A_2(\lambda)|^2 \rangle}} \right|, \quad (5.3)$$

where A_1 and A_2 are the electric field amplitudes of two independent SC output. g_{12} is the complex degree of first-order coherence and the angle bracket represents the ensemble average over all independently generated SC pairs. In this work, the coherence is calculated by applying 100 pairs of individual SC output with this equation, described in Ref. [114]. The laser source (OPO) used in this work has a 5% intensity noise with 30 dB level signal to noise ratio. To model the quantum noise from the input pulses, each of these spectra is generated by incorporating 5% intensity noise together with 30 dB level signal to noise ratio to the input pulse envelop [114]. As shown in Fig. 5.22, the SC is highly coherent (>0.9) and close to unity over its entire bandwidth. A ±5% pump intensity difference does not affect the overall spectral shape. This is in good agreement with the predictions that SC spectra pumped by femtosecond pulses will largely preserve the coherence of the pump source [124]. The coherence could be further improved to approach unity if pumped by a more stable laser source (e.g., a mode-locked fibre laser [125]) with negligible power fluctuations. For an example, when using mode-locked laser with power fluctuation of 1.5% [126], the coherence of the whole spectrum is almost 1. This indicates that the coherence of the SC mainly depends on the stability of the pump source.

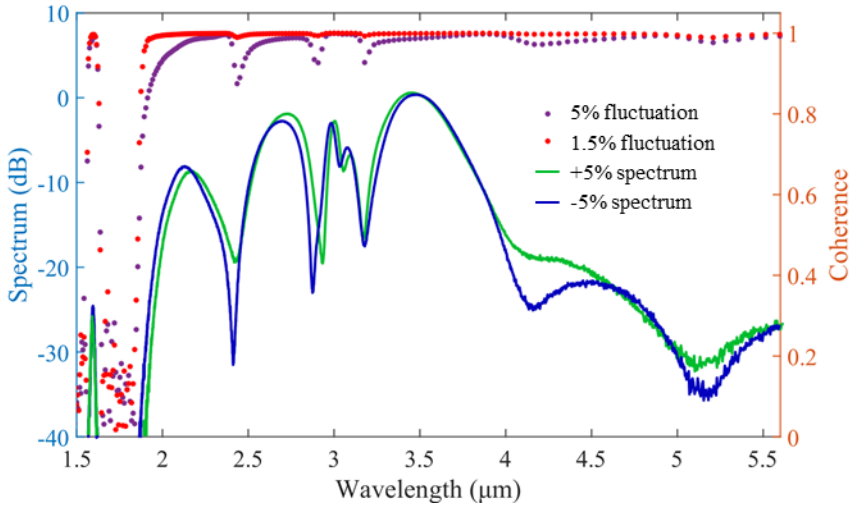

Figure 5.22 Simulated coherence with quantum noise and intensity fluctuations (5% in purple and 1.3% in red) together with the simulated SC spectra with + 5% and -5% differences of the highest input power in Fig. 5.19 (c).

5.7.6 Spectral optimisation

The experimental results have shown that the tapered SCF platform can generate SC spectra extending over 55% of the transparency window of the silicon core material. In order to study the ultimate limit of the SC bandwidth, further optimisation of the taper design was numerically investigated. To simplify the problem, the wavelength is fixed at 3 μm and the SCG is optimised by changing the fibre profile and pump power. The generated spectra are compared in terms of spectral bandwidth. I define spectral bandwidth factor as $\Gamma = \int S(\omega) d\omega$, where $S(\omega) = \frac{|A(\omega)|^2}{max(|A(\omega)|^2)}$ is the normalised SCG spectrum. This factor is related to both spectral bandwidth and flatness. Larger Γ corresponds to wider and flatter spectrum. There are 7 variables in this optimisation process (pump power, D_{in}, D_w, D_{out}, L_{Td}, L_w and L_{Tu}) to find the maximum value of Γ. To simply the problem, the fibre profile is created based on a simple model described in Ref. [127]. By calculating the SCG spectra with combinations of these 7 variables, the best spectrum can be found when Γ is at maximum. However, this optimisation process can be time consuming as the computational time exponentially grows with number of variables and variable step size. As a result, the optimisation process requires manual assistance to set proper variable range. Using this method, the fibre profile that produced the best spectrum is shown in Fig. 5.23 (a) together with the corresponding SC in Fig. 5.23 (b). We find that when the fibre is pumped with an average input power of 27.2 mW (3 kW peak power), the spectrum spans from 2 μm to beyond 8 μm at the 20 dB level.

The SC evolution in this tapered design is shown in Fig. 5.24. The longer wavelength components (beyond 6 µm) are, in fact, generated in the up-transition region in the last millimeter of the fibre. Although this is beneficial for minimizing the long wavelength interaction with the cladding, it does mean that the broadening is very sensitive to variations in the output taper diameter as higher order dispersion plays a key role in the frequency conversion. Nevertheless, this simulation indicates that the tapered SCF platform has the potential to produce SC spectrum that covers the entire silicon transparency window, even with an absorptive silica cladding.

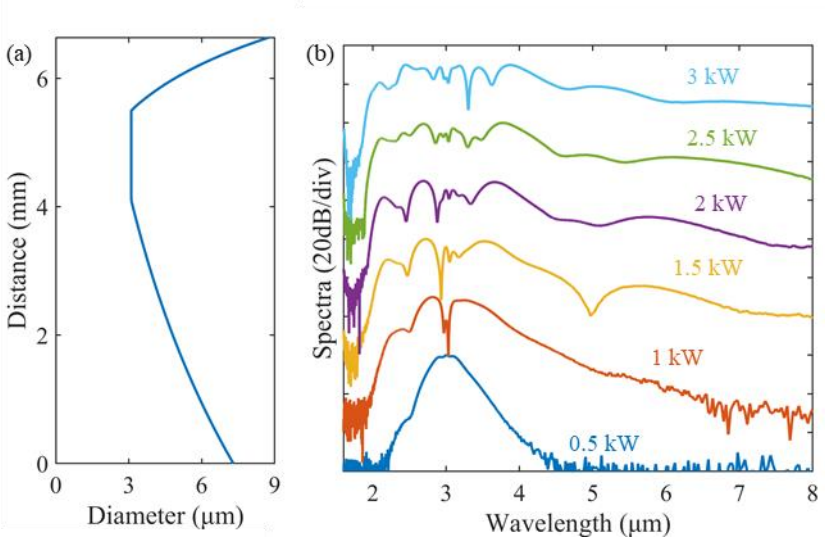

Figure 5.23 (a) Tapered SCF profile. (b) Simulated SC spectra with different coupled peak powers.

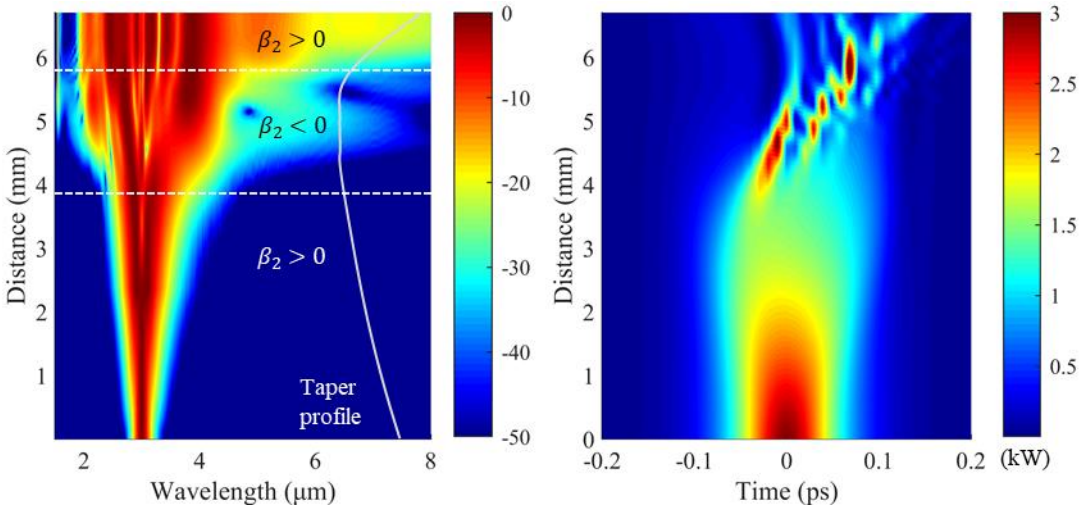

Figure 5.24 Simulation result for optimised taper profile. (a) Spectra evolution along the SCF. (b) Pulse evolution along the SCF.

5.8 Conclusion

In summary, this chapter has presented results on femtosecond pumped SCG in tapered SCFs. The GVD profiles and transmission windows of the tapered SCFs make them a suitable platform for

broadband SCG in the infrared region. SCG in straight and tapered SCFs were studied, both experimentally and numerically. Tapered fibre profiles can greatly improve the SC bandwidth and efficiency. A highly coherent SC spanning 1.74 octaves has been generated from 1.6-5.3 μm, which is the broadest SC reported in a silicon core/silica clad waveguide. Numerical modelling suggests that broader SC can be obtained by further optimising the fibre profile. The source also has high brightness and coherence, making it readily suitable for applications in mid-IR communications, spectroscopy and imaging.

Chapter 6 High index fiber integration

6.1 Introduction

In this chapter, we report the fabrication of tapered SCFs with inverse taper couplers that enable efficient optical coupling into the silicon core, as well as their robust integration to SMFs by splicing. Different couplers for integration of SCF nanospike structures and SMFs were investigated. The best coupler was found to be when both fibres were tapered. A proof-of-concept 30 µm cladding diameter SMF-SCF device was fabricated. The optical transmission property of this device was studied experimentally via the cutback measurement and numerically via FEM simulations. This integration design was found to be efficient and robust which will help to overcome significant barriers for all-fiber nonlinear photonics and optoelectronics.

6.2 Splicing of SCF nanospike to SMF

The inverse taper coupler has been especially designed for small core high index waveguides. It offers the capability to provide efficient coupling over a wide bandwidth [17]. The key idea behind this approach is to gradually decrease the SCF core to a small dimension at the facet, so the guided mode spreads out to better match both the area and the effective index of the incoming mode. The schematic diagram of the device is shown in Fig. 6.1 (a). Numerical simulations (Lumerical mode solution) were used to study the modal behavior in the SCF with nanoscale core sizes. Fig. 6.1 (b) shows the mode fields of the SCF with core diameter decreasing from 600 nm to 200 nm at λ = 1.55 µm. Due to strong light confinement, the mode is tightly confined in the core even when the core diameter is 300 nm. When the core diameter is smaller than 300 nm, light starts to spread out of the fibre core and propagates as evanescent field with its energy centered in the middle of the fibre. We define the criteria for mode spreading when less than 50 % of the power is confined in of the core. Thus, the core diameter of a SCF should be at most one fifth of the wavelength. Fig. 6.1 (c) shows the transmission between a SCF and a SMF as a function of tip diameter (calculated by Mr Joseph Campling). The optimum tip size is around 200nm. This means that theoretically if the tip size is 200 nm, the mode coupling at the tip can be as high as -0.5 dB.

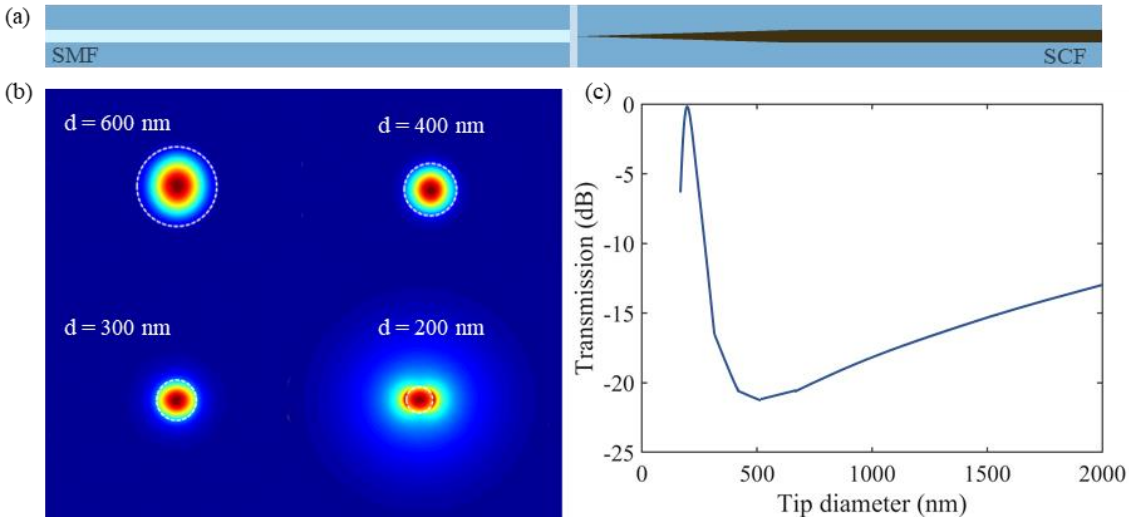

Figure 6.1 (a) Schematic of SMF integration with the SCF nanospike. (b) Fundamental mode profile in a SCF with different core diameters at λ = 1.55 µm. (c) Mode overlap between silicon tip and SMF as a function of tip diameter at λ = 1.55 µm.

6.2.1 Fabrication

The fabrication process to produce inverse tapers in SCFs can be achieved by properly setting the tapering parameters, such as heating power, tapering ratio, and tapering length. As discussed in Chapter 3, the core continuity can be affected by the drawing power and fibre dimensions. When the tapering ratio is relatively large, at the position between the down transition and waist of a tapered SCF, a small overshoot will occur. This overshoot leads to a local minimum of the fibre outer diameter. When the heating is slightly higher than normal the core in the overshoot area can become so small that it vanishes and form a silicon “nanospike”. Fig. 6.2 (a) and (b) show microscope and SEM images of a tapered SCF with a nanospike region. It can be seen that the tip is smooth, with a size that gradually vanishes. The SEM image was taken by chemically etching the silica cladding away using hydrofluoric acid (Work by Dr. Yohann Franz). The sharpness of the spike depends on the tapering parameters.

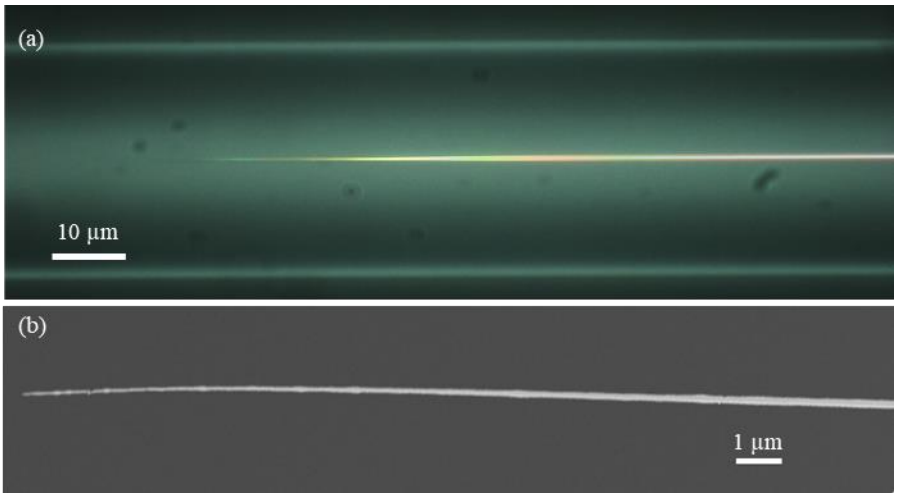

Figure 6.2 (a) Microscope image of a SCF with nanospike. The rainbow colour on the nanospike indicates the smoothness of its tip. (b) SEM image of the naked nanospike with the silica cladding etched.

As the final goal is to integrate the SCF with a nanospike coupler to SMF, the cladding diameter of the tapered SCF needs to be close to that of SMF (125 µm). The as-drawn fibre available has a ~120 µm diameter cladding and ~12 µm core diameter (core material D429, EL-CAT Inc.), thus, they need to be inserted into a thick silica tube before tapering to increase the cladding thickness, as shown in Fig. 6.3 (a). After the tapering process, the fibre is cleaved carefully using a cleaver (FC-6S Optical Fiber Cleaver) at the end of the nanospike under a microscope. Usually, the distance from the cleaved facet to the tip end should be kept within the Rayleigh length of the mode coming out of the SMF, which is estimated to be 60 µm at 1.55 µm. Otherwise, the light will spread into the cladding before entering the SCF nanospike. As the silicon tip is very small, it is extremely sensitive to heating, which makes the splicing process rather difficult with a commercial splicer, as the lowest power (1/16 of the power used for standard SMF fusion) with shortest arc duration (0.01 second) available can still damage the spike. To overcome this problem, we use the more flexible Vytran tapering rig to splice these fibres using a “cold splicing” method. Firstly, the SMF and the tip of the nanospike are aligned with both facets touching. Then, a modest heating power is used for a short duration. The power is just high enough to soften the silica glass. Once the two fibres are lightly fused together, pressure is applied to move them slightly closer together and the splice joint is heated again. This process needs to be repeated several times to enhance the strength of the joint. The final fused fibres are still very delicate. Thus, to protect the splicing joint, the integrated device is inserted into a capillary tube and filled with polymer wax for mechanical support.

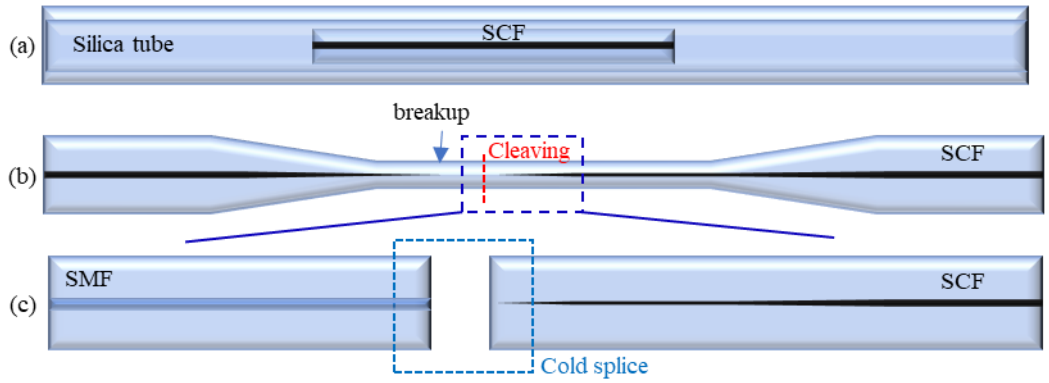

Figure 6.3 Fabrication of the nanospike and splicing with SMF. (a) Sample preparation of the SCF. The SCF is inserted into a silica tube for mechanical support and also to increase the cladding thickness. (b) SCF with nanospike forms between the waist and down transition region. (c) Cleaved SCF is spliced with SMF.

Fig. 6.4 show a few slightly different SCFs with nanospikes and their splicing with the SMF (Sample A, B and C). The silicon nanospike in sample A was spliced using a commercial fusion splicer (Sumitomo type-35SE). It was completely destroyed in the splicing process as a result of exceeding heating. Although the claddings of the SCF and SMF are fused strongly, this sample is not expected to have good transmission qualities. The nanospike in sample B has a good quality in the microscope image before splicing, the end of the tip has a ~50 µm distance to the fibre end. However, after the fusion, the nanospike shape is affected by the heating during the splicing process, as the tip position moves away from the SMF and the tip angle becomes larger. Sample C has a small air gap between the silica tube and the SCF near the nanospike region. This gap is accidently formed as the starting tapering position is not optimised. The cleaving facet of this fibre is closer to the tip. After splicing, however, the tip is less affected by the heating compared with sample B. This could be caused by the air gap as it acts as a heat insulating layer when splicing. After splicing, these samples were put into polymer capillaries and fixed with adhesive wax. The SMF sides of these devices were spliced to fibre patch cables. The SCF sides of these devices were polished following the same procedure discussed in Chapter 3.

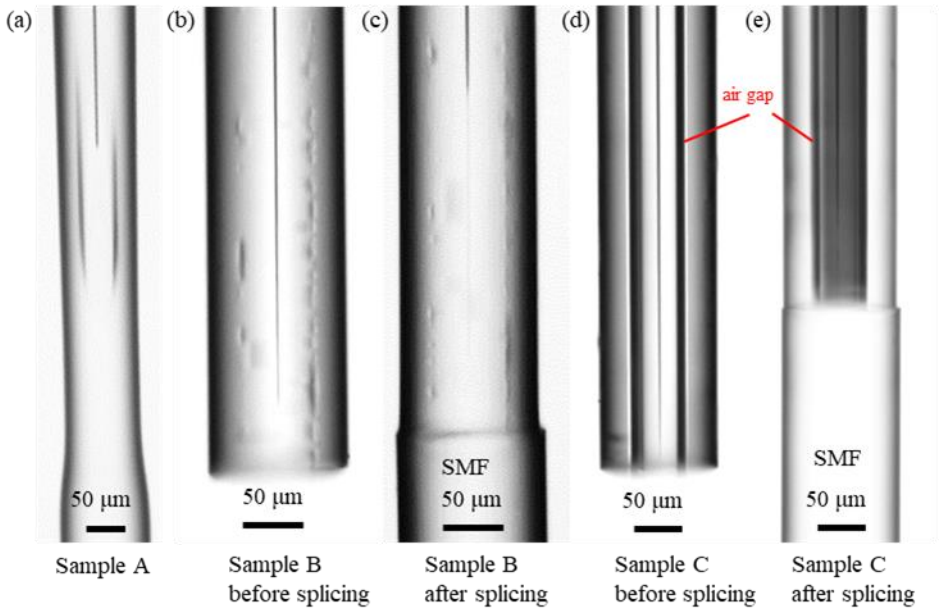

Figure 6.4 (a) Splicing of nanospike with SMF using commercial arc splicer. (b)-(c) SCF with nanospike before and after splicing with SMF. The glass tube is fused with the SCF cladding. (d)-(e) SCF with nanospike before and after splicing with SMF. The glass tube is not fused with the SCF cladding.

6.2.2 Optical characterisation

The optical transmission of the samples A, B and C in Fig. 6.4 were characterised. The experimental setup is shown in Fig. 6.5 (a). The SMF side of the devices were connected to a CW fibre laser source with a centre wavelength at 1.55 µm. The output light was collected via a 40x objective lens and recorded by a CCD camera. To measure the power transmitted within the core, a pinhole was used to block the light transmitted in the cladding. The output mode profiles (without pinhole) of these samples are shown in Fig. 6.5 (b), (c) and (d). For sample A and B, the spike shapes and position are affected by the splicing process, leading to a poor coupling efficiency. It can be seen that most of the power is transmitted in the cladding. For sample C, the spike shape remains unaffected in the splicing process so the coupling efficiency into the core is much higher than the other two devices. Most of the light is transmitted in the core. Furthermore, the unfused gap between the SCF and the glass tube also improves the coupling efficiency, as the gap reduces the size of the SCF cladding which leads to a smaller mode area that better matches the mode from the SMF.

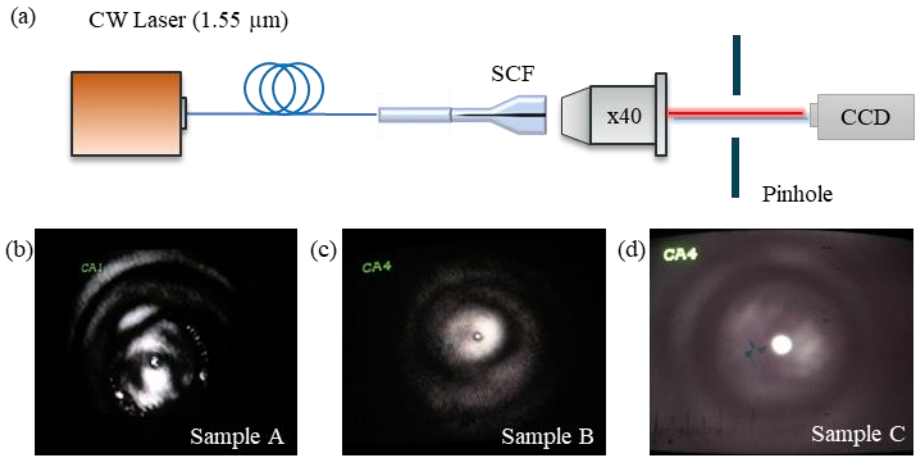

Figure 6.5 (a) Optical characterisation setup used for loss measurements. (b-d) Output mode images measured from the CCD camera without the pinhole for the different samples, as labelled.

For sample C, the insertion loss is measured to be 23 dB at 1.55 μm. The SCF part of the device is around 1 cm long. Assuming the fibre has an average loss of 5 dB/cm, the loss at the splice joint is roughly estimated to be around 10 dB by excluding the losses of the connector, fibre main body, reflection at the SCF output, and collection efficiency by the objective lens. Although this method successfully integrates SCF with the SMF, the coupling loss is still very high. The reason can be summarised as below:

1. The spike shape is usually changed by the splicing process.

2. With the current technique, it is difficult to align the nanospike and SMF accurately. Small alignment error can lead to large coupling loss.

3. The distance between the cleaving point and the tip end is difficult to control. Light will spread out into the cladding if this distance is large. Simulation shows that 1-2 dB extra coupling loss will be introduced if the length is 50 μm.

6.3 Splicing SCF nanospike to tapered SMF

To further improve the coupling efficiency and increase the fabrication robustness of the nanospike coupler, another design was investigated that uses a tapered SMF as an intermediate section between the SMF and SCF nanospike, as shown in Fig. 6.6 (a). Inspired by sample C in Fig.6.4, we noticed that the coupling efficiency could be greatly improved by using a SCF with a smaller cladding. The idea of the new design was to reduce the cladding size of both the SCF and SMF to increase the mode matching between the two fibres. Fig. 6.6 (b) shows the mode profiles of a SCF with different core sizes. The cladding diameter of the SCF is 10 μm. Different from the modal

behaviour in Fig. 6.1 (a), it is treated as a three-layer index fibre, as the mode is limited by the cladding/air interface when the light extends out of the core. As the cladding of the SCF is small, the SMF also needs to be tapered to match the size of the SCF for splicing.

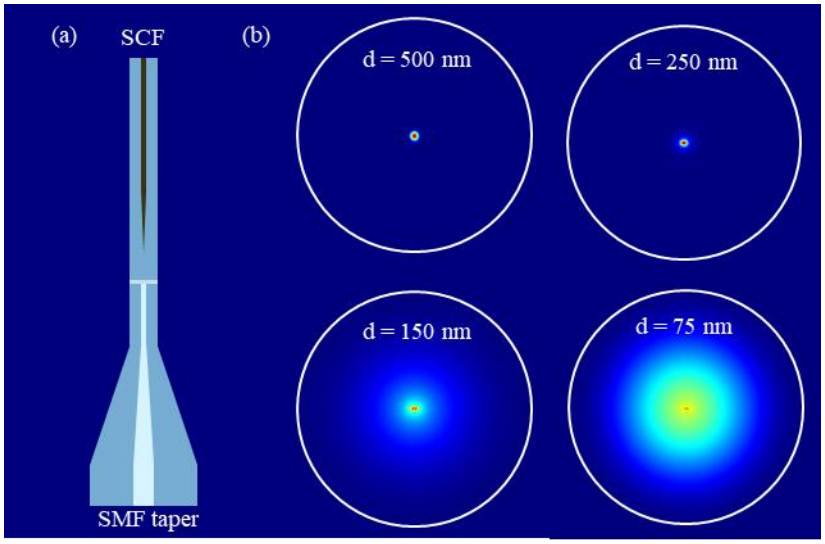

Figure 6.6 (a) Schematic of the SCF nanospike integration with tapered SMF. (b) Mode profile of SCF with same 10 µm diameter cladding and different core diameters at λ = 1.55 µm.

6.3.1 Fabrication

The as-drawn SCF used in this design has a cladding diameter of 144 µm and core diameter of 5.5 µm. For nonlinear applications in the telecommunication c-band, the core diameter needs to be around 1 µm. Thus, the cladding diameter needs to be tapered down to ~30 µm. As the targeted core diameter is very small, the heating power used in the tapering process needs to be kept as low as possible to prevent break-up of the core. However, we find that it is difficult to choose a proper heat power to form the nanospike with 1 µm core, as the power is either too high, resulting in discontinuities in the core, or too low, so that the nanospikes cannot form. Thus, the fabrication process was modified.

The cores of the as-drawn SCFs are poly-crystalline and under tensile stress due to the large difference in the thermal expansion coefficients of silica and silicon [54]. This tensile stress can be used to create a void gap by melting the core locally with a heat-polishing method based on unidirectional movement of the as-drawn fiber in a hot zone, as shown in Fig. 6.7. With this void gap, the nanospike can be formed more easily.

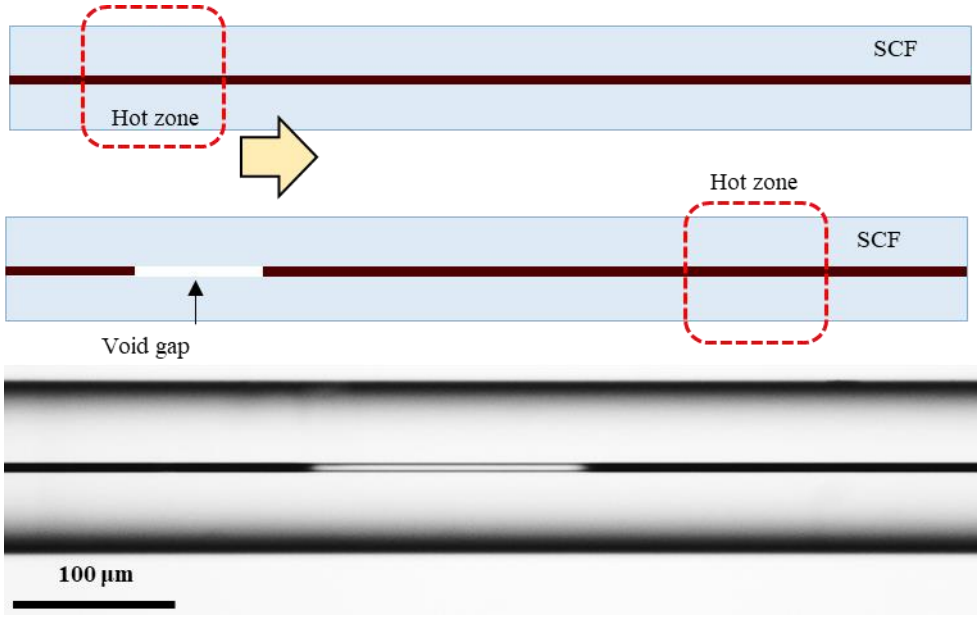

Figure 6.7 Illustration of void gap formation of SCF. Lower image shows the microscope image of a SCF with a void gap.

The modified fabrication process is shown in Fig. 6.8. After the spike formation by tapering, the fibre is cleaved on the left side of the silicon tip. The cleaving position needs to be at least 1 mm away from the tip to prevent the spike being damaged by the heating during splicing. The cleaved facet of a fibre is shown as an inset in Fig. 6.8 (c). There is a small bright spot in the centre of the fibre. This indicates that this cleaved section is actually not coreless, instead, the CaO interface layer between the silicon core and cladding acts as the fibre core in the absence of a silicon core.

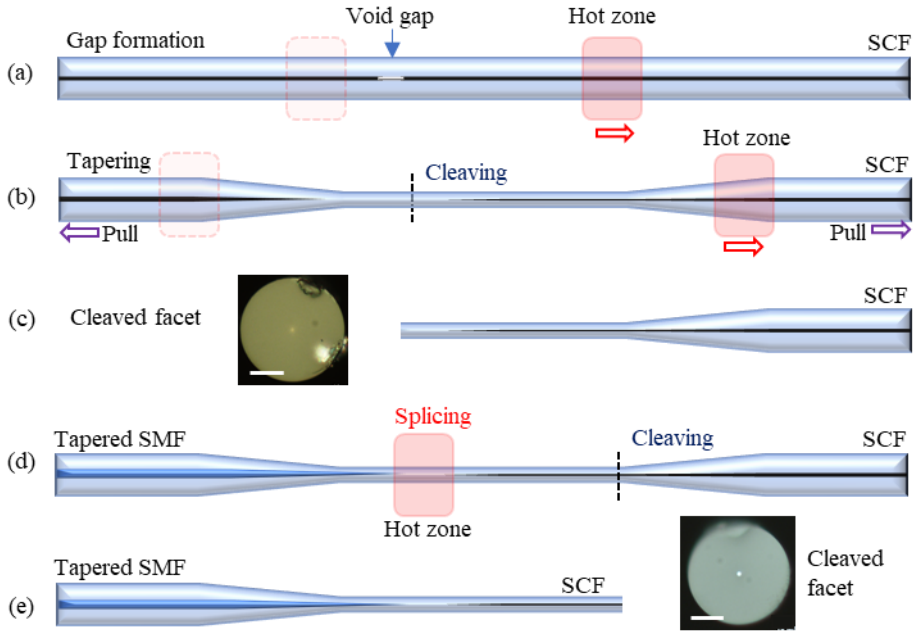

Figure 6.8 Fabrication of the nanospike and splicing to a tapered SMF. (a) Gap formation in the core of the SCF. (b) Tapering the SCF and formation of the nanospike.

(c) Cleaving near the nanospike. The inset shows the cleaved facet. The scale bar is 10 µm. (d) Splicing of the tapered SCF with a tapered SMF. (e) Remove the up transition of the tapered SCF by cleaving. The inset photo shows the cleaved facet. The scale bar is 10 µm.

The cleaved SCF with the nanospike tip is then spliced with a tapered SMF. The cladding diameter of the SMF is also tapered adiabatically to 30 µm to match the size of the SCF. During the tapering, the transmission of the SMF is monitored by a power meter. The insertion loss of the tapered SMF is usually below 0.2 dB, which can be neglected. The tapered SMF is then cleaved at the taper waist position. Finally, the tapered SMF and SCF with nanospike are spliced using the Vytran tapering rig. The splicing process requires much lower heating power as the fibre is much smaller. Also, as the splicing joint is away from the silicon tip, the shape of nanospike is unaffected in this process.

Small core fibre cleaving and splicing

As the fibre cladding diameter is only 30 µm, it cannot be cleaved by a conventional cleaver. To cleave fibres with these dimensions, the Vytran tapering rig is reconfigured into a cleaver by manually attaching a blade onto the splice head, shown in Fig. 6.9 (a). The tension monitor on the fibre holder stage and microscope can be used to monitor the cleaving process. Fig. 6.9 (b) shows the top view from the microscope of the cleaving process.

The fibre cleaving can be completed by 4 steps:

1. The fibre is placed on the V groove of the two stages. These stages are moved slightly away from each other to create a small tension (~20 gram-force for 30 µm fibre diameter) on the fibre.
2. The splice head with the blade attached rises slowly until the blade touches the fibre. Then the blade needs to rise another ~ 10- 20 µm to increase the contact.
3. Lightly push the fibre in the vertical direction forward and backward with a probe to score a breach on the fibre surface.
4. Gently tap the fibre in the vertical direction with a probe and cleave the fibre.

The splicing of the 30 µm core fibre is similar to the conventional splicing process. The two fibres are aligned properly, heating and pushing together at the same time. However, as the fibres are very small, the splicing parameters need to be experimental tested many times before finding the optimised splicing parameters. Table 6.1 shows the splicing parameters that were used for splicing optimisation. In this table, the Pre-gap is the distance between the two fibre sections before splicing; The Hot-push is the pushing distance; The Velocity is the pushing velocity; The Delay is the heating time before pushing; The Duration is the heating duration; The Power is the electric power applied

on the filament; The strength is the minimum tension to break the splicing joint (unit is gram-force). As shown in Fig.6.9 (c), we demonstrate that it is possible to perfectly splice the fibre in this dimension using the parameters in Table 6.1 (Sample number 10).

Table 6.1 Splicing optimisation of Vytran parameters (FTAV4 filament).

Sample number	1	2	3	4	5	6	7	8	9	10
Pre-gap (µm)	8	8	8	8	8	1	1	1	1	1
Hot-push (µm)	0	32	32	33	10	3	5	8	5	7
Velocity (µm/s)	50	30	10	7	50	3	5	8	50	10
Delay (s)	0.2	0.2	0.2	0.2	0.2	0.1	0.1	0.1	0.05	0.05
Duration (s)	5	5	5	5	5	4	4	4	4	7
Power (W)	50	50	50	50	55	55	55	55	55	55
Strength (g)	-	4	20	7	30	25	large	large	large	large

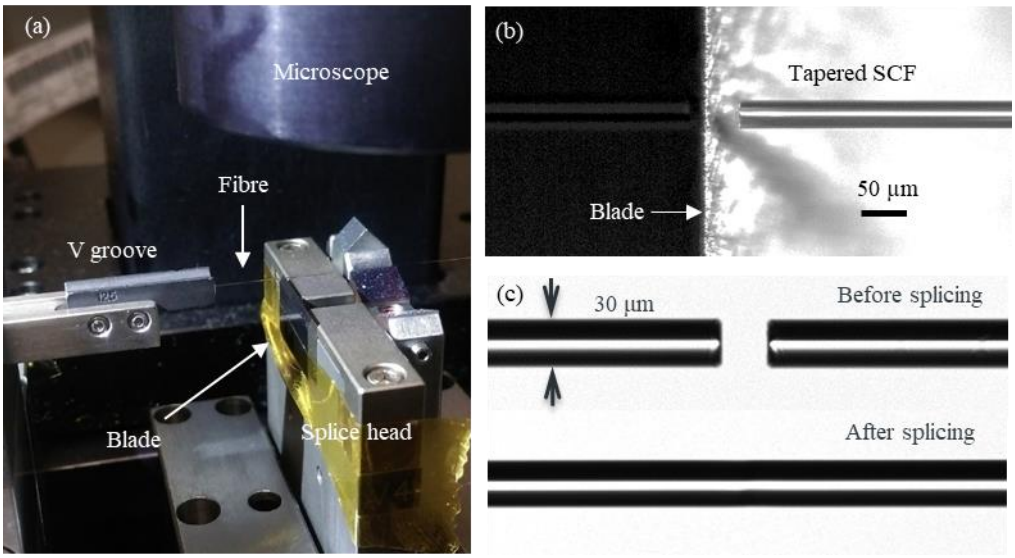

Figure 6.9 (a) Microscope top view of the cleaved fibre and blade. (b) Cleaving of the 30 µm core fibre. (b) Splicing of the 30 µm core fibre.

6.3.2 Optical characterisation

The schematic of the light propagation in the device is shown in Fig. 6.10. The light transmission can be divided into 4 parts, as shown in Fig. 6.10:

1. The light is transmitted into the tapered region of the SMF, the mode expands slowly and becomes cladding guided. The loss in this section is negligible as the fibre is adiabatically

tapered. The large mode area means that the fibre is not sensitive to misalignment at splicing joint.

2. The light enters the coreless section of the SCF. In this section, the SCF only has a thin layer of CaO that acts as the fibre core. Its refractive index is assumed to be 1.6, which is between the refractive index of silica and CaO.
3. The light is coupled into the nanospike.
4. The light propagates in the SCF main body.

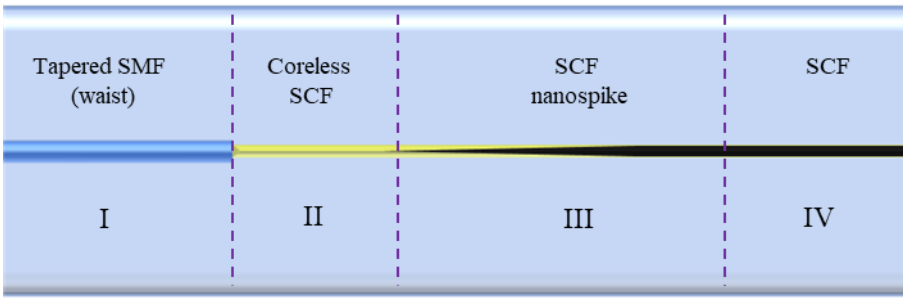

Figure 6.10 Schematic of the light transmission in the SMF-SCF devices.

We use the cutback method to characterize the optical transmission properties of the device. The transmission setup is shown in Fig. 6.11 (a). The SMF-SCF device under test is connected to a 1.55 μm CW fibre laser source (Tunics T100S-HP). The power from the laser is set to be 1 mW. A 63x objective lens with a NA of 0.85 is used to collect the output power from the cleaved facet. The output mode is a superposition of cladding guided and core guided modes, as can be seen from the image in Fig. 6.11 (b), taken by a CCD camera. Fig. 6.11 (c) shows the simulated mode profile from the device output using COMSOL. Note, all of the COMSOL modeling in this section was conducted by Dr. Ozan Aktas. A pinhole was used to filter the cladding mode so that only the core mode remained for the power measurement. The output mode profiles measured by a beam profiler (Pyrocam IIIHR, Ophir Optronics) before and after spatial filtering are shown in Fig.6.11 (b) and (c), respectively.

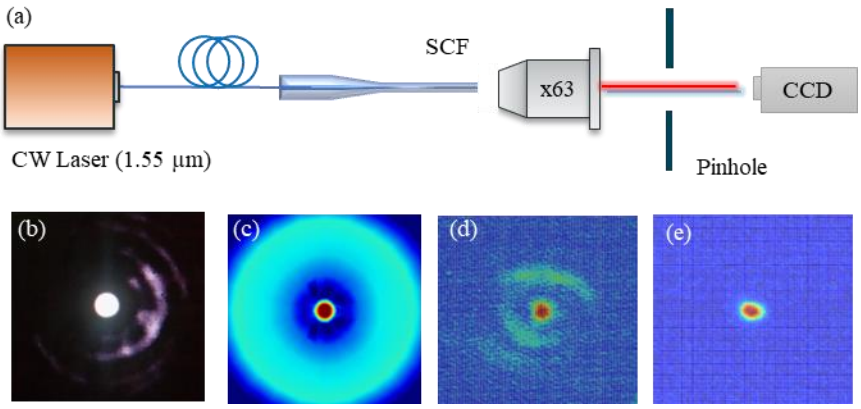

Figure 6.11 Optical characterisation setup used for loss measurements. (b) IR camera image of the output mode profile. (c) Simulated power profile of the output mode. (d) Experimental output mode profile image taken by a beam profiler. (e) Output mode profile after spatial filtering of the cladding guided mode.

The power was measured at 5 different cut-back positions along the device, as shown in the inset of Fig. 6.12 (a). Initially, the total transmitted power is 330 µW, including light from the cladding and core. After spatial filtering, the power of the core guided mode was measured to be 118 µW at position *a*, which corresponds to a total loss of 9.2 dB. A short section of the fibre is then removed by cleaving, and the transmission is measured using the same method. A total 8 mm section of the fibre is removed for the cutback measurements. A linear fit to the cut-back data was used to calculate a propagation loss of 1.66 ± 0.54 dB/cm. The uncertainty in the measurements occurs due to the slight changes in the angle of cleaving, the surface quality, and the output coupling condition. In the end, the SCF part of the device is totally removed from position *e*. The insertion loss of the remaining part is measured to be 2 dB, which includes fiber connector loss, SMF taper loss, and the mode conversion loss at the splicing point (calculated to be 1.25 dB from COMSOL). The nanospike coupling loss is then estimated to be 2.75 dB, assuming the reflection from the silicon air interface is 1.5 dB and lens collection efficiency is 1 dB (lens collection efficiency is calculated using Lumerical Software). This is much lower than the coupling efficiency of free space coupling for a 1 µm core size SCF, which is often over 20 dB.

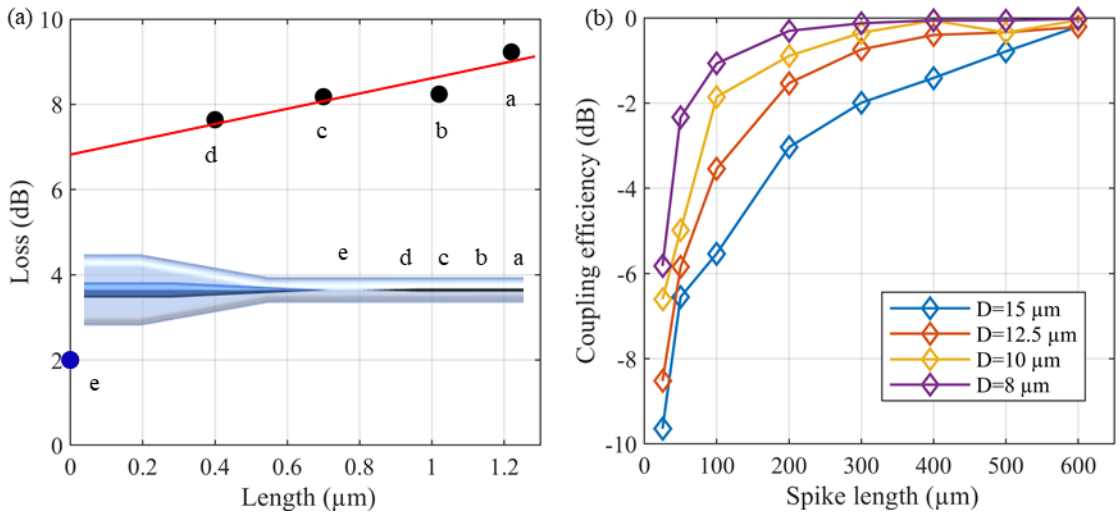

Figure 6.12 (a) Loss measurements with a linear fit to the data. Inset schematically shows cut-back positions where the tapered SCF was cleaved. (b) Simulated coupling efficiency as a function of the spike length and cladding diameter using 3D model in COMSOL.

The light transmission in the SMF-SCF device was also simulated in a 3D model using COMSOL. The coupling loss of the nanospike was calculated with different cladding diameters from 8-15 μm and CaO layer thickness from 0-400 nm at 1.55 μm. The nanospike starts from 5 nm in diameter and widens to a core diameter of 1 μm at the end of the transition length of 200 μm. Material absorption and scattering were assumed to be zero to investigate only the effects of a change in dimension on the coupling losses. For a CaO layer with a thickness of 260 nm in our device, the coupling loss from the nanospike is shown in Fig. 6.12 (b). It can be seen that smaller cladding sizes and longer spike lengths lead to higher coupling efficiencies. When the device dimension is optimised, theoretical, the coupling loss can be negligible small as shown in the Fig. 6.12 (b).

6.4 Conclusion

In summary, the tapered SCFs with nanospikes and their robust integration with SMFs by splicing was studied. The fabrication process of these devices is detailed documented. Loss measurements have revealed the propagation and nanospike coupling losses for our 30 μm cladding diameter device to be below 2 dB/cm and 4 dB, respectively. The coupling efficiency can be further improved by reducing the cladding size of the SCF. Seamless integration of SMFs and SCFs can pave the way for photonic and optoelectronic devices such as SCF Raman amplifiers and fiber photodetectors.

Chapter 7 Conclusion and future work

7.1 Conclusion

In summary, this thesis has investigated tapered SCFs as a novel nonlinear photonics platform. The fabrication techniques of small core SCFs, including the tapering process, sample preparation is studied and detailed documented. Two types of fibre mounting techniques for tapering are introduced, including the capillary method and splicing method. A numerical model based on fluid dynamics has been developed to describe the tapering process of the SCFs. The technique of tapering nanometre scale SCFs is studied with both theory and hands on experience. Transmissions of the tapered SCFs with a range of different core sizes are characterised experimentally by cutback measurements and the Fabry-perot cavity analysis. The SCF with propagation loss down to less than 1 dB/cm, which is the lowest SCF to date were fabricated in this work. The nonlinear properties of crystalline SCF, including nonlinear absorption and nonlinear refraction are characterised from telecommunication bands to mid-IR for the first time. By pumping a SCF with high intensity femtosecond pulses, the spectral broadening is recorded and fitted with numerical simulations to determine the nonlinear parameters. The FOM_{NL} increases for longer wavelengths, making SCFs a suitable platform for nonlinear applications in the mid-IR region. SCG in SCFs is studied in straight and tapered fibre profiles. It is shown that SCFs with an asymmetric tapered profile can greatly enhance the SC bandwidth and power efficiency. A broadband SC (1.67-5.3 μm) has been generated in a tapered SCF, using a femtosecond pump, which has a high power efficiency and coherence. Simulation shows that by further optimise the fibre structure, SCFs has the potential to generate supercontinuum cover its full transmission window in the mid-IR. A nanospike coupler has been developed for efficient light coupling between SCFs and standard fibre systems, with a 2.8 dB coupling loss achieved experimentally. This is the first fibre integration of semiconductor photonic device. This nanotaper coupler paves the way for all fibre SCF devices. These results show the promising future of the SCFs being used in mid-IR sources and other nonlinear applications.

7.2 Future work

Although this work has many achievements, most of the studies have been focused on optimizing the tapered fabrication techniques and optical characterisation. Thus the SCFs are still far from commercialisation. The next step is to carry on the optimisation work, at the same time, make progress on practical nonlinear photonics devices. A few proposals are listed below.

1. Mid-IR optical parametric amplification (OPA). OPA is a degenerate FWM process that requires precision dispersion engineering of the fibre. Since the dispersion of SCF can be engineered via tapering, SCF has the potential to be used as optical parametric amplifier, especially in the mid-IR where the FOM_{NL} is large.

2. Raman amplification. Large gain Raman amplification has been demonstrated in planar silicon waveguides, due to the narrow Raman response of silicon. SCF has greater power handling abilities than planar silicon waveguide, thus, it has a great potential of being used as Raman amplifier or even lasing.

3. All fibre device integration. Although Chapter 6 has demonstrated the nanospike integration method, it only integrated one end of the SCF to a standard fibre system. This technique needs further improvement for double-ended nanospike integration with SMF for the development of all-fibre silicon photonic systems.

4. Investigations of other nonlinear processes that would benefit from precise dispersion engineering such as pulse shaping, broadband frequency comb generation, single photon sources.

5. Commercialization. Including cost reduction, quality control.

List of publications

Journals

First author publications

1. **Ren, Haonan**, Aktas, Ozan, Franz, Yohann, Runge, Antoine F.J., Hawkins, Thomas, Ballato, John, Gibson, Ursula J. and Peacock, Anna (2017) Tapered silicon core fibers with nano-spikes for optical coupling via spliced silica fibers. Optics Express, 25 (20), 24157-24163. (doi:10.1364/OE.25.024157).

2. **Ren, Haonan**, Shen, Li, Wu, Dong, Aktas, Ozan, Hawkins, T., Ballato, John, Gibson, Ursula and Peacock, Anna (2019) Nonlinear optical properties of polycrystalline silicon core fibers from telecom wavelengths into the mid-infrared spectral region. Optical Materials Express, 9 (3), 1271-1279. (doi:10.1364/OME.9.001271).

3. **Ren, H**., Shen, L., Runge, A.F.J. et al. Low-loss silicon core fibre platform for mid-infrared nonlinear photonics. Light Sci Appl 8, 105 (2019). https://doi.org/10.1038/s41377-019-0217-z

Co-author publications

1. Peacock, Anna, Campling, Joseph, Runge, Antoine, **Ren, Haonan**, Shen, Li, Aktas, Ozan, Horak, Peter, Healy, Noel, Gibson, Ursula J. and Ballato, John (2017) Wavelength conversion and supercontinuum generation in silicon optical fibers. *IEEE Journal of Selected Topics in Quantum Electronics*.(doi:10.1109/JSTQE.2017.2762958).

2. Franz, Y., Runge, A.F.J., **Ren, H**., Healy, N., Ignatyev, K., Jones, M., Hawkins, T., Ballato, J., Gibson, U.J. and Peacock, A.C. (2017) Material properties of tapered crystalline silicon core fibers. *Optical Materials Express*, 7(6), 2055-2061. (doi:10.1364/OME.7.002055).

3. Wu, Dong, Shen, Li, **Ren, Haonan**, Campling, Joseph, Hawkins, Thomas, Ballato, John, Gibson, Ursula and Peacock, Anna (2019) Net optical parametric gain in a submicron silicon core ber pumped in the telecom band. *APL Photonics*. (Accepted)

4. Meng Huang, **Haonan Ren**, Ozan Aktas, Li Shen, Jian Wang, Thomas W. Hawkins, John Ballato, Ursula J Gibson, and Anna C. Peacock (2019) Fiber integrated wavelength converter based on a silicon core fiber with a nano-spike coupler. IEEE Photonics Technology Letters. (doi: 10.1109/LPT.2019.2937650).

Conference

1.Aktas, Ozan, **Ren, Haonan,** Runge, Antoine F.J., Peacock, Anna, Hawkins, Thomas, Ballato, John and Gibson, U. "Interfacing telecom fibers and silicon core fibers with nano-spikes for in-fiber silicon devices." Optical Fiber Communication Conference (OFC 2018), San Diago, United States. 11 - 15 Mar 2018.

2.**Ren, H.**, Shen, L., Campling, J., Runge, A.F.J., Aktas, O., Hawkins, T., Horak, P., Ballato, John, Gibson, U. and Peacock, A.C. "Octave-spanning supercontinuum generation in a dispersion managed tapered crystalline silicon core fiber." Conference on Lasers and Electro-optics (CLEO 2018), San Jose, United States. 13 - 18 May 2018.

3.**Ren, Haonan**, Aktas, Ozan, Runge, Antoine FJ, Hawkins, Thomas, Ballato, John, Gibson, Ursula and Peacock, Anna. "Integration of silicon core fibres to single mode fibres using nanospike with improved coupling efficiency", Workshop on Speciality Optical Fibers and their Applications (WSOF 2017) Limassol, Cyprus, 11-13 Oct 2017.

4.**Ren, Haonan**, Runge, Antoine, Campling, Joseph, Jones, Max, Hawkins, Thomas, Ballato, John, Horak, Peter, Gibson, Ursula J. and Peacock, Anna, "Silicon fibre nano-spike for robust coupling to silica fibres." CLEO/Europe - EQEC 2017, Munich, Germany. 25 - 29 Jun 2017.

5.Peacock, Anna, **Ren, Haonan**, Healy, Noel and Runge, Antoine, Semiconductor optical fibers for nonlinear photonics. At CLEO-Pacific Rim 2017 CLEO-Pacific Rim 2017, Singapore, Singapore. 31 Jul - 04 Aug 2017.

References

[1] W. N. Ye and Y. Xiong, 'Review of silicon photonics: history and recent advances', *Journal of Modern Optics*, vol. 60, no. 16, pp. 1299–1320, Sep. 2013, doi: 10.1080/09500340.2013.839836.

[2] R. Soref and J. Larenzo, 'All-silicon active and passive guided-wave components for λ = 1.3 and 1.6 μm', *IEEE Journal of Quantum Electronics*, vol. 22, no. 6, pp. 873–879, Jun. 1986, doi: 10.1109/JQE.1986.1073057.

[3] W. Bogaerts *et al.*, 'Silicon microring resonators', *Laser & Photonics Reviews*, vol. 6, no. 1, pp. 47–73, 2012, doi: 10.1002/lpor.201100017.

[4] G. T. Reed, G. Mashanovich, F. Y. Gardes, and D. J. Thomson, 'Silicon optical modulators', *Nature Photonics*, vol. 4, no. 8, pp. 518–526, Aug. 2010, doi: 10.1038/nphoton.2010.179.

[5] L.-W. Luo *et al.*, 'WDM-compatible mode-division multiplexing on a silicon chip', *Nature Communications*, vol. 5, p. 3069, Jan. 2014, doi: 10.1038/ncomms4069.

[6] V. R. Almeida *et al.*, 'All-optical switching on a silicon chip', *Opt. Lett., OL*, vol. 29, no. 24, pp. 2867–2869, Dec. 2004, doi: 10.1364/OL.29.002867.

[7] Y. Takahashi, Y. Inui, M. Chihara, T. Asano, R. Terawaki, and S. Noda, 'A micrometre-scale Raman silicon laser with a microwatt threshold', *Nature*, vol. 498, no. 7455, pp. 470–474, Jun. 2013, doi: 10.1038/nature12237.

[8] X. Liu, R. M. Osgood Jr, Y. A. Vlasov, and W. M. J. Green, 'Mid-infrared optical parametric amplifier using silicon nanophotonic waveguides', *Nature Photonics*, vol. 4, no. 8, pp. 557–560, Aug. 2010, doi: 10.1038/nphoton.2010.119.

[9] B. Kuyken, X. Liu, R. M. Osgood, R. Baets, G. Roelkens, and W. M. J. Green, 'Mid-infrared to telecom-band supercontinuum generation in highly nonlinear silicon-on-insulator wire waveguides', *Opt. Express, OE*, vol. 19, no. 21, pp. 20172–20181, Oct. 2011, doi: 10.1364/OE.19.020172.

[10] A. G. Griffith *et al.*, 'Silicon-chip mid-infrared frequency comb generation', *Nature Communications*, vol. 6, no. 1, Dec. 2015, doi: 10.1038/ncomms7299.

[11] 'Extending opportunities', *Nature Photonics*, vol. 6, no. 7, p. 407, Jul. 2012, doi: 10.1038/nphoton.2012.164.

[12] G. Z. Mashanovich *et al.*, 'Low loss silicon waveguides for the mid-infrared', *Opt. Express, OE*, vol. 19, no. 8, pp. 7112–7119, Apr. 2011, doi: 10.1364/OE.19.007112.

[13] N. Singh *et al.*, 'Midinfrared supercontinuum generation from 2 to 6 μm in a silicon nanowire', *Optica*, vol. 2, no. 9, p. 797, Sep. 2015, doi: 10.1364/OPTICA.2.000797.

[14] S. Khan, J. Chiles, J. Ma, and S. Fathpour, 'Silicon-on-nitride waveguides for mid- and near-infrared integrated photonics', *Appl. Phys. Lett.*, vol. 102, no. 12, p. 121104, Mar. 2013, doi: 10.1063/1.4798557.

[15] Z. Cheng, X. Chen, C. Y. Wong, K. Xu, and H. K. Tsang, 'Mid-infrared Suspended Membrane Waveguide and Ring Resonator on Silicon-on-Insulator', *IEEE Photonics Journal*, vol. 4, no. 5, pp. 1510–1519, Oct. 2012, doi: 10.1109/JPHOT.2012.2210700.

[16] P. T. Lin, V. Singh, Y. Cai, L. C. Kimerling, and A. Agarwal, 'Air-clad silicon pedestal structures for broadband mid-infrared microphotonics', *Opt. Lett., OL*, vol. 38, no. 7, pp. 1031–1033, Apr. 2013, doi: 10.1364/OL.38.001031.

[17] R. Marchetti, C. Lacava, L. Carroll, K. Gradkowski, and P. Minzioni, 'Coupling strategies for silicon photonics integrated chips [Invited]', *Photonics Research*, vol. 7, no. 2, p. 201, Feb. 2019, doi: 10.1364/PRJ.7.000201.

[18] P. Mehta, N. Healy, T. D. Day, J. V. Badding, and A. C. Peacock, 'Ultrafast wavelength conversion via cross-phase modulation in hydrogenated amorphous silicon optical fibers', *Optics Express*, vol. 20, no. 24, p. 26110, Nov. 2012, doi: 10.1364/OE.20.026110.

[19] F. H. Suhailin *et al.*, 'Kerr nonlinear switching in a hybrid silica-silicon microspherical resonator', *Optics Express*, vol. 23, no. 13, p. 17263, Jun. 2015, doi: 10.1364/OE.23.017263.

[20] L. Shen *et al.*, 'Four-wave mixing and octave-spanning supercontinuum generation in a small core hydrogenated amorphous silicon fiber pumped in the mid-infrared', *Optics Letters*, vol. 39, no. 19, p. 5721, Oct. 2014, doi: 10.1364/OL.39.005721.

[21] F. A. Martinsen, B. K. Smeltzer, M. Nord, T. Hawkins, J. Ballato, and U. J. Gibson, 'Silicon-core glass fibres as microwire radial-junction solar cells', *Scientific Reports*, vol. 4, no. 1, May 2015, doi: 10.1038/srep06283.

[22] P. J. A. Sazio, 'Microstructured Optical Fibers as High-Pressure Microfluidic Reactors', *Science*, vol. 311, no. 5767, pp. 1583–1586, Mar. 2006, doi: 10.1126/science.1124281.

[23] J. Ballato *et al.*, 'Silicon optical Fiber', *Optics Express*, vol. 16, no. 23, p. 18675, Nov. 2008, doi: 10.1364/OE.16.018675.

[24] F. H. Suhailin *et al.*, 'Tapered polysilicon core fibers for nonlinear photonics', *Optics Letters*, vol. 41, no. 7, p. 1360, Apr. 2016, doi: 10.1364/OL.41.001360.

[25] B. N. Kurdi and D. G. Hall, 'Optical waveguides in oxygen-implanted buried-oxide silicon-on-insulator structures', *Opt. Lett., OL*, vol. 13, no. 2, pp. 175–177, Feb. 1988, doi: 10.1364/OL.13.000175.

[26] D. J. Albares and R. A. Soref, 'Silicon-On-Sapphire Waveguides', in *Integrated Optical Circuit Engineering IV*, Mar. 1987, vol. 0704, pp. 24–26, doi: 10.1117/12.937191.

[27] R. A. Soref, F. Namavar, and J. P. Lorenzo, 'Optical waveguiding in a single-crystal layer of germanium silicon grown on silicon', *Opt. Lett., OL*, vol. 15, no. 5, pp. 270–272, Mar. 1990, doi: 10.1364/OL.15.000270.

[28] G. T. Reed and A. P. Knights, *Silicon photonics: an introduction*. Chichester ; Hoboken, NJ: John Wiley, 2004.

[29] R. Claps, D. Dimitropoulos, Y. Han, and B. Jalali, 'Observation of Raman emission in silicon waveguides at 1.54 µm', *Opt. Express, OE*, vol. 10, no. 22, pp. 1305–1313, Nov. 2002, doi: 10.1364/OE.10.001305.

[30] R. Claps, D. Dimitropoulos, V. Raghunathan, Y. Han, and B. Jalali, 'Observation of stimulated Raman amplification in silicon waveguides', *Opt. Express, OE*, vol. 11, no. 15, pp. 1731–1739, Jul. 2003, doi: 10.1364/OE.11.001731.

[31] O. Boyraz and B. Jalali, 'Demonstration of a silicon Raman laser', *Opt. Express, OE*, vol. 12, no. 21, pp. 5269–5273, Oct. 2004, doi: 10.1364/OPEX.12.005269.

[32] H. Rong *et al.*, 'A continuous-wave Raman silicon laser', *Nature*, vol. 433, no. 7027, p. 725, Feb. 2005, doi: 10.1038/nature03346.

[33] H. Rong *et al.*, 'A cascaded silicon Raman laser', *Nature Photonics*, vol. 2, no. 3, pp. 170–174, Mar. 2008, doi: 10.1038/nphoton.2008.4.

[34] H. Fukuda *et al.*, 'Four-wave mixing in silicon wire waveguides', *Opt. Express, OE*, vol. 13, no. 12, pp. 4629–4637, Jun. 2005, doi: 10.1364/OPEX.13.004629.

[35] R. L. Espinola, J. I. Dadap, R. M. Osgood, Jr., S. J. McNab, and Y. A. Vlasov, 'C-band wavelength conversion in silicon photonic wire waveguides', *Optics Express*, vol. 13, no. 11, p. 4341, 2005, doi: 10.1364/OPEX.13.004341.

[36] M. A. Foster, A. C. Turner, J. E. Sharping, B. S. Schmidt, M. Lipson, and A. L. Gaeta, 'Broad-band optical parametric gain on a silicon photonic chip', *Nature*, vol. 441, no. 7096, p. 960, Jun. 2006, doi: 10.1038/nature04932.

[37] R. Salem, M. A. Foster, A. C. Turner, D. F. Geraghty, M. Lipson, and A. L. Gaeta, 'Signal regeneration using low-power four-wave mixing on silicon chip', *Nature Photonics*, vol. 2, no. 1, pp. 35–38, Jan. 2008, doi: 10.1038/nphoton.2007.249.

[38] X. Liu, B. Kuyken, G. Roelkens, R. Baets, R. M. Osgood Jr, and W. M. J. Green, 'Bridging the mid-infrared-to-telecom gap with silicon nanophotonic spectral translation', *Nature Photonics*, vol. 6, no. 10, pp. 667–671, Oct. 2012, doi: 10.1038/nphoton.2012.221.

[39] J. M. Dudley, G. Genty, and S. Coen, 'Supercontinuum generation in photonic crystal fiber', *Reviews of Modern Physics*, vol. 78, no. 4, pp. 1135–1184, Oct. 2006, doi: 10.1103/RevModPhys.78.1135.

[40] I.-W. Hsieh *et al.*, 'Supercontinuum generation in silicon photonic wires', *Opt. Express, OE*, vol. 15, no. 23, pp. 15242–15249, Nov. 2007, doi: 10.1364/OE.15.015242.

[41] L. Yin, Q. Lin, and G. P. Agrawal, 'Soliton fission and supercontinuum generation in silicon waveguides', *Optics Letters*, vol. 32, no. 4, p. 391, Feb. 2007, doi: 10.1364/OL.32.000391.

[42] U. D. Dave, S. Uvin, B. Kuyken, S. Selvaraja, F. Leo, and G. Roelkens, 'Telecom to mid-infrared spanning supercontinuum generation in hydrogenated amorphous silicon waveguides using a Thulium doped fiber laser pump source', *Optics Express*, vol. 21, no. 26, p. 32032, Dec. 2013, doi: 10.1364/OE.21.032032.

[43] R. K. W. Lau, M. R. E. Lamont, A. G. Griffith, Y. Okawachi, M. Lipson, and A. L. Gaeta, 'Octave-spanning mid-infrared supercontinuum generation in silicon nanowaveguides', *Opt. Lett., OL*, vol. 39, no. 15, pp. 4518–4521, Aug. 2014, doi: 10.1364/OL.39.004518.

[44] K. Shimamura, S. Uda, T. Yamada, S. Sakaguchi, and T. Fukuda, 'Silicon Single Crystal Fiber Growth by Micro Pulling Down Method', *Japanese Journal of Applied Physics*, vol. 35, no. Part 2, No. 6B, pp. L793–L795, Jun. 1996, doi: 10.1143/JJAP.35.L793.

[45] C. E. Finlayson, A. Amezcua-Correa, P. J. A. Sazio, N. F. Baril, and J. V. Badding, 'Electrical and Raman characterization of silicon and germanium-filled microstructured optical fibers', *Applied Physics Letters*, vol. 90, no. 13, p. 132110, Mar. 2007, doi: 10.1063/1.2713755.

[46] N. Healy, J. R. Sparks, M. N. Petrovich, P. J. A. Sazio, J. V. Badding, and A. C. Peacock, 'Large mode area silicon microstructured fiber with robust dual mode guidance', *Optics Express*, vol. 17, no. 20, p. 18076, Sep. 2009, doi: 10.1364/OE.17.018076.

[47] P. Mehta, N. Healy, N. F. Baril, P. J. A. Sazio, J. V. Badding, and A. C. Peacock, 'Nonlinear transmission properties of hydrogenated amorphous silicon core optical fibers', *Optics Express*, vol. 18, no. 16, p. 16826, Aug. 2010, doi: 10.1364/OE.18.016826.

[48] P. Mehta *et al.*, 'All-optical modulation using two-photon absorption in silicon core optical fibers', *Optics Express*, vol. 19, no. 20, p. 19078, Sep. 2011, doi: 10.1364/OE.19.019078.

[49] B. Scott, 'Fabrication of silicon optical fiber', *Optical Engineering*, vol. 48, no. 10, p. 100501, Oct. 2009, doi: 10.1117/1.3250189.

[50] N. Healy *et al.*, 'Polycrystalline silicon optical fibers with atomically smooth surfaces', *Optics Letters*, vol. 36, no. 13, p. 2480, Jul. 2011, doi: 10.1364/OL.36.002480.

[51] S. Morris *et al.*, 'The influence of core geometry on the crystallography of silicon optical fiber', *Journal of Crystal Growth*, vol. 352, no. 1, pp. 53–58, Aug. 2012, doi: 10.1016/j.jcrysgro.2011.12.009.

[52] S. Morris *et al.*, 'On loss in silicon core optical fibers', *Optical Materials Express*, vol. 2, no. 11, p. 1511, Nov. 2012, doi: 10.1364/OME.2.001511.

[53] T. Minami, S. Maeda, M. Higasa, and K. Kashima, 'In-situ observation of bubble formation at silicon melt–silica glass interface', *Journal of Crystal Growth*, vol. 318, no. 1, pp. 196–199, Mar. 2011, doi: 10.1016/j.jcrysgro.2010.10.075.

[54] E. F. Nordstrand, A. N. Dibbs, A. J. Eraker, and U. J. Gibson, 'Alkaline oxide interface modifiers for silicon fiber production', *Optical Materials Express*, vol. 3, no. 5, p. 651, May 2013, doi: 10.1364/OME.3.000651.

[55] C. Hou *et al.*, 'Crystalline silicon core fibres from aluminium core preforms', *Nature Communications*, vol. 6, no. 1, Dec. 2015, doi: 10.1038/ncomms7248.

[56] N. Healy, J. R. Sparks, P. J. Sazio, J. V. Badding, and A. C. Peacock, 'Tapered silicon optical fibers', *Optics Express*, vol. 18, no. 8, p. 7596, Apr. 2010, doi: 10.1364/OE.18.007596.

[57] D.-J. Won *et al.*, 'All-optical modulation of laser light in amorphous silicon-filled microstructured optical fibers', *Appl. Phys. Lett.*, vol. 91, no. 16, p. 161112, Oct. 2007, doi: 10.1063/1.2790079.

[58] A. Peacock and N. Healy, 'Parabolic pulse generation in tapered silicon fibers', *Optics Letters*, vol. 35, no. 11, p. 1780, Jun. 2010, doi: 10.1364/OL.35.001780.

[59] A. C. Peacock, 'Soliton propagation in tapered silicon core fibers', *Optics Letters*, vol. 35, no. 21, p. 3697, Nov. 2010, doi: 10.1364/OL.35.003697.

[60] A. C. Peacock, 'Mid-IR soliton compression in silicon optical fibers and fiber tapers', *Optics Letters*, vol. 37, no. 5, p. 818, Mar. 2012, doi: 10.1364/OL.37.000818.

[61] S. Zhang *et al.*, 'Temperature characteristics of silicon core optical fiber Fabry–Perot interferometer', *Optics Letters*, vol. 40, no. 7, p. 1362, Apr. 2015, doi: 10.1364/OL.40.001362.

[62] M. Fokine *et al.*, 'Laser structuring, stress modification and Bragg grating inscription in silicon-core glass fibers', *Optical Materials Express*, vol. 7, no. 5, p. 1589, May 2017, doi: 10.1364/OME.7.001589.

[63] F. A. Martinsen, J. Ballato, T. Hawkins, and U. J. Gibson, 'Bulk fabrication and properties of solar grade silicon microwires', *APL Materials*, vol. 2, no. 11, p. 116108, Nov. 2014, doi: 10.1063/1.4902140.

[64] F. A. Martinsen, B. K. Smeltzer, J. Ballato, T. Hawkins, M. Jones, and U. J. Gibson, 'Light trapping in horizontally aligned silicon microwire solar cells', *Optics Express*, vol. 23, no. 24, p. A1463, Nov. 2015, doi: 10.1364/OE.23.0A1463.

[65] N. Healy *et al.*, 'Extreme electronic bandgap modification in laser-crystallized silicon optical fibres', *Nature Materials*, vol. 13, no. 12, pp. 1122–1127, Dec. 2014, doi: 10.1038/nmat4098.

[66] Y. P. Huang and L. A. Wang, 'In-line silicon Schottky photodetectors on silicon cored fibers working in 1550 nm wavelength regimes', *Applied Physics Letters*, vol. 106, no. 19, p. 191106, May 2015, doi: 10.1063/1.4919449.

[67] A. Gumennik *et al.*, 'Silicon-in-silica spheres via axial thermal gradient in-fibre capillary instabilities', *Nature Communications*, vol. 4, no. 1, Dec. 2013, doi: 10.1038/ncomms3216.

[68] J. Bures, *Guided Optics: Optical Fibers and All-fiber Components*. John Wiley & Sons, 2009.

[69] R. Paschotta, 'LP Modes', *RP Photonics Encyclopedia*. https://www.rp-photonics.com/lp_modes.html (accessed Apr. 29, 2019).

[70] G. Agrawal, *Nonlinear Fiber Optics (Fifth Edition)*. Boston: Academic Press, 2013.

[71] K. Han, S. Kim, J. Wirth, M. Teng, Y. Xuan, and B. Niu, 'Strip-slot direct mode coupler', p. 10, 2016.

[72] A. C. Peacock, P. Mehta, P. Horak, and N. Healy, 'Nonlinear pulse dynamics in multimode silicon core optical fibers', *Optics Letters*, vol. 37, no. 16, p. 3351, Aug. 2012, doi: 10.1364/OL.37.003351.

[73] H. H. Li, 'Refractive index of silicon and germanium and its wavelength and temperature derivatives', *Journal of Physical and Chemical Reference Data*, vol. 9, no. 3, pp. 561–658, Jul. 1980, doi: 10.1063/1.555624.

[74] 'Optical Substrates', *Thorlabs.com*, 2019. https://www.thorlabs.com/newgrouppage9.cfm?objectgroup_id=6973&tabname=Silicon (accessed Apr. 24, 2019).

[75] R. Kitamura, L. Pilon, and M. Jonasz, 'Optical constants of silica glass from extreme ultraviolet to far infrared at near room temperature', *Appl. Opt., AO*, vol. 46, no. 33, pp. 8118–8133, Nov. 2007, doi: 10.1364/AO.46.008118.

[76] B. J. Frey, D. B. Leviton, and T. J. Madison, 'Temperature-dependent refractive index of silicon and germanium', in *Optomechanical Technologies for Astronomy*, Jul. 2006, vol. 6273, p. 62732J, doi: 10.1117/12.672850.

[77] D. B. Leviton and B. J. Frey, 'Temperature-dependent absolute refractive index measurements of synthetic fused silica', in *Optomechanical Technologies for Astronomy*, Jul. 2006, vol. 6273, p. 62732K, doi: 10.1117/12.672853.

[78] B. Jalali, V. Raghunathan, D. Dimitropoulos, and Ö. Boyraz, *Raman-Based Silicon Photonics*. 2006.

[79] V. Nathan, S. S. Mitra, and A. H. Guenther, 'Review of multiphoton absorption in crystalline solids', *J. Opt. Soc. Am. B*, vol. 2, no. 2, p. 294, Feb. 1985, doi: 10.1364/JOSAB.2.000294.

[80] T. S. Moss, joint author.) Burrell Geoffrey Joh, and joint author.) Ellis Bria, *Semiconductor opto-electronics*. London : Butterworths, 1973.

[81] L. Yin and G. P. Agrawal, 'Impact of two-photon absorption on self-phase modulation in silicon waveguides', *Opt. Lett., OL*, vol. 32, no. 14, pp. 2031–2033, Jul. 2007, doi: 10.1364/OL.32.002031.

[82] Ö. Boyraz, P. Koonath, V. Raghunathan, and B. Jalali, 'All optical switching and continuum generation in silicon waveguides', *Opt. Express*, vol. 12, no. 17, p. 4094, 2004, doi: 10.1364/OPEX.12.004094.

[83] N. Akhmediev and M. Karlsson, 'Cherenkov radiation emitted by solitons in optical fibers', *Phys. Rev. A*, vol. 51, no. 3, pp. 2602–2607, Mar. 1995, doi: 10.1103/PhysRevA.51.2602.

[84] S. Roy, S. K. Bhadra, and G. P. Agrawal, 'Dispersive waves emitted by solitons perturbed by third-order dispersion inside optical fibers', *Phys. Rev. A*, vol. 79, no. 2, p. 023824, Feb. 2009, doi: 10.1103/PhysRevA.79.023824.

[85] C. J. Liu and E. F. Sieckmann, 'Refractive Index of Calcium Oxide', *Journal of Applied Physics*, vol. 37, no. 6, pp. 2450–2452, May 1966, doi: 10.1063/1.1708835.

[86] G. Brambilla, V. Finazzi, and D. J. Richardson, 'Ultra-low-loss optical fiber nanotapers', *Opt. Express, OE*, vol. 12, no. 10, pp. 2258–2263, May 2004, doi: 10.1364/OPEX.12.002258.

[87] T. E. Dimmick, G. Kakarantzas, T. A. Birks, and P. St. J. Russell, 'Carbon dioxide laser fabrication of fused-fiber couplers and tapers', *Appl. Opt.*, vol. 38, no. 33, p. 6845, Nov. 1999, doi: 10.1364/AO.38.006845.

[88] G. Kakarantzas, T. E. Dimmick, T. A. Birks, R. Le Roux, and P. St. J. Russell, 'Miniature all-fiber devices based on CO_2 laser microstructuring of tapered fibers', *Opt. Lett.*, vol. 26, no. 15, p. 1137, Aug. 2001, doi: 10.1364/OL.26.001137.

[89] G. Brambilla, F. Koizumi, X. Feng, and D. J. Richardson, 'Compound-glass optical nanowires', *Electronics Letters*, vol. 41, no. 7, pp. 400–402, Mar. 2005, doi: 10.1049/el:20058381.

[90] C. Baker and M. Rochette, 'A generalized heat-brush approach for precise control of the waist profile in fiber tapers', *Opt. Mater. Express, OME*, vol. 1, no. 6, pp. 1065–1076, Oct. 2011, doi: 10.1364/OME.1.001065.

[91] J. Dewynne, J. R. Ockendon, and P. Wilmott, 'On a Mathematical Model for Fiber Tapering', *SIAM J. Appl. Math.*, vol. 49, no. 4, pp. 983–990, Aug. 1989, doi: 10.1137/0149059.

[92] R. H. Doremus, 'Viscosity of silica', *Journal of Applied Physics*, vol. 92, no. 12, pp. 7619–7629, Dec. 2002, doi: 10.1063/1.1515132.

[93] J. Zhao and X. Li, 'A Long Wavelength Model for Manufacturing of Continuous Metal Microwires by Thermal Fiber Drawing From a Preform', *J. Micro Nano-Manuf*, vol. 6, no. 1, p. 011003, Dec. 2017, doi: 10.1115/1.4038433.

[94] A. V. Shishkin and A. S. Basin, 'Surface tension of liquid silicon', *Theor Found Chem Eng*, vol. 38, no. 6, pp. 660–668, Nov. 2004, doi: 10.1007/s11236-005-0043-2.

[95] B. M. Epelbaum, K. Shimamura, S. Uda, J. Kon, and T. Fukuda, 'Operating Limits for Stable Growth of Silicon Fibers with Diameter Less Than 150 µm by Modified µ-PD Method', *Crystal Research and Technology*, vol. 31, no. 8, pp. 1077–1084, 1996, doi: 10.1002/crat.2170310817.

[96] R. Hull, *Properties of Crystalline Silicon*. IET, 1999.

[97] E. Ringdalen and M. Tangstad, 'Softening and Melting of SiO2, an Important Parameter for Reactions with Quartz in Si Production', in *Advances in Molten Slags, Fluxes, and Salts:*

Proceedings of the 10th International Conference on Molten Slags, Fluxes and Salts 2016, 2016, pp. 43–51.

[98] Y. Franz, 'Polycrystalline silicon waveguides for integrated photonics', University of Southampton, 2018.

[99] Y. Franz *et al.*, 'Material properties of tapered crystalline silicon core fibers', *Optical Materials Express*, vol. 7, no. 6, p. 2055, Jun. 2017, doi: 10.1364/OME.7.002055.

[100] A. D. Bristow, N. Rotenberg, and H. M. van Driel, 'Two-photon absorption and Kerr coefficients of silicon for 850–2200nm', *Appl. Phys. Lett.*, vol. 90, no. 19, p. 191104, May 2007, doi: 10.1063/1.2737359.

[101] Q. Lin, J. Zhang, G. Piredda, R. W. Boyd, P. M. Fauchet, and G. P. Agrawal, 'Dispersion of silicon nonlinearities in the near infrared region', *Appl. Phys. Lett.*, vol. 91, no. 2, p. 021111, Jul. 2007, doi: 10.1063/1.2750523.

[102] X. Liu *et al.*, 'Self-phase modulation and nonlinear loss in silicon nanophotonic wires near the mid-infrared two-photon absorption edge', *Opt. Express*, vol. 19, no. 8, p. 7778, Apr. 2011, doi: 10.1364/OE.19.007778.

[103] F. Gholami *et al.*, 'Third-order nonlinearity in silicon beyond 2350 nm', *Appl. Phys. Lett.*, vol. 99, no. 8, p. 081102, Aug. 2011, doi: 10.1063/1.3630130.

[104] H. Garcia and R. Kalyanaraman, 'Phonon-assisted two-photon absorption in the presence of a dc-field: the nonlinear Franz–Keldysh effect in indirect gap semiconductors', *J. Phys. B: At. Mol. Opt. Phys.*, vol. 39, no. 12, pp. 2737–2746, Jun. 2006, doi: 10.1088/0953-4075/39/12/009.

[105] H. K. Tsang and Y. Liu, 'Nonlinear optical properties of silicon waveguides', *Semicond. Sci. Technol.*, vol. 23, no. 6, p. 064007, May 2008, doi: 10.1088/0268-1242/23/6/064007.

[106] T. Kato, Y. Suetsugu, M. Takagi, E. Sasaoka, and M. Nishimura, 'Measurement of the nonlinear refractive index in optical fiber by the cross-phase-modulation method with depolarized pump light', *Opt. Lett., OL*, vol. 20, no. 9, pp. 988–990, May 1995, doi: 10.1364/OL.20.000988.

[107] L. Shen *et al.*, 'Nonlinear transmission properties of hydrogenated amorphous silicon core fibers towards the mid-infrared regime', *Opt. Express, OE*, vol. 21, no. 11, pp. 13075–13083, Jun. 2013, doi: 10.1364/OE.21.013075.

[108] S. Pearl, N. Rotenberg, and H. M. van Driel, 'Three photon absorption in silicon for 2300–3300nm', *Applied Physics Letters*, vol. 93, no. 13, p. 131102, Sep. 2008, doi: 10.1063/1.2991446.

[109] C. R. Petersen *et al.*, 'Mid-infrared supercontinuum covering the 1.4–13.3 µm molecular fingerprint region using ultra-high NA chalcogenide step-index fibre', *Nature Photonics*, vol. 8, no. 11, pp. 830–834, Nov. 2014, doi: 10.1038/nphoton.2014.213.

[110] A. M. Heidt *et al.*, 'Mid-infrared ZBLAN fiber supercontinuum source using picosecond diode-pumping at 2 µm', *Opt. Express, OE*, vol. 21, no. 20, pp. 24281–24287, Oct. 2013, doi: 10.1364/OE.21.024281.

[111] P. Domachuk *et al.*, 'Over 4000 nm Bandwidth of Mid-IR Supercontinuum Generation in sub-centimeter Segments of Highly Nonlinear Tellurite PCFs', *Opt. Express, OE*, vol. 16, no. 10, pp. 7161–7168, May 2008, doi: 10.1364/OE.16.007161.

[112] M. Sinobad *et al.*, 'Mid-infrared octave spanning supercontinuum generation to 8.5 µm in silicon-germanium waveguides', *Optica*, vol. 5, no. 4, p. 360, Apr. 2018, doi: 10.1364/OPTICA.5.000360.

[113] N. Nader *et al.*, 'Versatile silicon-waveguide supercontinuum for coherent mid-infrared spectroscopy', *APL Photonics*, vol. 3, no. 3, p. 036102, Mar. 2018, doi: 10.1063/1.5006914.

[114] N. Singh *et al.*, 'Octave-spanning coherent supercontinuum generation in silicon on insulator from 1.06 µm to beyond 2.4 µm', *Light: Science & Applications*, vol. 7, no. 1, p. 17131, Jan. 2018, doi: 10.1038/lsa.2017.131.

[115] M. A. Ettabib *et al.*, 'Broadband telecom to mid-infrared supercontinuum generation in a dispersion-engineered silicon germanium waveguide', *Opt. Lett., OL*, vol. 40, no. 17, pp. 4118–4121, Sep. 2015, doi: 10.1364/OL.40.004118.

[116] B. Kuyken *et al.*, 'An octave-spanning mid-infrared frequency comb generated in a silicon nanophotonic wire waveguide', *Nature Communications*, vol. 6, p. 6310, Feb. 2015, doi: 10.1038/ncomms7310.

[117] H. Bach and N. Neuroth, Eds., *The Properties of Optical Glass*. Berlin Heidelberg: Springer-Verlag, 1998.

[118] M. A. Khashan and A. Y. Nassif, 'Dispersion of the optical constants of quartz and polymethyl methacrylate glasses in a wide spectral range: 0.2–3 µm', *Optics Communications*, vol. 188, no. 1, pp. 129–139, Feb. 2001, doi: 10.1016/S0030-4018(00)01152-4.

[119] H. Hu, X. Zhang, W. Li, and N. K. Dutta, 'Simulation of octave spanning mid-infrared supercontinuum generation in dispersion-varying planar waveguides', *Applied Optics*, vol. 54, no. 11, p. 3448, Apr. 2015, doi: 10.1364/AO.54.003448.

[120] C. Ciret and S.-P. Gorza, 'Generation of ultra-broadband coherent supercontinua in tapered and dispersion-managed silicon nanophotonic waveguides', *Journal of the Optical Society of America B*, vol. 34, no. 6, p. 1156, Jun. 2017, doi: 10.1364/JOSAB.34.001156.

[121] J. Degallaix *et al.*, 'Bulk optical absorption of high resistivity silicon at 1550 nm', *Opt. Lett., OL*, vol. 38, no. 12, pp. 2047–2049, Jun. 2013, doi: 10.1364/OL.38.002047.

[122] T. Wang *et al.*, 'Multi-photon absorption and third-order nonlinearity in silicon at mid-infrared wavelengths', *Optics Express*, vol. 21, no. 26, p. 32192, Dec. 2013, doi: 10.1364/OE.21.032192.

[123] J. M. Dudley and S. Coen, 'Coherence properties of supercontinuum spectra generated in photonic crystal and tapered optical fibers', *Optics Letters*, vol. 27, no. 13, p. 1180, Jul. 2002, doi: 10.1364/OL.27.001180.

[124] J. M. Dudley and S. Coen, 'Numerical simulations and coherence properties of supercontinuum generation in photonic crystal and tapered optical fibers', *IEEE Journal of Selected Topics in Quantum Electronics*, vol. 8, no. 3, pp. 651–659, May 2002, doi: 10.1109/JSTQE.2002.1016369.

[125] S. Antipov, D. D. Hudson, A. Fuerbach, and S. D. Jackson, 'High-power mid-infrared femtosecond fiber laser in the water vapor transmission window', *Optica, OPTICA*, vol. 3, no. 12, pp. 1373–1376, Dec. 2016, doi: 10.1364/OPTICA.3.001373.

[126] R. Paschotta, 'Noise of mode-locked lasers (Part I): numerical model', *Appl Phys B*, vol. 79, no. 2, pp. 153–162, Jul. 2004, doi: 10.1007/s00340-004-1547-x.

[127] T. A. Birks and Y. W. Li, 'The shape of fiber tapers', *Journal of Lightwave Technology*, vol. 10, no. 4, pp. 432–438, Apr. 1992, doi: 10.1109/50.134196.